Effects of Deglaciation on Glaciovolcanism on Mars

Exploring the origin of tuyas in the Martian South Polar Region

Joana Lisa Wiese

Delft University of Technology

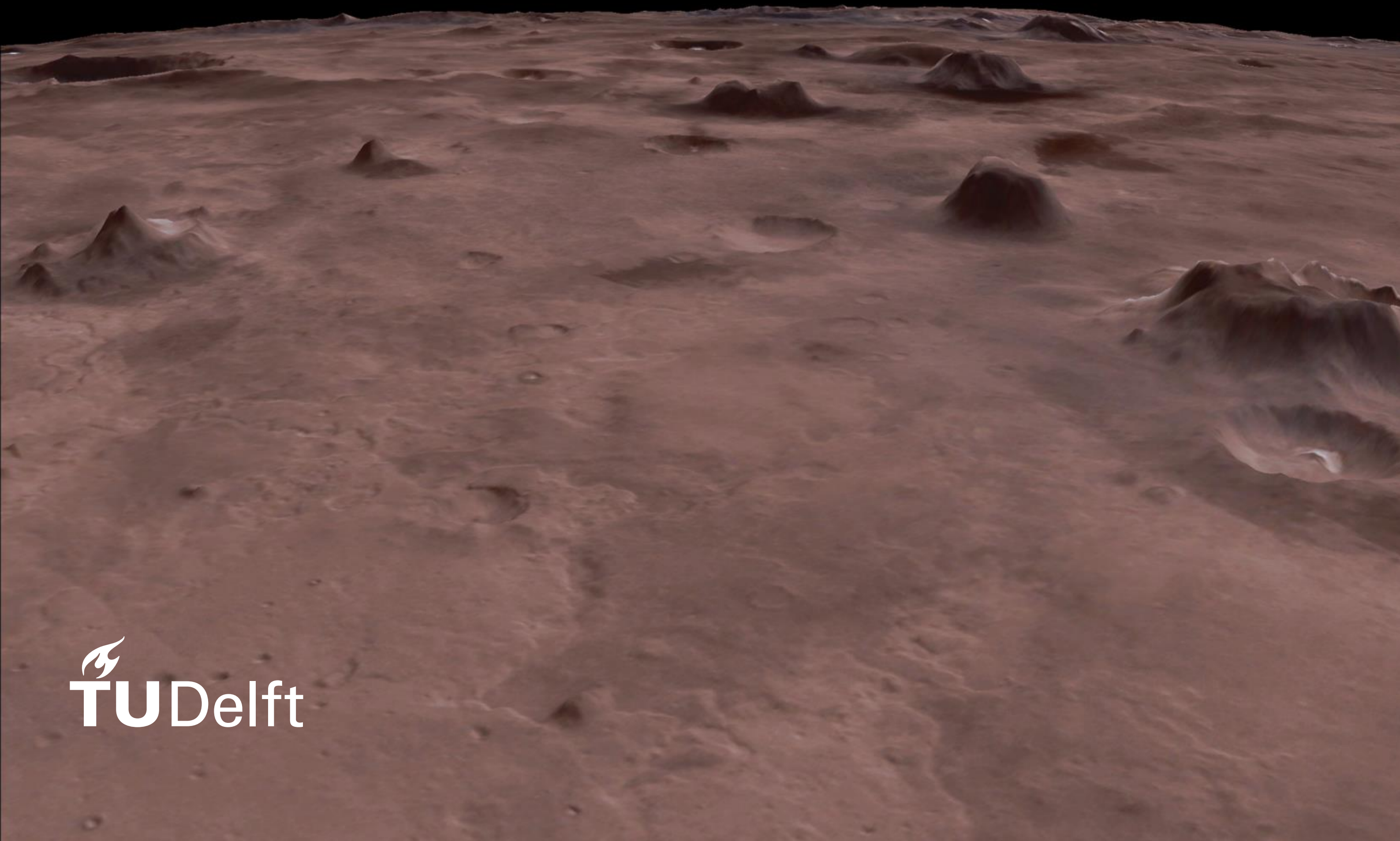

Effects of Deglaciation on Glaciovolcanism on Mars

Exploring the origin of tuyas in the Martian South Polar Region

by

Joana Lisa Wiese

To obtain the degree of Master of Science
at the Delft University of Technology,
to be defended publicly on November 22, 2021.

Student number:	4342364	
Project duration:	February 2, 2021 – November 22, 2021	
Thesis committee:	Dr. S.J. de Vet,	TU Delft AE, supervisor
	Dr. ir. W. van der Wal,	TU Delft AE, supervisor
	Dr. S.M. Cazaux,	TU Delft AE & chair
	Dr. S.L.M. Lhermitte,	TU Delft CEG, external

Cover image shows view of Sisyphi Montes on Mars. Credits of global colourized mosaic:
USGS Astrogeology Science Center, NASA, JPL, Esri

Preface

This document is the Master of Science thesis ”Effects of deglaciation on Glaciovolcanism on Mars - Exploring the origin of tuyas in the Martian South Polar Region”. This thesis concludes my studies at the faculty of Aerospace Engineering at Delft University of Technology where I followed the master in Space Exploration.

I started my project with the second wave of the CoVid-19 crisis and even though working from home was the new norm, I had not expected to write my Master thesis in my student room. Nevertheless, thanks to the support from my supervisors, friends and family I was able to finish this project successfully and I have learned a great deal on the way.

First of all, I would like to thank Dr. Wouter van der Wal and Dr. Sebastiaan de Vet for their endless patience, flexibility and support throughout the process. Thank you for being critical and taking the time to discuss ideas with me. I very much enjoyed working together.

Secondly, I thank Dr. Dan McKenzie and Dr. Peter Schmidt for answering my questions on the processes in Iceland and their interest in my research. I would also like to show my appreciation to Jesse and Weilun for taking the time to discuss my results and sharing ideas. It has always been a pleasure to hear your perspectives.

Furthermore, a big thanks to Dr. S, Cazaux and Dr. S. Lhermitte for being part of the thesis committee and evaluating my work.

I also thank the people from my Master support group: Daniel, Wouter, Lina, Bushra, José and Pieter. Thank you for sharing your own struggles and listening to mine. I would not have made it without you guys. My family has been very supportive, as well and I’d like to thank my parents and siblings for being there for me.

Last, but not least, I would like to express my gratitude to Jasper for his endless support and patience during the entire time. You always put a smile on my face.

Joana Lisa Wiese
Delft, November 8, 2021

Executive Summary

In the South Polar Region on Mars a number of glaciovolcanic edifices, similar to terrestrial tuyas have been found (Ghatan and Head, 2002). On Earth, tuyas can be used to derive palaeo ice sheet parameters such as thickness (Smellie and Edwards, 2016). Research on Earth suggests that the deglaciation of ice sheets can cause an increase in volcanic activity as a result of enhanced mantle melting (Jull and McKenzie (1996); Schmidt et al. (2013)). Since remnants of glaciovolcanic activity are present on Mars, this study aims to find support for the following research hypothesis: *The unloading of the Martian mantle, due to melting of a former ice sheet, has contributed to forming tuyas, glaciovolcanic edifices, in the South Polar Region on Mars.* This research can advance our knowledge on geophysical processes on Mars. Furthermore, results from this study can be compared to findings on Earth and further conclusions can be drawn from similarities and differences.

In this study the relation between tuya height and palaeo ice sheet thickness is applied on Mars and the first ever regional reconstruction of a palaeo ice sheet thickness in the South Polar Region on Mars has been done. A circular, perfectly plastic ice sheet is with an optimum ice divide height of 1754 m and a radius of 600 km is found.

Based on evolution of obliquity, three different deglaciation periods are applied in the modelling: 1 kyr, 30 kyr and 60 kyr. The shortest deglaciation is comparable to the ice melt in Iceland during the last glacial maximum.

To analyse the decompression rates ($\frac{dP}{dt}$) in the mantle, Mars is modelled in Abaqus as an incompressible, elastic lithosphere overlaying an incompressible Maxwell viscoelastic mantle (Simulia Abaqus, 2014a). The reconstructed ice sheet is used as surface pressure load and decays linearly over time.

In general $\frac{dP}{dt}$ decrease with depth and time, which is in good agreement with findings in Iceland (Jull and McKenzie (1996); Pagli and Sigmundsson (2008)). In addition, sensitivity to lithosphere thickness is found, with a decrease in $\frac{dP}{dt}$ for a thicker lithosphere.

In the model with a thin lithosphere of 35 km for a deglaciation period of 1 kyr a decompression rate of 1450 Pa/yr is found at a depth of 500 km. This is equal to the maximum decompression rate under Vatnajökull right below the lithosphere. Decompression rates can cause a drop in solidus temperature that when shifted equal to or below the mantle temperature results in melt. An initial melt depth of 490 km was estimated by Ding et al. (2020). These findings support the possibility for a decrease in solidus at 500 km to initiate melt due to unloading of the surface. However, increase in volcanism is highly dependent on the magma ascent velocity. For tuyas to form, volcanism must take place while the ice sheet is still present. Assuming an ascent velocity of 1000 m/yr, generated melt at a depth of 500 km would reach the surface within 500 yr. This is sufficient for volcanism to take place within a deglaciation of 1 kyr. In addition, propagation of dykes in the lithosphere could accelerate magma ascent. This is likely to take place based on estimated driving pressures.

As conclusion, for a warm, wet Martian climate, and conditions mentioned above, mantle unloading due to ice melt could have contributed to the formation of tuyas in the South Polar Region. This study proposes that the deglaciation of Vatnajökull today and its effect on mantle melting is a good analogue study for geophysical processes related to deglaciation on past Mars, provided that climate and surface conditions were similar to Iceland today.

Contents

List of Figures

List of Tables

Nomenclature

Acronyms

CTX	Context Camera
DAF	Dorsa Argentea Formation
ECEF	Earth Centered Earth Fixed
ESRI	Environmental Systems Research Institute
GIA	Glacial Isostatic Adjustment
Gyr	Billion years
HiRISE	High Resolution Imaging Science Experiment
FEM	Finite Element Method
kyr	Thousand years
MAE	Mean Absolute Error
MOC	Mars Orbiter Camera
MOLA	Mars Orbiter Laser Altimeter
MEGDR	Mission Experiment Gridded Data Records
MRO	Mars Reconnaissance Orbiter
Myr	Million years
PZ	Passage Zone

List of Symbols

$\epsilon_{\hat{m}}$	[deg]	Obliquity
ρ	[kg/m^3]	Density
σ	[Pa]	Normal stress component
τ	[Pa]	Shear stress component
$\vec{\tau}$	[Pa]	Stress tensor
$\vec{t}$	[Pa]	Stress tensor after transformation
ν	[-]	Poisson's ratio
E	[Pa]	Young's modulus
G	[m^3/kg s^2]	Universal gravitational constant
H$_0$	[m]	Ice height at ice divide
L	[m]	Length
M	[kg]	Mass
P	[Pa]	Pressure
R	[m]	Radius
S	[Pa]	Shear modulus
T	[K]	Temperature
T$_{pot}$	[°C]	Mantle potential temperature
W	[m]	Width
g	[m/s^2]	Gravitational acceleration
h$_m$	[m]	Ice elevation at specific mountain
n	[-]	Number of mountains
p	[Pa]	Pressure after stress transformation
t	[yr]	Time
u$_z$	[m]	Vertical component of displacement
z$_m$	[m]	Passage zone elevation at specific mountain

1

Introduction

When glaciation and volcanism coincide a process termed glaciovolcanism can take place. By definition: *Glaciovolcanism refers to all types of volcano interaction with ice in all its forms (including snow and firn) and, by implication, any meltwater derived from that ice by volcanic heating* (Smellie, 2006). During glaciovolcanic processes very distinct edifices are formed which have helped to understand Earth's palaeoclimate and the processes involved when ice and lava interact (Licciardi et al. (2007); Smellie and Edwards (2016); Tuffen et al. (2010); Walker (1965); Wilson et al. (2019)). The most prominent edifices are tuyas: circular or sub-rectangular, flat-topped mountains with steep sides (Mathews, 1947). Tuyas are form by volcanic eruption under thick ice and have very distinct geomorphological features that can be used to identify ice sheet parameters, such as thickness and extent. One of these features are horizontal passage zones (PZ), which mark the transition from subaqueous to subaerial volcanism in the formation process. A table of terminology used in the research is provided in Section 1.1.

The formation of tuyas can be described in four general stages by Jones' classical tuya model (Jones, 1968) (Figure 1.1). The model assumes a basaltic subglacial eruption.

In the first stage (Figure 1.1 (a)) magma rises to the bedrock-ice interface and causes an initial effusive eruption. Due to the high confining pressure from the overlaying ice sheet and generated meltwater, magma fragmentation and volatile release is suppressed. The main effusive product is pillow lava (small grey pebbles in Figure 1.1) with possibly small volumes of hyaloclastites (volcanic glass) (Edwards et al., 2015). During the building of pillow lava and increase in edifice height, melting and sagging of the ice above creates a cauldron on the surface (circular lines on ice surface right above the pillow lava mound in Figure 1.1 (a)).

Thinner ice and the increased height of the edifices result in less pressure which in turn supports volatile release and magma fragmentation. In this stage the eruption becomes explosive (phreatomagmatic) and a subaqueous tuff cone is formed including hyaloclastite (brown cone-shaped layer in Figure 1.1 (b)). Eventually, the ice collapses or is melted through and an englacial lake surrounds the volcanic edifices (Figure 1.1 (b)).

Stage three (Figure 1.1 (c)) starts once the top of the growing edifice breaches the surface of the lake or the ice sheet, resulting in a transition to subaerial eruption. Since the vent dries out, the eruption becomes effusive again and is fully magmatic at this point in time. From this, a pyroclastic cone may form made of palagonite and accumulation of abundant scoria (ejected vesicular volcanic rock) (yellow cone on top of the brown tuff-cone in Figure 1.1 (c)). Lava can also flow away from the vent laterally and into the surrounding lake where it forms lava-fed deltas that prograde into the water (yellow-brown layers on left and right side with lava feeds marked in grey in Figure 1.1 (c)). With the progradation of the delta, lava flows resurface at the top of the edifice (black-brown block-like layer on top of the yellow cone in Figure 1.1 (c)). The boundary between the products from subaqueous and subaerial eruptions is called the passage zone (Edwards et al. (2015); Russell et al. (2014); Smellie and Edwards (2016); Smellie (2018)). As mentioned earlier, this feature is one of the critical palaeoclimate proxies and provides information on the height of the englacial lake or minimum ice sheet thickness where the edifice emerged. Different types of passage zones exist, most examples published so far include the horizontal passage zone (Smellie, 2006). Such a passage zone is generally identifiable as a horizontal line in the edifice structure, clearly separating different lithofacies. Variations in passage zone elevation give an idea about changes in the lake level and/or ice thickness controlled by drainage or the glacial hydrology (Edwards et al., 2015). For more details on passage zones the reader is referred to the resources by Smellie (2006) and Smellie and Edwards (2016).

The last and final stage of the tuya formation (Figure 1.1 (d)) gives the tuya its characteristic flat top. With the deltas prograding into the lake water, subaerial lava flows distribute laterally until they reach the ice margin (black layer on top of edifice in Figure 1.1 (d)). This forms a protective lava cap on top of the edifice that also helps to preserve the tuya from being removed by future glaciations (Smellie, 2018). Depending on the frequency of eruption and amount of magma that reaches the top, the lava caps of tuyas can become quite thick. Observations in Iceland revealed lava caps up to 350 m thick (Jakobsson and Johnson, 2012).

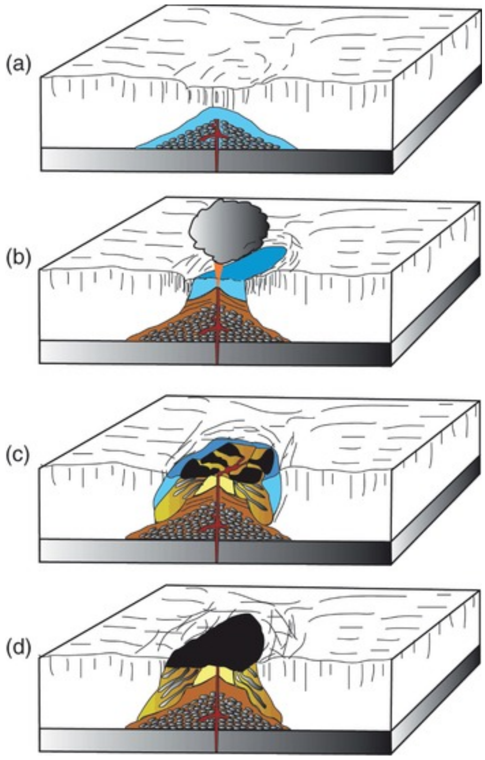

Figure 1.1: 'Classic' tuya model by Jones (1968), showing four stages of tuya formation obtained from Smellie and Edwards (2016). Explanation of colours in subfigures: (a) red vertical lines: rising magma; grey pebbles: pillow lava. (b) brown cone-shaped layer: tephra mound / tuff cone and hyaloclastite. (c) yellow cone: pyroclasitc cone, dried vent; yellow-brown layer on left and right side: lava-fed tuff-breccia deltas with lava flows as grey lines inside; black-brown blocky layer on top: subaerial lava flow. (d) black surface layer: lava cap.

The cap rock is not always entirely smooth and flat, but often contains a small cone shaped that formed during the subaerial eruption. The cone indicates the location of the volcano vent where lava flows out and pyroclastic material erupts. An example of a tuya with a summit cone is the Herðubreið tuya in Iceland (Figure 1.2). One can clearly see the vent location as summit cone. The thick lava cap rock can be identified and is labelled in Figure 1.2. In addition, the bird's foot shaped lava-fed deltas are visible and pillow lavas are marked that were created during the four-stage formation at the tuya flanks.

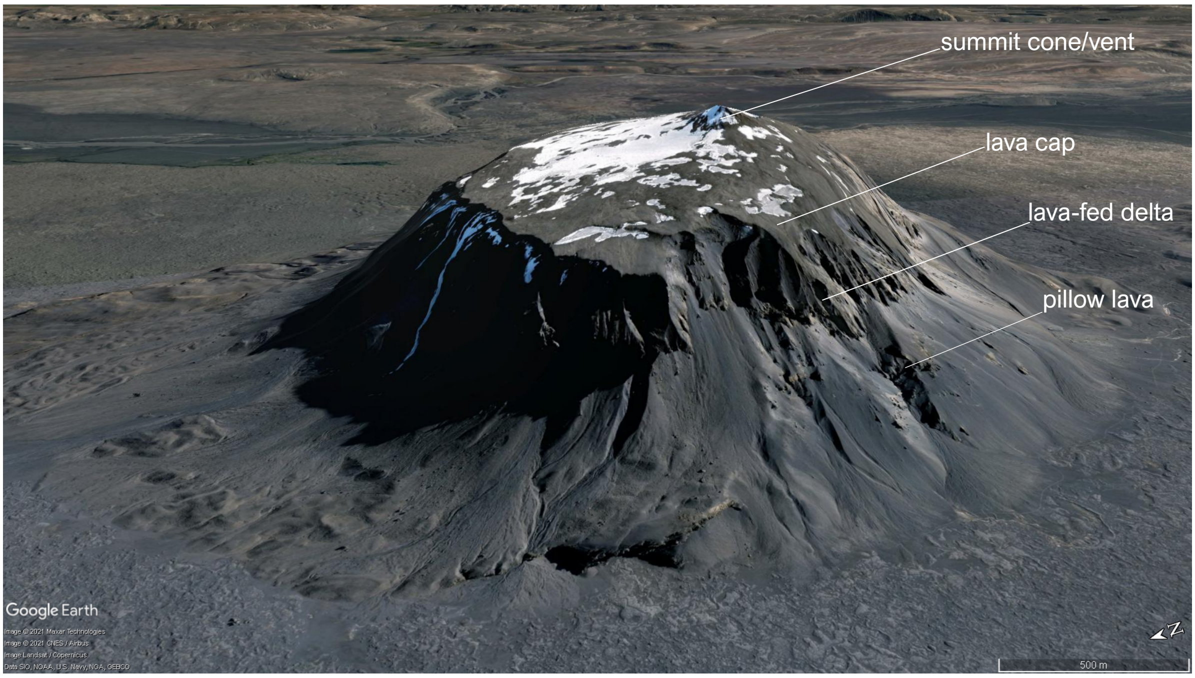

Figure 1.2: Google Earth Landsat/Copernicus image of the western face of the Herðubreið tuya in Iceland. Clear lava cap rock identifiable as the top most layer with a small summit cone where the vent used to be. Image credits: Maxar Technologies and CNES/Airbus, 2021

By studying and understanding this natural process on Earth we are able to investigate the shaping of the landscape and recover palaeoenvironmental information (Russell et al. (2014); Smellie and Edwards (2016)). In addition, we can monitor and possibly mitigate volcanic hazards (massive flooding by melt-water and tephra production) (Barr et al. (2018); Gudmundsson et al. (2008); Huggel et al. (2007); Kelman et al. (2002)) and gain knowledge on the biological evolution of our planet (Ackiss et al. (2018); Fraser et al. (2014)). Besides this, we can better understand the impact of volcanism on the stability of our present day ice sheets (De Vries et al. (2018); Iverson et al. (2017); Seroussi et al. (2017)) and analyse how ice growth and retreat may influence volcanism in turn (Edwards et al. (2020); Jull and McKenzie (1996); Sigmundsson et al. (2010)). The effect of ice retreat on volcanic activity on Earth involves the process of glacial isostatic adjustment (GIA). The response of the solid Earth to the melting of the ice triggers processes in the mantle and crust that can regionally affect the generation and supply of magma, leading to and increased volcanic activity.

The terminology used in this research is listed in Section 1.1. After this, a detailed overview of Glacial Isostatic Adjustment (GIA) and its effect on volcanism on Earth is provided in Section 1.2. Section 1.3 describes the process of glaciovolcanism on Mars, including the description of a set of glaciovolcanic edifices in the South Polar Region. Furthermore, Martian obliquity cycles and the effect on ice deposition are described in Section 1.3.1, followed by introduction to the Martian interior structure in Section 1.4. Using the knowledge obtained from research on Earth and the understanding of volcanic and glacial processes on Mars, the research objective and questions for this study are presented in Section 1.5.

1.1. Terminology

During this research, we found variations in terminology within the research field. To ensure consistent use of words within this work, we present a list of definitions in Table 1.1 with references.

Table 1.1: Terminology in the research at hand.

Term	**Definition**	**Reference**
cold-based ice	frozen-bed ice, ice that is frozen to its bed and protects bedrock surfaces	(Smellie and Edwards, 2016)
dyke	tabular or sheet-like magma bodies that cut through the layering of adjacent rocks formed by magma rising into fractures or creating cracks	U.S. Geological Survey[1]
edifices	the main portion of a volcano built by eruption of lava, tephra, pyroclastic flows, lahars, and related volcanic deposits	U.S. Geological Survey[2]
glaciovolcanism	the interaction of magma and ice in all forms (ice, snow, firn, any melt-water)	(Smellie, 2006)
hyaloclastite	volcanic glass fragments formed by quench fragmentation of magma	(Edwards et al., 2015)
knick point	An abrupt change of gradient in the mountain profile reflecting different conditions and processes	-
lava-fed deltas	distinctive nearly flat-topped steep-sided volcanic landform sourced in a subaerial volcano that is formed principally by mafic lava where it enters standing water. They have digitate (bird's foot) or lobate (cat's paw) terminations.	Smellie (2014)
lithofacies	deposits with a combination of distinct characteristics that help to understand the depositional environment and processes that produce them	Smellie and Edwards (2016)
lithosphere	the fully elastic layer of the planet's internal structure	-
palagonite	altered product resulting from the interaction of water and volcanic glass, generally yellow-orange in colour	(Stroncik and Schmincke, 2002)
passage zone	the boundary that marks the transition between subaerial conditions and subaqueous	(Jones, 1968)
pillow lava	elongated lava pillow mounds that formed by repeated quenching of hot basalt	U.S. Geological Survey[3]
subglacial	processes under the ice cover without direct exposure to atmosphere	(Jakobsson and Gudmundsson, 2008)
tuff	general term for all hardened rock that originated from an explosive volcanic eruption	U.S. Geological Survey[4]
tuya	a circular or subrectangular, flat-topped volcanic edifices with steep sides, made up of hyaloclastites and/or pillow lavas and contain cap lava	(Mathews, 1947)

---

[1] U.S. Geological Survey (2013). Dike. In USGS Volcanic Hazards Program Glossary. Retrieved October 25, 2021 from https://volcanoes.usgs.gov/vsc/glossary/dike.html

[2] U.S. Geological Survey (2013). Edifice. In USGS Volcanic Hazards Program Glossary. Retrieved October 20, 2021 from https://volcanoes.usgs.gov/vsc/glossary/edifice.html

[3] U.S. Geological Survey (2013). Pillow lava. In USGS Volcanic Hazards Program Glossary. Retrieved October 25, 2021 from https://volcanoes.usgs.gov/vsc/glossary/pillow_lava.html

[4] U.S. Geological Survey (2013). Tuff. In USGS Volcanic Hazards Program Glossary. Retrieved October 25, 2021 from https://volcanoes.usgs.gov/vsc/glossary/tuff.html

1.2. GIA as a Trigger for Volcanism

Earth has undergone multiple glacial cycles (Earle, 2015) and the Last Glacial Maximum occurred about 21 kyr ago. After this period of cold climate, the Northern Hemisphere ice sheets collapsed (Whitehouse, 2018) and the variations between cold and warm climate still affect the planet, causing geophysical processes such as Glacial Isostatic Adjustment (GIA). GIA is the response of the solid Earth, the gravitational field and the oceans to the melting or growing of an ice sheet (Whitehouse, 2018). In this process, isostatic assumes that the system is growing towards a state of equilibrium (isostasy) (Whitehouse et al., 2021). In the study at hand we define the lithosphere as follows: the fully elastic layer of the planet's internal structure. We denote the lithosphere thickness as T_e.

During ice growth the underlying lithosphere subsides, leading to compression in the upper lithosphere layer and tension in the lower lithosphere (right below the ice sheet). Due to the loading, the viscous mantle material underneath flows away from the location, redistributing mass over the planet. During ice decay the rebound period can begin, in which the surface rises and reverses the tensional and compressional states in the lithosphere. Mantle material can flow back to the region where ice used to be, redistributing mass yet again. A visualisation of this process is provided in Figure 1.3.

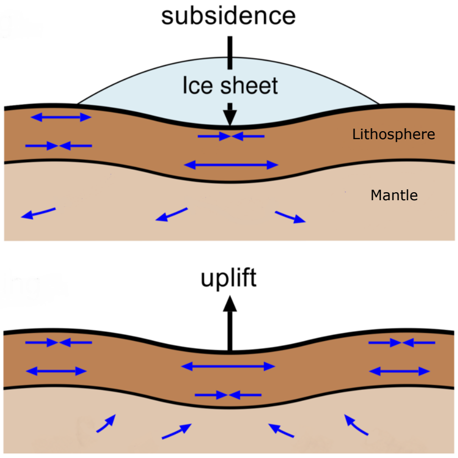

Figure 1.3: The process of GIA on Earth. Dark brown region denotes the lithosphere, light brown region is the Earth's viscous mantle. Blue arrows show the tensional or compressional states inside the lithosphere and the flow of the mantle underneath. Figure modified from Helmholtz Centre Potsdam[5].

When investigating deformations and processes in the mantle the thickness of the lithosphere and the size of the surface load are essential. Their ratio determines the state of isostasy. Figure 1.4 below shows the different states of isostasy. Thick lithospheres, much greater than the load, result in no isostasy. This means that the lithosphere does not bend entirely under the presented load, but only deforms slightly at the top. With decreasing thickness of T_e for the same load size, isostasy increases. This leads to more flexure of the elastic layer up until local isostasy is reached. For this research the case of regional isostasy takes place, as the elastic thickness is much smaller than, or approximately equal to the size of the above ice load.

---

[5] Helmholtz Centre Potsdam. *Glacial isostatic adjustment (GIA)*. GFZ German Research Centre for Geosciences. Retrieved on October 26, 2021 from `https://www.gfz-potsdam.de/en/section/earth-system-modelling/topics/solid-earth-dynamics/glazial-isostatic-adjustment-gia/`

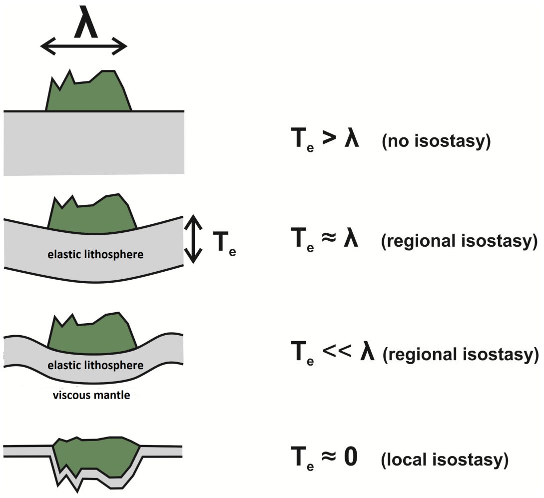

Figure 1.4: States of isostasy with λ being the wavelength size of the surface load and T_e the effective elastic thickness of the lithosphere. Modified graphic from [6].

On Earth, for loads applied over a time scale of hundreds to thousands of years, the total deformation of the material contains an elastic and a viscous component. For such cases the rheology is often modelled with a linear Maxwell model which is the simplest model that can describe short term elastic and long term viscoelastic behaviour (Maxwell, 1867). Maxwell rheology is represented by a spring-damper system, where the spring models the elastic behaviour of the lithosphere and the damper the viscous fluid of the mantle. For mantle viscosities of 10^{21} Pa · s and a Shear modulus of 10^{11} Pa, the Maxwell time is in the order of 1 kyr (Whitehouse et al., 2021). This approximation has been found applicable for other planets, in particular for Mars (Broquet et al. (2020); Johnson et al. (2000)) as used in this study.

However, GIA not only results in surface deformations, but also in decompression of the upper mantle. This change in decompression in the Earth's mantle can lead to an increase in magma generation (Jull and McKenzie (1996); Pagli and Sigmundsson (2008); Schmidt et al. (2013); Sigmundsson et al. (2010)). In addition, magma chambers in the crust may be affected by the changing stress states in the lithosphere. It has been shown that glacial loading causes magma trapping due to compressive stresses in the crust, whereas unloading of the surface results in stress relaxation and the release of accumulated magma (Wilson and Russell, 2020). In addition, these stress changes can lead to fracture and eventual failure of magma chambers (Sigmundsson et al. (2010)). Furthermore, induced horizontal stresses during unloading may alter the storage conditions and dyke dynamics inside the crust (Jellinek et al. (2004); Mora and Tassara (2019)). Dykes form when magma rises into an existing fracture or forces its way through rock and then solidifies. They are sheet-like or tabular magma bodies that cut through or across older rocks and are generally directed vertically. Wilson and Russell (2020) indicated that it might be possible that both, increased mantle melting rate and modulation of magma transport by dyke propagation are a response to glacial loading and unloading in Iceland. The formation of dykes is more favourable at a spreading ridge, such as in Iceland. However, heavily cratered surfaces might also be favourable for dyke propagation in the crust. Such surfaces can be found in the southern highlands on Mars, but it is still to be proven whether they benefit dyke formation.

---

[6] Wikipedia (2015). *Isostasy*. Accessed on October 26, 2021 at `https://en.wikipedia.org/wiki/Isostasy`. Graphic licensed under Creative Commons Attribution-share Alike 4.0 International.

The focus of this study is the effect of deglaciation on mantle melting on Mars, where the detailed research done in Iceland serves to draw comparative conclusions. For understanding the influence of deglaciation on mantle melting, Iceland is a favourable study area, as it lies above a spreading ridge. It is important to note that for mantle melting to take place the in situ pressure needs to decrease. This pressure decrease can cause a drop in the melting temperature of the mantle material. However, if and only if the melting temperature drops below the actual mantle temperature does the material start to melt (P. Schmidt, personal communication, October 5, 2021).

Modelling of the glacially induces pressure changes in the Icelandic mantle by Jull and McKenzie (1996) has shown that a 2 km thick ice sheet that decayed over 1 kyr can lead to an increase in magma generation of up to 3.4 km^3/yr. This is about 30 times higher than during glacial periods. The associated maximum pressure change was 19 kPa/yr.

Further studies found that recent deglaciation (120 yr) of Vatnajökull, the largest ice sheet in Iceland, could cause an increase in melt production of 0.21-0.23 km^3/yr. Pressure changes associated with this melt generation had a maximum of 1450 Pa/yr right below the lithosphere (Schmidt et al., 2013). In conclusion, these two studies show that magma generation is related to pressure changes in the mantle, which is affected by the ice sheet thickness and extent, as well as the deglaciation period.

1.3. Glaciovolcanism on Mars

Besides Earth, also Mars has potential for hosting glaciovolcanic processes in the past and maybe even in the present. In the following section an overview of glaciovolcanic edifices in the Southern Polar Region on Mars is provided with an explanation on how to identify such landforms. Section 2.2.2 elaborates on Martian obliquity cycles and its influence on ice covers on the red planet.

For glaciovolcanism to take place, periods of glaciation and volcanism need to coincide. Same as on Earth also Mars experiences variations in climate and it has been shown that periods of glaciation and volcanism have occurred simultaneously (Cousins and Crawford (2011); de Vet (2013); Neukum et al. (2010)), which makes glaciovolcanic eruptions a likely process on the red planet. A timeline overview of such periods is provided in Figure 1.5.

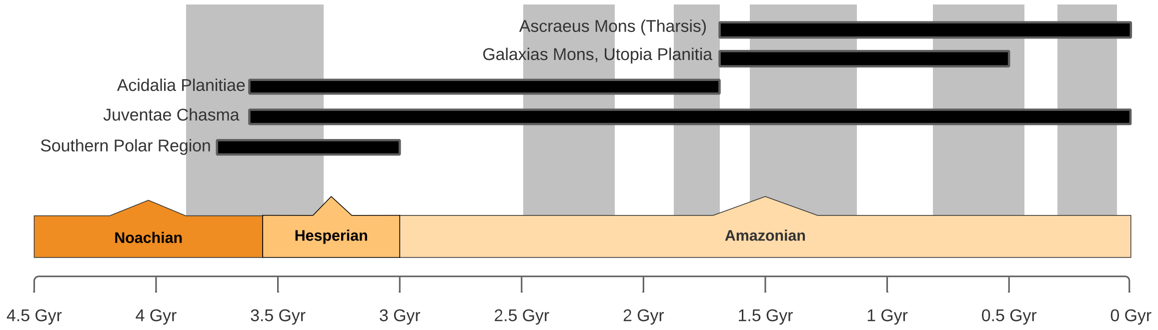

Figure 1.5: Periods of glaciovolcanism on Mars over time, showing the Martian epochs and timeline in Gyr ago. Gray vertical bars represent peak periods of simultaneous volcanism and glaciation (3.8-3.3 Gyr, 2.5-2.2 Gyr, 2.0-1.8 Gyr, 1.6-1.2 Gyr, 800-300 Myr and 200-100 Myr ago). Black horizontal bars indicate estimated formation periods of glaciovolcanic features at specific eruption locations (Cousins and Crawford, 2011).

In multiple regions on Mars remnants similar to terrestrial glaciovolcanic edifices have been identified using spacecraft images (Allen (1979); Fagan et al. (2010); Ghatan and Head (2002)). Comparative studies to Icelandic glaciovolcanoes shed light on a number of differences between the features on Earth and Mars (Fagan et al., 2010). Most evident is the difference in size, with Martian features being larger and more massive than terrestrial ones. A possible explanation for the larger Martian remnants is their formation in cold-based ice which does not restrict the tuya height, as meltwater can only escape by overflow (Smellie, 2013).

In the South Polar Region, specifically in the Dorsa Argentea Formation (DAF), a group of mountains has been identified by Ghatan and Head (2002) to be of glaciovolcanic origin. In this region glaciation and volcanism is thought to have taken place during the late Noachian to late Hesperian period, about 3.8 to 3.2 billion years ago (Cousins and Crawford (2011); de Vet (2013); Neukum et al. (2010)). Evidence for volcanism has been found by geological mapping the surface of the mountainous area by Tanaka and Scott (1987) and Ackiss et al. (2018), who found that most surface materials are gypsum, smectite-zeolite-iron-oxide which could be palagonite and polyhydrated sulfate, associated with volcanic activity (Ackiss et al., 2018). Palagonite is a product of volcanic glass alteration that forms during interaction with water. It has a similar chemical composition to basalt and is generally yellow-orange to yellow-brown in colour (Stroncik and Schmincke, 2002). This specific type of material provides further evidence that the mountains are of subglacial origin due to its interaction with water during formation.

The location of the region on Mars is marked on the map in Figure 1.6, made with a Natural Earth projection. A detailed view, where fourteen of the identified edifices are labelled, can be found in Figure 1.7. Both maps were made in ArcGIS Pro using the Mars2000 geographic coordinate system. An Albers Equal Area projection is best suited for regions in the mid-latitudes and uses two standard parallels to reduce distortions in shape, distant and angle. As the name already indicates, this map projection preserves areas. A Natural Earth projection is used for world maps and was specifically designed to display physical data[7]. More details on using ArcGIS Pro on Mars can be found in Appendix A. The mountains are hereafter referred to as the Sisyphi Montes (Ackiss et al., 2018).

---

[7] Šavrič, B. & Kennedy, M. (2020). *Map Projections in ArcGIS*. Retrieved on October 26, 2021 from `https://storymaps.arcgis.com/stories/ea0519db9c184d7e84387924c84b703f`

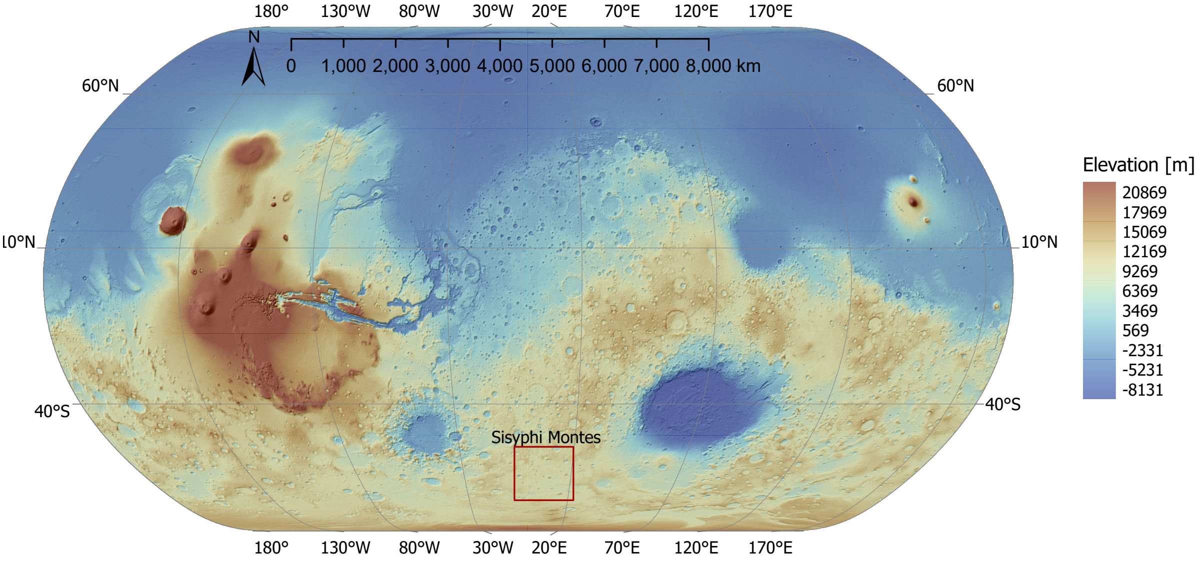

Figure 1.6: Global Mars Orbiter Laser Altimeter (MOLA) topography map over hillshade in a Natural Earth projection. High elevations in red and low elevations in blue colour. The Sisyphi Montes region is marked with the red rectangle.

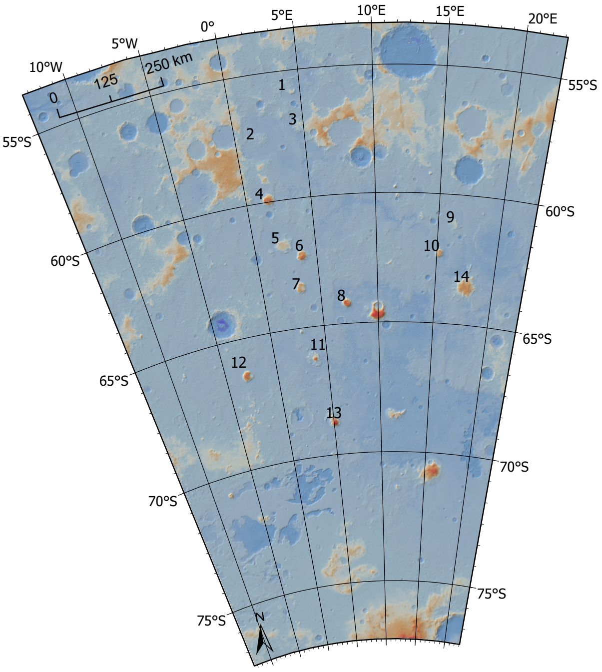

Figure 1.7: MOLA Shaded Relief of Sisyphi Montes in Albers Equal Area map projection. Fourteen edifices labelled, previously identified as of glaciovolcanic origin by Ghatan and Head (2002).

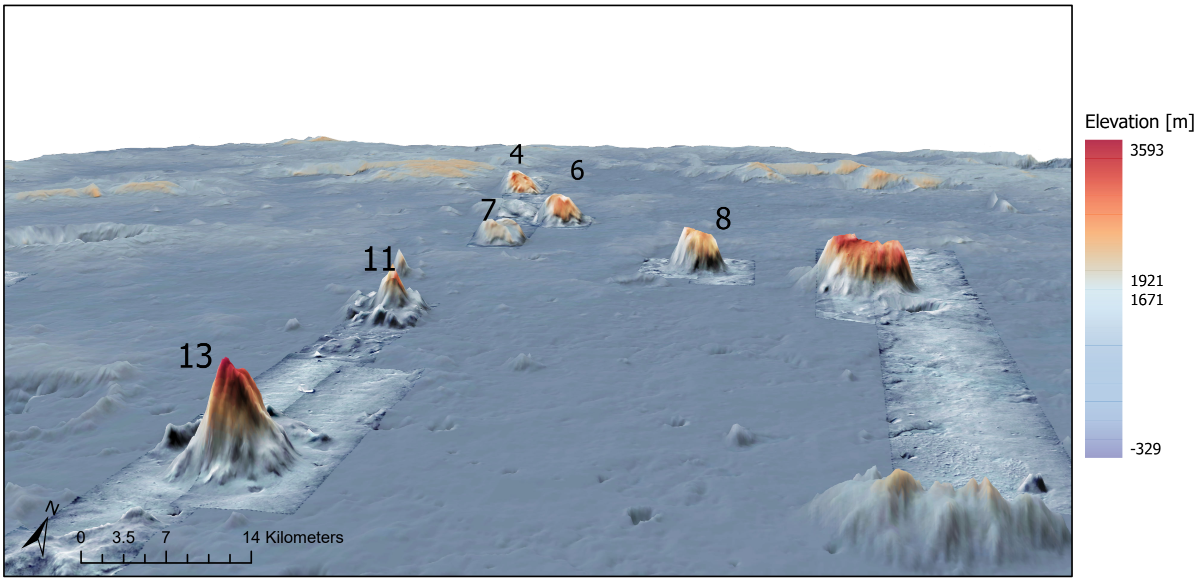

Figure 1.8: 3D rendering of some of the Sisyphi Montes in the Dorsa Argentea Formation on the Martian South Pole. MOLA topography overlain hillshade. Vertical exaggeration of 10. Visible swaths are CTX images with 6 m/pixel resolution over a swath of ≈ 30 km. Image IDs: P12_005845_1200_XI_60S358W, B09_013321_1175_XN_62S356W, P10_005067_1167_XI_63S356W, B06_011910_1156_XN_64S353W, B09_013255_1156_XI_64S352W, B06_011831_1132_XN_66S356W, B10_013532_1116_XN_68S354W, G11_022525_1113_XI_68S355W

As previously said, glaciovolcanic edifices can be used to reconstruct past ice sheets. On Earth, the passage zone is a clear identifier for the minimum palaeo ice thickness derived from tuyas (Smellie and Edwards, 2016). On Mars, however, this distinct feature is not yet accurately identifiable, due to the lack of high resolution images and in situ observations. However, an analysis of slope and curvature can be done to identify a knick point, where the steep slope of the mountain side transitions into a flat top. Curvatures at the transition points need to be convex (curved outwards) for a knick point to be present. The definition of a knick point used throughout this report is: *A abrupt change of gradient in the mountain profile reflecting different conditions and processes above and below the knick point*. With this, an approximate passage zone can be identified to be used in the reconstruction of a palaeo ice sheet that overlaid the edifices. It should be noted that the actual passage zone is probably lower than the knick point analysis predicts, since the lava cap is included in the knick point region, although it reaches above the passage zone.

Any mountain for which a clear knick point can be identified is referred to as tuya in this study, because a distinct flat top is present. As an example, the elevation profile of mountain 10 is shown in Figure 1.9a together with an image from the Mars Orbiter Camera (MOC) in Figure 1.9b, indicating how the elevation profile was drawn. From this profile a clear transition point from a steep slope to a flat top can be identified at both edges of the mountain. This specific mountain has been labelled as a tuya by Ghatan and Head (2002) previously and is also included in this study as tuya. Figure 1.10 shows the knick point region of the Herðubreið tuya in Iceland.

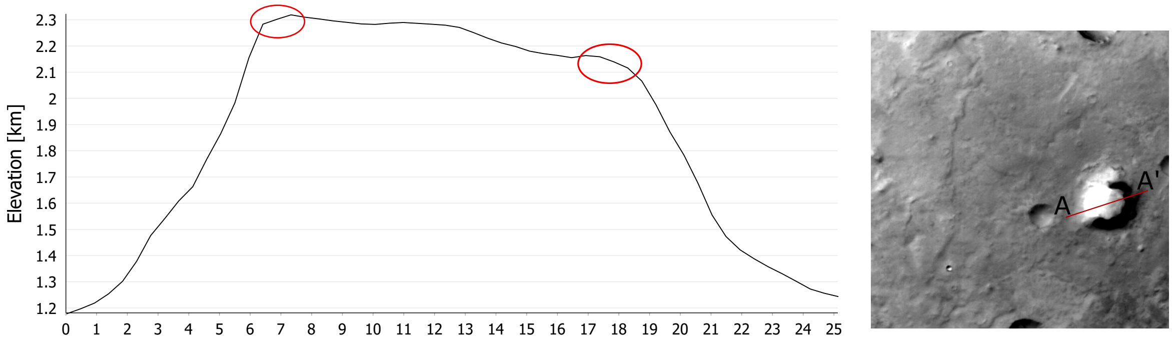

(b)

(a)

Figure 1.9: (a) Elevation profile of mountain 10 over a horizontal distance of 25 km. Red circles indicate the knick point at each edge. (b) MOC image M0307607. Red line indicates direction of elevation profile in (a). A at 0 km, point A' at 25 km.

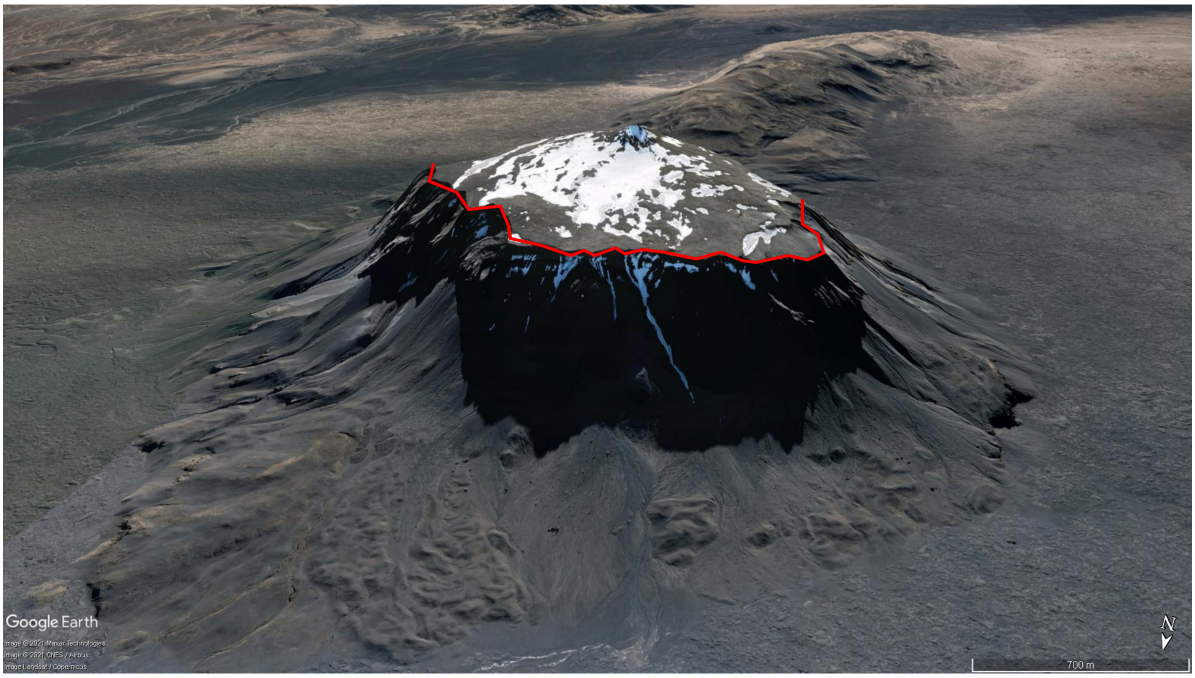

Figure 1.10: Google Earth Landsat/Copernicus image of the western face of the Herðubreið tuya in Iceland. Red line indicates the knick point location around the tuya edge. Image credits: Maxar Technologies and CNES/Airbus, 2021

1.3.1. Mars Obliquity Cycles

On current Mars, both poles are covered in ice with seasonal variations. Over one Martian year the ice extent changes due to the atmospheric deposition of the CO_2 ice on the north and south poles. The Martian climate is ultimately controlled by the solar energy distribution over the surface, comparable to Earth's Milankovitch cycles. Apart from the distance to the sun, three orbital parameters regulate this distribution: obliquity, eccentricity and the argument of perihelion (Mischna, 2018).

Obliquity, the angle between the orbital and equatorial plane, has the largest influence on the Martian climate (Mischna et al., 2003) and is the only parameter taken into account in this research. It is agreed that during periods of high obliquity ($>35^\circ$) the CO_2 ice from the polar caps would sublimate and redistribute to higher latitudes (Laskar et al. (2004a); Madeleine et al. (2014); Mansfield et al. (2018); Mischna (2018); Ward (1974)). A present day value of obliquity equal to 25.19°, comparable to Earth's spin axis orientation, is the reason that only Mars's poles are currently covered in ice. Over the course of Martian history, the resonance between orbital and spin axis lead to large variations in obliquity, much larger than on Earth (Mischna, 2018). We are able to derive the obliquity in the past by modelling the spin of Mars and how the torques on that spin have changed over time by interaction with other planets. Although there are no observations to verify these models on Mars, there is good agreement with estimates of past obliquities on Earth that are confirmed by observations[8].

Predictions of the obliquity are only accurate for the past 20 Myr on Mars, due to the chaotic behaviour of the solar system, Laskar et al. (2004a) derived a precise description of the parameter evolution beyond 500 Myr ago (Equation (25) from Laskar et al. (2004a)).

$$\epsilon_{\hat{m}} = 54.515 + 3.726\ln(t) - 0.583\ln^2(t) \tag{1.1}$$

Using the expression in Equation (1.1), the obliquity at t = 3.2 Gyr is 58.06°: large enough to host ice in mid-latitudes and covering even parts of the planets equator in snow and ice.

From simulations by Laskar et al. (2004a) a drop in obliquity could be detected about 4 Myr ago (Figure 1.11). Obliquity quickly changed from 35 to 25° (Laskar et al., 2004a) which, according to Bramson et al. (2017) caused most of the mid-latitude ice to retreat.

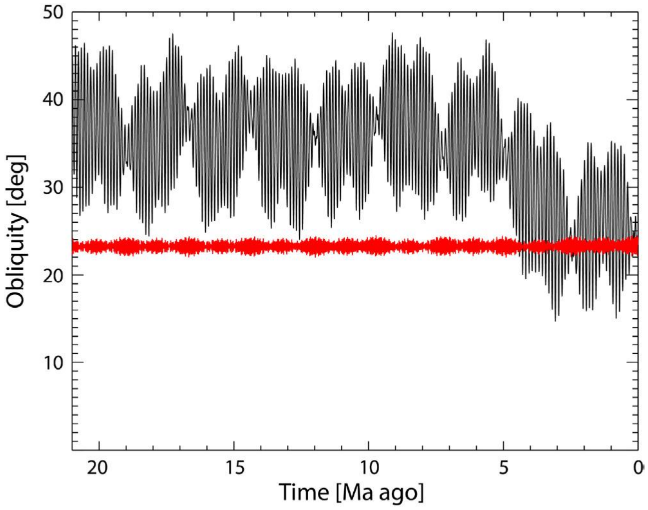

Figure 1.11: Obliquity evolution of Mars (black) and Earth (red) over the past 21 Myr. Data from Laskar et al. (2004a) and Laskar et al. (2004b). Figure taken from Mischna (2018).

Melting periods of past ice on Mars are highly uncertain, as Martian climate models are not able to accurately predict the conditions of 3.2 Gyr ago. There is agreement between researchers that one obliquity cycle from peak to peak takes about 120 kyr (Bramson et al. (2017); Laskar et al. (2004a); Madeleine et al. (2009)). During this period ice could melt and grow again in the mid-latitudes while obliquity is generally above 35°. The rate at which ice would melt on Mars is unknown at this point and assumptions need to be made for the ice history in models. Testing different deglaciation periods for ice at higher latitudes could also help to provide more

---

[8] SETI Institute. (2016). *The History of the Martian South Polar Cap - Carver Bierson*. Retrieved on October 16, 2021 from `https://www.youtube.com/watch?v=SSQ_exfk7GA`

insight into Mars' climate history and evolution. It must be noted that dust, porosity and water content also have an influence on melting. Furthermore, surface temperature, topography, thermal inertia, solar brightening, atmospheric pressure and radiative active clouds play a factor in the stability of ice in higher latitudes (Madeleine et al. (2014); Mischna et al. (2003); Mischna (2018); Mischna and Piqueux (2020)).

1.4. Martian Interior Structure

Mars' interior consists of a core, mantle and a crust as shown in Figure 1.12. Knowing the interior structure and composition provides insight into the planet's origin, as well as thermal and dynamic evolution (Cottaar and Koelemeijer, 2021). Seismic data from NASA's InSight mission have recently revealed that the Martian structure is different than previously estimated from gravity and topography. The new results provide us with essential information for future scientific research on composition and processes on the red planet (Khan et al. (2021); Stähler et al. (2021) and Knapmeyer-Endrun et al. (2021)).

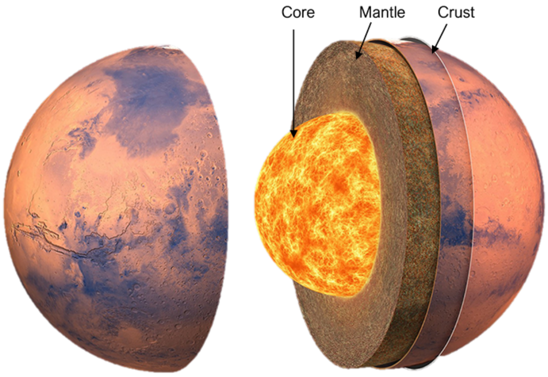

Figure 1.12: Artist impression of Mars' interior structure. Image credit: David Ducros/IPGP[9].

From local values of gravity and topography average crustal thicknesses between 30 and 80 km have been estimated (Wieczorek and Zuber (2004) and Neumann et al. (2004)). In recent studies, thicknesses of 45 to 57 km were reported for the southern Martian highlands (Bouley et al. (2020) and (Jiménez-Díaz et al. (2021)), making it thicker and stronger than the Northern Plain which is in agreement with the older age of the southern terrain. The boundary separating the Northern and Southern hemispheres is commonly known as Martian dichotomy (Robinson, 1995). More precise estimates of average crustal thickness between 24 and 72 km and densities < 3100 kg/m^3 were made with the new seismic data from InSight. It should be noted, that the seismometer is located in Elysium Planitia, just north of the Martian dichotomy and the data is most valid for this region of the planet. Furthermore, from signals bouncing off the core-mantle boundary it was shown that the core is larger than earlier thought. This implied that, given the known moment of inertia and mass of the planet, that the core's density is lower than previous values and in a liquid state. From the SEIS data a radius of 18830 ± 40 km and a density between 5700 to 6300 kg/m^3 were determined (Stähler et al., 2021).

Besides new insights into the crust and core, also the Martian mantle can be more clearly constrained. Studies revealed that the lower part of the Martian mantle is comparable to Earth's upper mantle. This observation makes Mars lack a dense insulating layer just above

---

[9] Sci-News. (2021). *NASA's InSight Lander Provides New Information about Crust, Mantle and Core of Mars.* Retrieved on September 25, 2021 from `http://www.sci-news.com/space/insight-crust-mantle-core-mars-09897.html`

the core (Cottaar and Koelemeijer, 2021). Analysis by Khan et al. (2021) showed that a lithosphere of about 500 km best matched the data.

As mentioned in Section 1.2, the lithosphere is defined as the fully elastic layer in the planet's internal structure, equivalent to that of an elastic plate and denoted at T_e. The lithosphere on Mars has been estimated using gravity and topography (Grott and Breuer (2008); Grott and Breuer (2010) and Steinberger et al. (2010)). Although lateral variations take place across the planet (Audet (2014) and Thor (2016)), it can be assumed that in a small area, such as the region of the Sisyphi Montes the lithosphere thickness is homogeneous, simplifying the modelling approach used.

Modelling the evolution of the lithosphere on Mars showed that during the Noachian and Hesperian epoch (3 Gyr ago), Mars had a thin lithosphere of 20-40 km and a strong thick layer between 70 and 900 km during the Hesperian-Amazonian epoch (Grott and Breuer (2008) and Grott and Breuer (2010)). Cooling of the planet is generally the reason for this change in lithosphere thickness.

Besides the change in thickness over time, estimates of lithosphere thickness depend on the time frame of the surface load. Phillips et al. (2008) predicted a lithosphere thickness underneath the Martian North Polar cap of more than 300 km based on Shallow Radar (SHARAD) images of the internal stratigraphy. Later, a new model by Grott and Breuer (2010), taking into account locally varying crustal thicknesses and the concentration of heat-producing elements estimated a T_e of 196 km at the North Pole at that time. The large variations in elastic thickness between the models show that variations in crustal thickness and the concentration of heat-producing elements have an influence on the elastic layer.

From the research conducted previously it can be concluded that taking into account two different lithosphere thickness is necessary to draw adequate conclusions on what influences geophysical processes inside Mars. Therefore, in this study a thick lithosphere layer, representative for Mars today and a thin layer, for modelling Mars 3.2 Gyr ago, are used.

1.5. Research Question, Aims and Objective

As explained in Section 1.2 the effect of deglaciation on the formation of glaciovolcanic edifices has thus far only been studied on Earth. The vast amount of in situ data and the accessibility of research sites make it much easier to model processes under the ice and in the deeper layers of the planet as compared to Mars.

Ongoing research on Mars has shown that glaciovolcanic edifices, similar to terrestrial tuyas, exist in the South Polar Region. Section 1.3 outlined that these edifices can be used to reconstruct the minimum thickness of a palaeo ice sheet by means of identifying a knick point region. Furthermore, since ice history models do not yet exist for Mars, estimates of the Martian obliquity can be used to approximated the ice history as explained in Section 1.3.1. This can be done more accurately using the knowledge about the interior structure of the red planet discussed in Section 1.4. With the enhanced knowledge about past, as well as present Mars, modelling of the deglaciation effects on volcanism is possible to certain extent and results can be compared to findings from research on Earth, specifically Iceland.

The objective of this study is to determine whether there exists a relationship between deglaciation and the eruption of subglacial volcanoes to form tuyas in the South Polar Region on Mars by reconstructing a former ice sheet analysing pressure changes in the mantle using a Finite Element Model.

To close the research gap, the following research hypothesis has been established:

> *The unloading of the Martian mantle, due to melting of a former ice sheet, has contributed to forming tuyas, glaciovolcanic edifices, in the South Polar Region on Mars.*

To explore the hypothesis and guide the research the following sub-questions are posed:

a) How can the elevation and spatial distribution of tuyas in the Dorsa Argentea Formation be used to constrain the minimum palaeo ice sheet thickness and minimum ice extent?

b) In what way can the ice sheet retreat period be derived from the spatial distribution of tuyas in the Dorsa Argentea Formation?

c) How does induced change in mantle decompression affect the mantle melt rate underneath the degrading ice sheet?

Answering whether deglaciation has had an effect on the formation of tuyas on the Martian South Pole can advance our knowledge on geophysical processes on Mars. Furthermore, results from this study can be compared to findings on Earth and investigating the similarities and differences to draw further conclusions.

1.6. Thesis Outline

In the first Chapter of this dissertation an introduction to the topic was provided. Chapter 2 covers the main part of the research and is written in the form of a draft journal article to be submitted to the Journal of Geophysical Research Planets. Section 2.1 includes an introduction and defines the research aim. After this, Section 2.2 the methodology and use of data is explained which gives a detailed overview of the Finite Element Model created. Results of this research are presented in Section 2.3 following a discussion of the findings and including model limitations in Section 2.4. The article is concluded in Section 2.5. To provide more details on the work done, Chapter 3 contains supplementary material that are used to support the main article. The dissertation ends with a conclusion in Section 4.1 and recommendations for future work in Section 4.2.

2

Journal Article

Deglaciation as a potential trigger for glaciovolcanism in the Martian South Polar Region

J.L. Wiese[1] et al.
[1] *Faculty of Aerospace Engineering, Delft University of Technology, Delft, the Netherlands*
(Corresponding author: J.L. Wiese, wiese.joanalisa@gmail.com)

Abstract: *Several mountains in the Martian South Polar Region qualify as tuyas. From the height and spatial distribution of these tuyas we reconstruct a palaeo ice sheet for this region. We find an optimum ice sheet radius of 600 km and an optimum ice divide height of 1754 m. The reconstructed ice sheet constrains the surface pressure load applied in the finite element model used to study glacially induced decompression rates within the Martian mantle. Our models show a decrease in decompression rates over depth and time for three linear deglaciation periods: 1 kyr, 30 kyr and 60 kyr. At 465 km below a thin lithosphere we find a decompression rate of 1450 Pa/yr induced by ice melt over 1 kyr. This decompression rate is equal to the maximum values under present-day Vatnajökull. Decompression rates can initiate mantle melting at a depth where the mantle temperature is close to the solidus, which is likely to occur at 465 km. For melt to reach the surface within the deglaciation period, magma ascent velocity needs to be sufficiently high. Assuming a velocity of 1000 m/yr, melt reaches the surface within 500 yr: faster than our deglaciation periods. Under these conditions and a warm, wet Martian climate, mantle unloading due to ice melt could have contributed to the formation of tuyas in the South Polar Region. In addition, our study proposes present-day deglaciation of Vatnajökull as a potential analogue for processes related to deglaciation on Mars.*

Keywords: *decompression rate, glaciovolcanism, mantle melt, Mars, tuya*

2.1. Introduction

The Sisyphi Montes (55°S - 75°S, 335°E - 40 °E) (Ackiss et al., 2019) lie within the Noachis Terra and Mare Australe quadrangles in the Southern hemisphere on Mars. Mapped by Tanaka and Scott (1987) and re-examined by Ghatan and Head (2002) a number of these mountains have been identified to potentially be of subglacial origin. Tanaka and Scott (1987) and Tanaka and Kolb (2001) have discussed possible interpretations of features and landforms in the Dorsa Argentea Formation and identified various features as lava flows or remnants of magma/volatile interactions. Furthermore, mineralogical evidence was found by Ackiss et al. (2018) (see also Campbell et al. (2016) and Ackiss (2019)) that the Sisyphi Montes are of glaciovolcanic origin. These studies provide additional evidence for magma-ice interactions on the red planet. Excellent preservation of morphologies and availability of high resolution MRO CTX images of single edifices make this region an interesting study area.

Furthermore, detailed mapping suggests that the Sisyphi Montes could have been covered by a large ice sheet, possibly an extent of the south polar ice cap (Head et al. (2007) and Head and Pratt (2001)). The surface age in the region has been estimated to be from the Hesperian epoch based on observed deposits (Head and Pratt, 2001).

Studies performed in Iceland and other regions on Earth have shown that the deglaciation of a former ice sheet causes an increase in volcanic activity (Jellinek et al. (2004); Jull and McKenzie (1996); Maclennan et al. (2002); Schmidt et al. (2013); Sigmundsson et al. (2010)). During deglaciation, additional magma generation can occur if the in situ pressure in the mantle decreases. This pressure decrease shifts the solidus temperature of the mantle material closer to (or below) the actual mantle temperature, causing it to melt (Schmidt et al., 2013). Under Vatnajökull during recent deglaciation a decompression rate of 1450 Pa/yr was found, causing an increase of up to 0.23 km^3/yr of magma (Schmidt et al., 2013). Furthermore, stress states changing in the crust due to the unloading can cause magma chamber instability and dyke propagation (Jellinek et al. (2004); Sigmundsson et al. (2010)) favouring subglacial eruptions. It is still unknown whether on Mars the same geophysical processes have contributed to subglacial eruptions, forming the tuyas in the South Polar Region.

In this study we therefore investigate the decompression rates induced by deglaciation inside the Martian mantle. We apply an ice sheet reconstructed from tuya heights in the Dorsa Argentea formation as a surface load and aim to find support for the following research hypothesis:

> *The unloading of the Martian mantle, due to melting of a former ice sheet, has contributed to forming tuyas, glaciovolcanic edifices, in the South Polar Region on Mars.*

Finding support for the research hypothesis can advance our knowledge on geophysical processes on Mars. Furthermore, we can compare results from this research to findings on Earth and investigating the similarities and differences to draw further conclusions.

First, we provide a more detailed introduction to deglaciation induced mantle melting on Earth from previous studies and briefly present their findings. In Section 2.2 an overview of the data used is given, followed by the method used to reconstruct the ice sheet from tuya heights and the final result of the reconstruction (Section 2.2.3). After this, we explain the finite element(FE) model setup and the model geometry in Section 2.2.4. Presentation and evaluation of the resulting decompression rates is done in Section 2.3 and Section 2.4, respectively. Finally, conclude our research and provide future research directions in Section 2.5.

2.1.1. The Effect of Deglaciation on Magma Production on Earth

Mantle melting due to glacially induced decompression rates can only occur when the solidus temperature of the material is equal to or below the actual mantle temperature. Iceland makes a great study case for this process, as it lies above a spreading ridge where temperatures are already high due to the presence of hot mantle plumes.

Jull and McKenzie (1996) modelled an ice sheet with a radius of 180 km to estimate the decompression rates in the Icelandic mantle over a deglaciation period of 1 kyr. They found a maximum $\frac{dP}{dt}$ of 19 kPa/yr right below the lithosphere at the loading centre. We note, that this deglaciation took place during the Pleistocene-Holocene boundary when the ice sheet covered the entire country. Jull and McKenzie (1996) found that these induced decompression rates can cause an increase in melt production in the mantle of 3.5 km^3/yr, which is 30 times more than during glacial or postglacial periods. However, the enhancement in volcanism is largely dependent on magma ascent velocity. For their study they propose that melt would reach the surface within 1 kyr.

In the study by Schmidt et al. (2013), they estimated a maximum decompression rate of 1450 Pa/yr underneath Vatnajökull ice sheet in Iceland during the recent deglaciation between 1890 and 2010 (120 yr). They found additional generation of magma of 0.21-0.23 km^3/yr, comparable with previous estimates by Pagli and Sigmundsson (2008) of 1700 Pa/yr.

The resulting pressure changes in Iceland were small and led to small changes in melting temperature (less than $\frac{1}{10}$ of a °C) (P. Schmidt, personal communication, October 5, 2021). For melting to take place, it is therefore necessary for the temperature of the mantle and the melting temperature to be close to each other, before the decrease in pressure starts.

The mentioned studies in Iceland take a potential temperature of the mantle (T_{pot}) equal to 1500° C and observed that higher potential temperatures in the mantle, shift the initiation of melting to a lower depth (Schmidt et al., 2013). Furthermore, the bulk water content also has an influence on the generation of melt: the melting occurs at a lower depth for dryer, colder models than for hotter, wetter models. We note that the temperature and composition of the mantle are a large factor for deglaciation induced mantle melting, but due to Mars' lower gravity melt production will potentially occur over a larger depth than on Earth and even material deep inside the mantle could start to melt (D. McKenzie, personal communication, May 30, 2021).

An alternative process that could favour the eruptions under thick ice and formation of tuyas on Mars is related to magma chamber instability and dyke formation. It has been found that glacial loading may suppress volcanism by trapping magma in the upper crustal layer of the lithosphere. During unloading of the surface the stresses relax and the accumulated magma is released (Wilson and Russell, 2020). Furthermore, studies showed that glacially induced crustal stresses can cause instabilities in magma chambers in the lithosphere. In addition, these induced stresses restrict or enhance dyke formation, influencing the magma transport to the surface (Jellinek et al. (2004); Mora and Tassara (2019)).

These findings can help draw a conclusion on the processes taking place on Mars, as discussed hereafter.

2.2. Method and Data

2.2.1. Topography Data and Surface Images

To investigate the glaciovolcanic edifices in the region of interest we use data from the Mars Global Surveyor spacecraft that operated from 1996 till 2006[1] and provided laser altimetry data from the Mars Orbiter Laser Altimeter (MOLA) which was used to generate a global topography map of the planet. For the research at hand, MOLA Mission Experiment Gridded Data Records (MOLA MEGDR) with a map resolution of 128 pixels/deg are used. The vertical resolution of the altimetry data is 40 cm and 300 m along-track. The products use an areocentric coordinate system which is based on the IAU2000 cartographic standard (Smith et al., 2003). For analysis, the topography raster datasets are processed in the geo-processing software ArcGIS Pro. An Albers Equal Area map projection is applied which has been newly created from the Mars2000 geographic coordinate system available in ArcGIS Pro.

In addition to the MOLA topography data, Mars Reconnaissance Orbiter (MRO) Context Camera (CTX) images are used for 3D high resolution rendering and visual inspection of the edifices to help identify the knick points and with this the possible passage zone (PZ) elevation. CTX provides images of the planet at 6 m/pixel scale over a swath of approximately 30 km wide.

2.2.2. Ice Load History from Obliquity

The Martian climate is predominantly controlled by solar insolation of the surface, comparable to Earth's Milankovitch cycles. the distribution of solar energy is regulated by three of the planets orbital parameters: obliquity, eccentricity and argument of perihelion. On Mars, obliquity has the largest influence on the climate (Mischna et al., 2003). Simulations over the past twenty five million years have shown that periods of high obliquity were present between 20 Myr to 4 Myr ago (Laskar et al., 2004a). Research agrees that due to the change in Mars' spin axis over time the ice from the poles travels to mid-latitudes when obliquity exceeds the 35°

---

[1] NASA Science (n.d.). *Mars Global Surveyor*. Retrieved on May 20, 2021 from `https://mars.nasa.gov/mars-exploration/missions/mars-global-surveyor/`

mark and returns to the poles once obliquity decreases again (Mischna et al. (2003); Mischna (2018) and Madeleine et al. (2014)).

Analytical solutions of obliquity for more than 20 Myr ago do not exist, due to the chaotic behaviour of the solar system. Nevertheless, Laskar et al. (2004a) have performed an extensive statistical analysis of the Martian orbital and rotational evolution. They found an average obliquity of 37.62° over 5 Gyr with a maximum of 82.035°. This study therefore assumes that during the eruption period of the Sisyphi Montes, about 3 Gyr ago, obliquity was high (>35°). This assumption favours the accumulation of ice in higher latitudes on early Mars, and covers the region of interest under an ice sheet.

We further assume that the obliquity behaviour in the past was similar to precise solutions over the past 20 Myr by Laskar et al. (2004a). An obliquity drop from 35° to 25° has been observed at about four million years ago, which according to research by Bramson et al. (2017) caused most of the ice retreat in mid-latitudes. Although this drop caused the largest ice loss, smaller oscillations in obliquity also affect ice retreat and growth (Bramson et al., 2017). One obliquity oscillation from peak to peak has been estimated to be 120 kyr (Bramson et al. (2017); Laskar et al. (2004a); Madeleine et al. (2009); Schorghofer (2007)). Based on this, the period of ice retreat is about 60 kyr (peak to trough).

Since climate variations are still very difficult to predict on Mars, we take three different time periods during which the reconstructed ice sheet melts linearly over time: 60 kyr, 30 kyr and 1 kyr. The longest retreat period is based on the peak to trough period of the obliquity oscillation as mentioned earlier. We expect shorter retreat periods to result in larger decompression rates in the mantle, which is favourable for mantle melting. We therefore halve the melting period and also investigate an extreme case of 1 kyr, that could have occurred in a warmer, wetter Martian climate in the past. In addition, deglaciation in Iceland during the last glacial maximum has been modelled as 1 kyr and can be used as a comparison study Jull and McKenzie (1996). To reduce simulation times, a period of 2 Myr is taken during which the ice is stable on the surface, which is about $\frac{1}{8}$ of the 16 Myr of high obliquity estimated by Laskar et al. (2004a).We do not take into account any possible seasonal variations in ice thickness or increased melt due to volcanic activity underneath the ice sheet.

The Sisyphi Montes are clustered in a small area close to the south polar ice cap and it can be assumed that during the periods of high obliquity the entire area was covered in ice, instead of just high topography locations. We do note that factors such as surface temperature, topography, atmospheric pressure and even radiative active clouds influence the distribution of ice across the Martian surface (Madeleine et al. (2014); Mansfield et al. (2018); Mischna et al. (2003)). With more accurate climate models and better knowledge about the surface composition of early Mars, predictions about the ice history can be improved in future studies.

2.2.3. Ice Sheet Reconstruction from Tuya Heights

The ice sheet reconstruction is done using a fitting approach with the goal of the optimisation is to find the optimum ice (divide) height (H_0) above the base elevation and optimum location (Δx) of the ice sheet with respect to the tuyas, such that for all tuyas the distance between the maximum possible passage zone elevation and the ice height is minimised. With this, we can determine the thickest ice sheet possible that can be derived from the passage zone elevations of the tuyas.

In this study we use nine of the twenty one mountains analysed by Ghatan and Head (2002) to reconstruct a former ice sheet that overlaid the volcanoes. Making use of slope and profile curvature analysis of the individual mountains we determine a knick point area at which the steep slope transitions into a flat top. From this, we are able to infer a maximum elevation for a possible passage zone (PZ), the transition zone between subaqueous and subaerial lithofacies.

On Earth, this transition zone provides an indication for the minimum ice sheet thickness before eruption (Smellie and Edwards, 2016) and we therefore apply this relation between PZ elevation and ice sheet thickness in our study on Mars, as well.

The edifices used in the reconstruction are chosen based on whether they would lie close to a straight line in North-South (NS) (Figure 2.1b) or West-East (WE) (Figure 2.1a) direction (hereafter referred to as NS line and WE line). We have used these lines to pragmatically constrain the axes of the ice sheet architecture, which in turn determined the shape of it. For the NS line, mountains 1, 4, 6, 7 and 11, were used, whereas the WE line included mountains 7, 8, 10, 12 and 14 (Figure 2.2b). Mountain 3 and 5 on the NS line, labelled in Figure 2.2a with a red cross, have been identified as outliers due to their relatively low height. This difference could be indication for different eruption periods, i.e. that mountains 3 and 5 would be younger than the rest and erupt after the ice had already decayed a certain amount. We assume that all other mountains have formed in the same period and are of similar age. By superimposing the mountains onto the NS and EW lines, their elevations are used to fit the ice profile height.

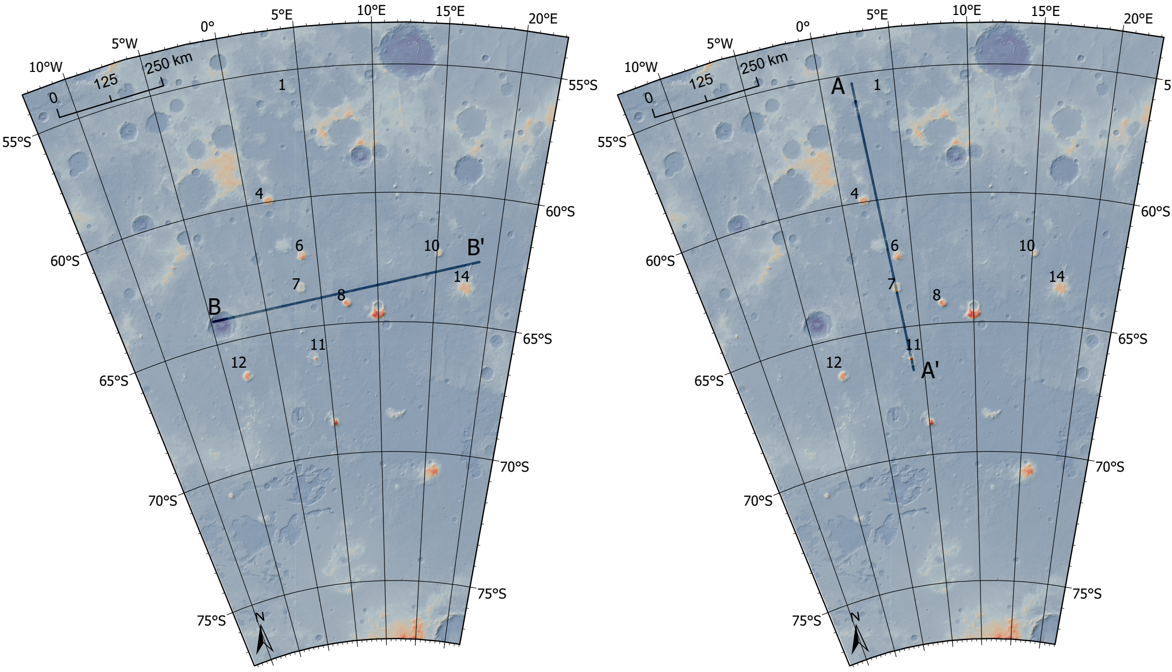

(a)

(b)

Figure 2.1: MOLA colour topography overlain hillshade of Sisyphi Montes on the South Polar Region on Mars. (a) Line in West-East direction (B-B′) on which mountains 7, 8, 10, 12 and 14 are superimposed. (b) Line in North-South direction (A-A′) onto which mountains 1, 4, 6, 7 and 11 are superimposed.

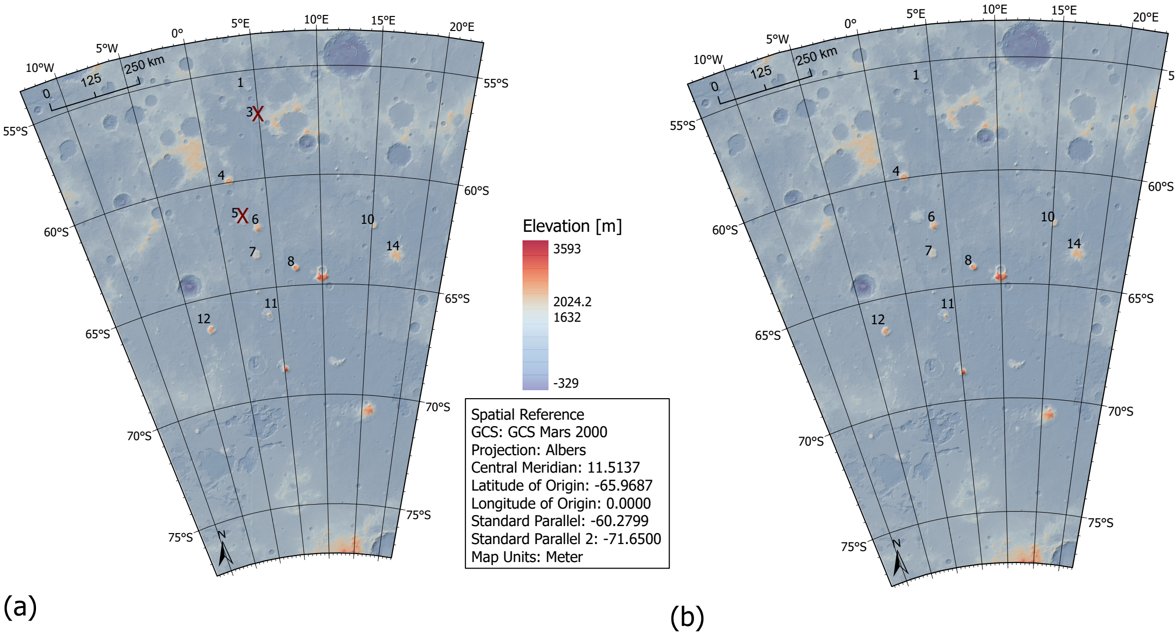

Figure 2.2: MOLA colour topography overlain hillshade of Sisyphi Montes on the South Polar Region on Mars. Spatial reference given in the figure. (a) Includes mountains 3 and 5 that are marked with red crosses as outliers. (b) Mountains are included in the ice sheet reconstruction.

For each of these remnants a base elevation of 1200 m has been assumed above which slope and curvature are analysed to determine the knick point region and extract the possible passage zone elevation. In addition, we compute the ice height with respect to this base elevation and assume a flat ice sheet base at 1200 m, neglecting topography variations. This assumption is supported by the fact that the surrounding topography is fairly even, without significant topographic extremes as observed in Figure 2.3.

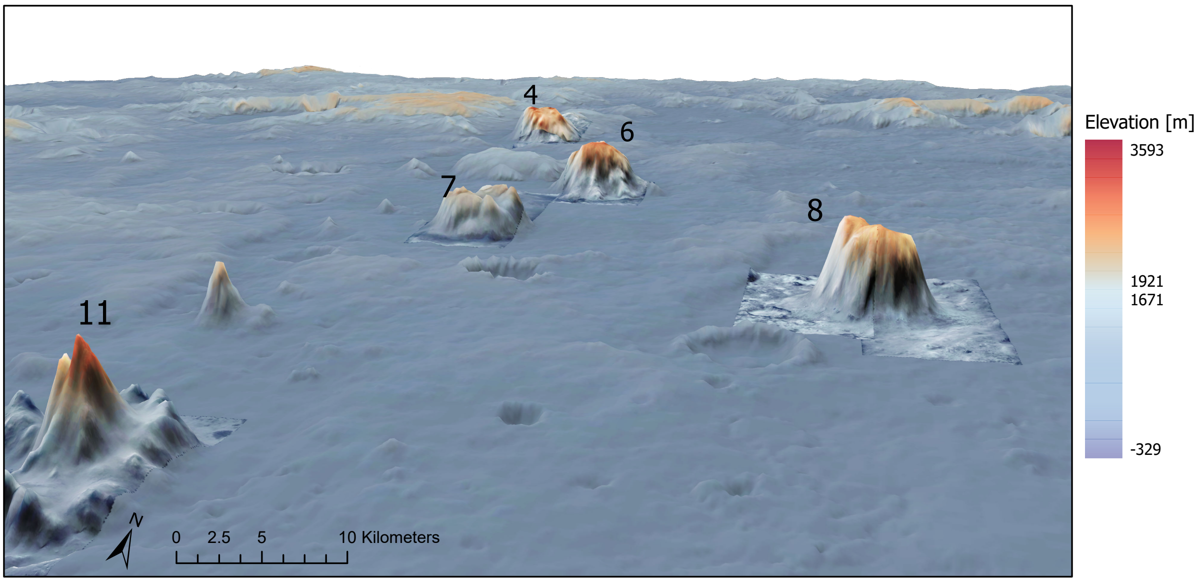

Figure 2.3: 3D rendering of six of the Sisyphi Montes in the Dorsa Argentea Formation used in this study. MOLA topography overlain a hillshade layer. Vertical exaggeration of 10. Visible swaths are high resolution CTX images: P12_005845_1200_XI_60S358W, B09_013321_1175_XN_62S356W, P10_005067_1167_XI_63S356W, B06_011910_1156_XN_64S353W, B09_013255_1156_XI_64S352W, B06_011831_1132_XN_66S356W

For each mountain, the average flank slope is taken as the mean of mountain slopes from two previous studies (Ghatan and Head (2002); Fagan et al. (2010)), see Table 2.1. Any cell of the raster data set with a higher slope value than the average flank slope (per mountain) is included in the knick point inspection.

Table 2.1: Average flank slope of selected mountains in the Dorsa Argentea formation on Mars.

Mountain	Ghatan and Head (2002)	Fagan et al. (2010)	Mean both studies
1	5.4°	5.72°	5.56°
4	7.76°	8.32°	8.04°
6	9.14°	11.21°	10.18°
7	8.34°	8.58°	8.46°
8	11.29°	15.22°	13.26°
10	10.4°	10.66°	10.53°
11	7.46°	7.93°	7.695°
12	8.36°	10.54°	9.45°
14	6.45°	3.67°	5.06°

Profile curvature measures the geometric normal curvature along the mountain's slope line. For our analysis we only use positive profile curvatures which indicate a convex surface in the direction of the slope. Cells that exhibit positive profile curvatures form a region around the mountain top where the slope transitions from steep to flat. This transition zone is called a knick point zone hereafter. When the surface is flat a value of zero is found for the profile curvature which we expect to be mostly in the centre of the summits [2].

For each of the remnants in this study we combine the slope and profile curvature and visually identify the knick point zone where cells of highest slope and curvature values meet. (Figure 2.5a). Firstly, Figure 2.4a shows the slope of mountain 6 in a 3D render. Values below 10.18° are coloured in grey and are therefore not visible. Steepest slopes (dark green) can be identified at the top edge of the mountain. Secondly, the profile curvature for the same mountain is displayed in Figure 2.4b with a maximum curvature of 2.9x10^{-4}m^{-1} in dark blue.

In Figure 2.5a both, slope and profile curvature are displayed together and we observe that highest slope and highest curvature meet at the edge of the mountain top (dark green and dark blue are neighbouring cells). From this, a ring-shaped area for the kick point zone is determined (pink area in Figure 2.5b). We extract the elevation values of all cells within this area, which gives us a maximum and minimum elevation. In the supplementary material in Section 3.1 we provide a flow chart showing the steps to obtain slope and curvature profile values in ArcGIS Pro and how to apply a feature class to draw the ring-shaped kick point zone and extract elevations.

---

[2] Esri (n.d.). *Surface Parameters (Spatial Analyst).* Retrieved on October 31, 2021 from `https://pro.arcgis.com/en/pro-app/2.7/tool-reference/spatial-analyst/surface-parameters.htm`

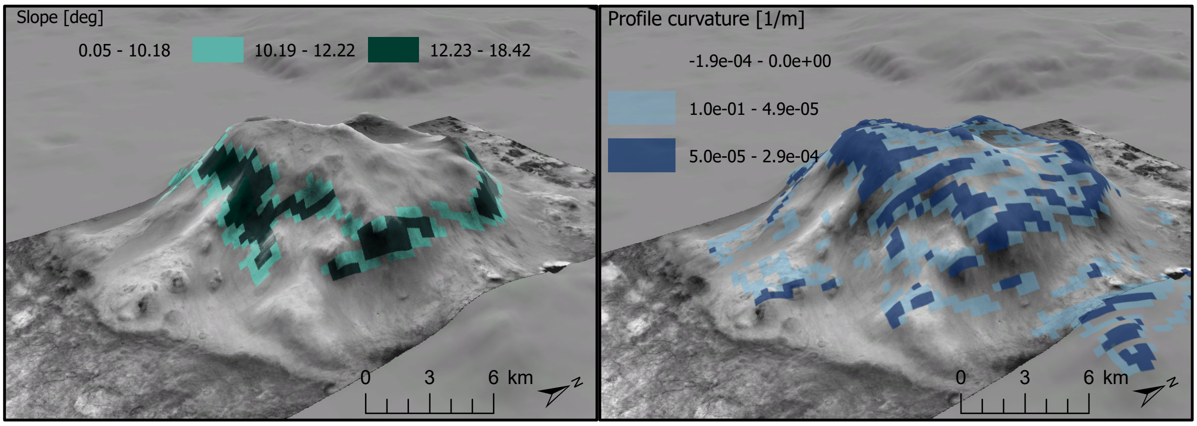

(a) (b)

Figure 2.4: MOLA topography derived hillshade overlaid by CTX image B09_013321_1175_XN_62S356W rendered in 3D of mountain 6. (a) Slope in degree. Values below 10.18°are coloured grey and not visible. (b) Profile curvature in 1/m. Negative curvatures indicate concave profiles and are coloured grey (not visible in the render).

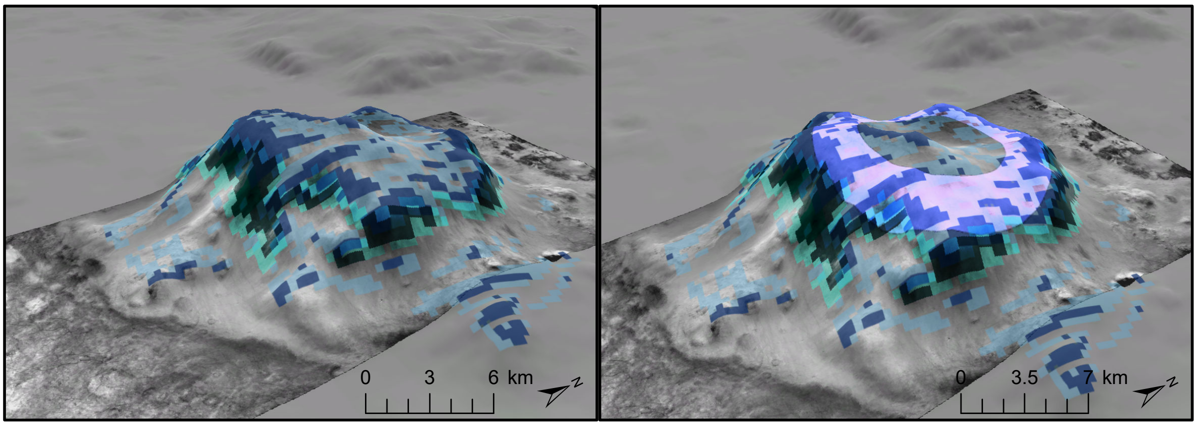

(a) (b)

Figure 2.5: MOLA topography derived hillshade overlaid by CTX image B09_013321_1175_XN_62S356W rendered in 3D of mountain 6. (a) Slope and profile curvature combined. (b) Combination of slope and profile curvature with the pink area indicating the possible passage zone region.

We identify a clear knick point zone for all mountains listed in Table 2.1, therefore all mountains fit our definition of a tuya. We may use the terms mountain and tuya interchangeably. From the ring-shaped areas for the kick point zone, the elevation values have been extracted and we call the range between minimum to maximum elevation the passage zone range. This is the potential range of elevation in which the tuya passage zone could lie. Using the knick point region as indication for the PZ elevation introduces a small overestimation. This is, that the lava cap on the top of the tuya is included in our approximation of the passage zone elevation. During the tuya formation the cap lava always forms above the passage zone. However, passage zone elevation provides an indication for the minimum palaeo ice sheet thickness (Smellie and Edwards, 2016). As we aim to derive the thickest ice sheet possible from the tuya heights, this slight overestimation does not affect our results and conclusions, as the ice could have always been thicker than the passage zone indicates.

We further note a minimum value of 2.94x10^{-4} m^{-1} for the profile curvature for tuyas 14 and 6. Denoting them as tuyas in our study is in line with their previous identification as flat-topped by Ghatan and Head (2002). We propose that this minimum profile curvature value could be used in future studies to help identify tuyas on Mars.

We then compare these passage zone ranges between the individual tuyas in NS and WE direction by means of notched box-plots (Figure 2.6 and Figure 2.7). We observe that in the NS direction tuyas 1 and 11 have a similar passage zone elevation range. Their mean and even the maximum PZ elevation is lower than for tuyas 4, 6 and 7, which indicates that edifice 1 and 11 have formed at the edges of the ice sheet, where ice sheet thickness is smaller.

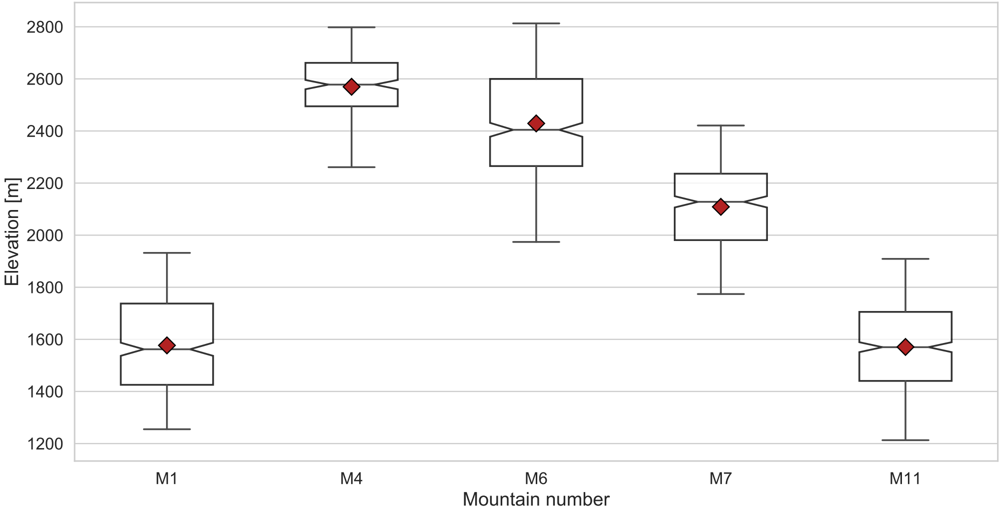

Figure 2.6: Notched boxplots of identified passage zone elevation ranges for mountains 1, 4, 6, 7 and 11 along the NS line. Red diamond indicates the mean elevation and the notch marks the 95% confidence interval of the median. Whiskers mark the minimum and maximum data points.

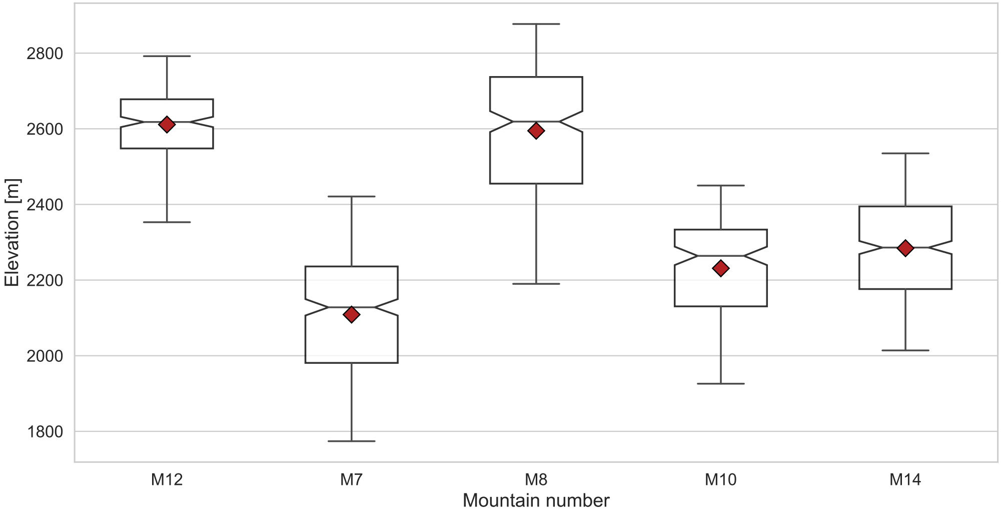

Figure 2.7: Notched boxplots of identified passage zone elevation ranges for mountains 7, 8, 10, 12 and 14 along the WE line. Red diamond indicated the mean elevation and the notch marks the 95% confidence interval of the median. Whiskers mark the minimum and maximum data points.

The PZ elevation ranges for the remnants on the WE line are on average higher than along the NS line. Again, we observe that two of the tuyas (10 and 14) have similar PZ elevation ranges with mean elevations between 2100 to 2300 m. Both tuyas lie on the most east edge of the WE line which again is good indication that they breached the ice at its edge. We note that tuya 7 has a much lower average passage zone elevation than its neighbouring tuyas 12 and 8. Nevertheless, its maximum PZ elevation lies above the minimum PZ elevations of the neighbouring tuyas which makes it less likely to have formed at the ice sheet edge like tuya 10 and 14. In addition, the PZ elevation range of tuya 7 fits well within the elevation ranges of its neighbouring tuyas on the NS line (Figure 2.6) and is therefore not considered an outlier.
We have successfully obtained minimum and maximum passage zone elevation per tuya and added a 120 m margin to the maximum value to take into account any fractured ice that could have been present during eruption time and/or surface sagging during melting (Smellie and Edwards (2016); Smellie et al. (2011) and Smellie (2018)). The final passage zone elevation ranges per tuya plus the margin can be found in Figure 2.8 and Figure 2.9 for the NS and WE line, respectively.

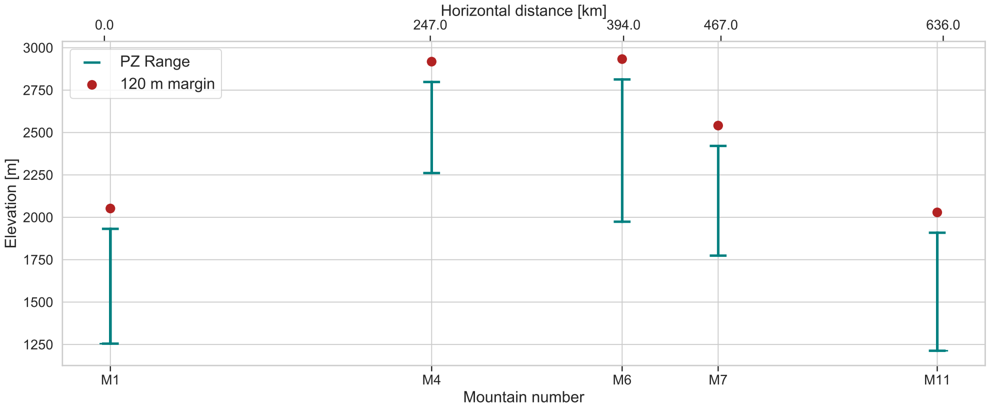

Figure 2.8: Passage zone elevation range for mountains 1, 4, 6, 7 and 11. The red dot indicates the 120 m margin above the maximum passage zone elevation. Horizontal distance is measured with respect to the most northern mountain, mountain 1.

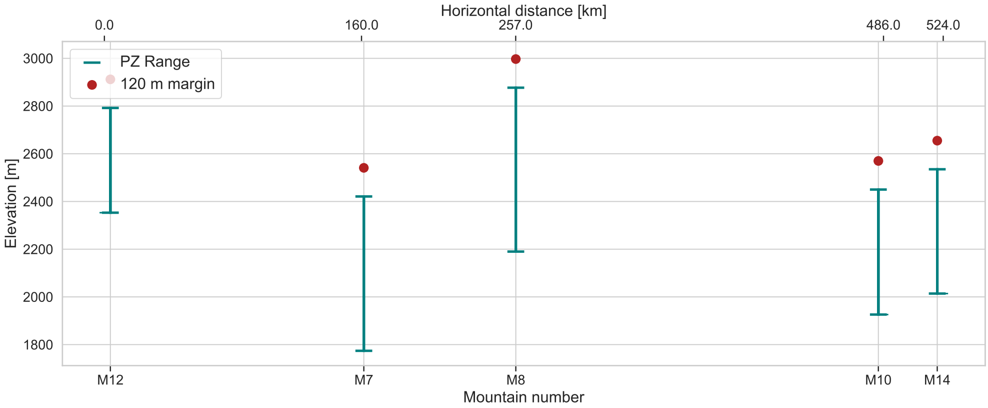

Figure 2.9: Passage zone elevation range for mountains 7, 8, 10, 12 and 14. The red dot indicates the 120 m margin above the maximum passage zone elevation. Horizontal distance is measured with respect to the most western mountain, mountain number 12.

We approximate the ice sheet as a perfectly plastic glacier. This approximation is often used in modelling, especially when the modelled ice sheets are large (van der Veen, 1999). As mentioned earlier, we assume a flat ice base which is warranted by the fairly even surrounding topography (Figure 2.3).

With the perfectly plastic glacier approximation it possible to estimate the profile of the ice sheet as a square root function (Equation (2.1)) (van der Veen, 1999). *L* is the radius of the ice sheet and H_0 the ice divide height.

$$H = H_0\left(1 - \frac{x}{L}\right)^{\frac{1}{2}} \tag{2.1}$$

The ice sheet is assumed to be circular with a fixed radius of *L* = 600 km for the fitting process. The fixed radius is based on the spatial distribution of the tuyas in the region of interest. In addition, it is sufficiently large to also cover other edifices in the region that might be of glaciovolcanic origin (Ghatan and Head (2002) Fagan et al. (2010)), but were not included in this study. For the tuyas in our study we have found a distance of 636 km between the most northern and most southern tuya and a distance of 524 km between the most western and most eastern tuya. The ice sheet radius of 600 km makes sure that the entire ice extent is always larger than the largest distance between the tuyas on the NS and WE line.

A schematic drawing of the ice profile of Equation (2.1) is given in Figure 2.10.

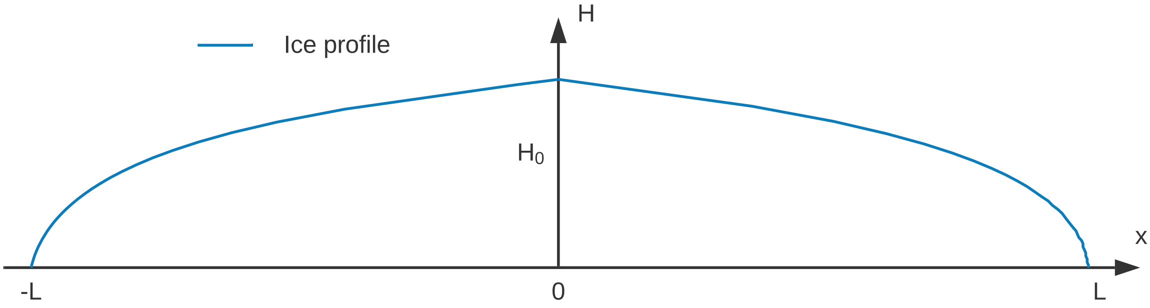

Figure 2.10: Schematic drawing of the perfectly plastic ice profile. H_0 marks the ice divide height. L is the ice sheet radius.

We assess five different values of ice divide height (H_0) and ten different Δx values along both, the NS and WE line. This leaves us with fifty different combinations along each line to determine the optimum ice divide height and ice sheet location. We assume that H_0 is determined by the passage zone elevation range of the tallest tuya on the NS or WE line. This assumption guarantees to find the thickest ice sheet possible which is the goal of the optimisation. Δx is taken as the x-location of the north most (M1) or west most (M12) mountain underneath the ice sheet. Following constraints have been set for the optimisation:

1. L is fixed to 600 km: $L = 600$
2. Δx must be between $-L$ and $L - L_m$ (length of NS or WE line): $-L <= \Delta x <= L - L_m$
3. H_0 must be between the minimum and maximum passage zone elevation of the tallest mountain on the NS or WE line.

Based on these constraints the ice heights tested in NS and WE direction are slightly different, as the maximum and minimum passage zone elevation of the tallest mountain on the NS line are different compared to the ones on the WE line (Figure 2.8 and Figure 2.9). An overview of the five ice divide heights used for testing along each line is provided in Table 2.2.

Table 2.2: Testing ice divide heights for ice sheet profile over NS and EW mountain ranges.

H_0 NS [m]	H_0 WE [m]
1111	1203
1272	1357
1432	1512
1593	1666
1754	1821

We exclude scenarios instantly that do not meet the minimum constraints set for finding the optimum ice height from tuyas. This means, when the ice height at a certain tuya lies below the minimum passage zone elevation of this tuya the scenario is discarded. An example of such can be found in Figure 2.11. By doing so, we are left with 13 possible combinations of ice divide height and ice location from the fitting in WE direction and 33 possible combinations from the fitting in NS direction.

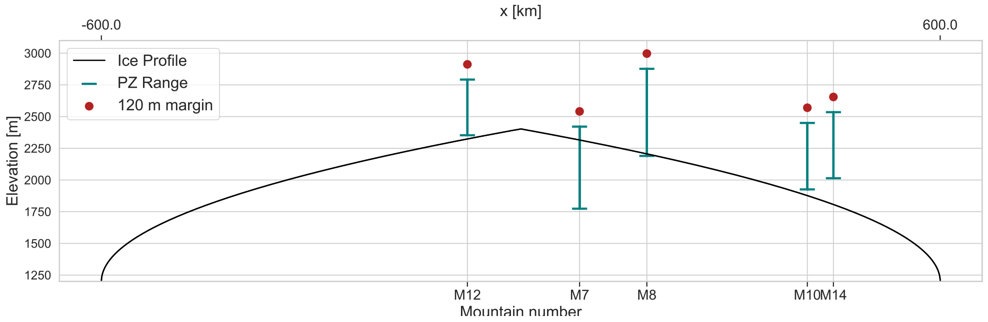

Figure 2.11: Suboptimum scenario of ice profile over mountain range in WE direction. Ice height at mountains 10, 12 and 14 lies below the minimum passage zone elevation.

Statistical evaluation using the Mean Absolute Error (MAE) of the test scenarios leads to an optimum choice for the ice divide height and location. We calculate the MAE with Equation (2.2). n is the number of mountains along the WE or NS line (Figure 2.9 and Figure 2.8), h_m is the height of the ice sheet at mountain i and z_m is the elevation of the margin point of mountain i. We only consider the MAE of the difference between the ice height and the margin elevation of 120 m above the maximum possible passage zone elevation to achieve the thickest ice sheet possible.

$$\text{MAE} = \frac{\sum_{i=1}^{n} |(h_m)_i - (z_m)_i|}{n} \tag{2.2}$$

Looking at the initial fitting of the ice sheet over the mountains in NS and WE, we observe that the largest ice height in both directions provides us the smallest mean absolute error (Figure 2.12 and Figure 2.13). Specifically, scenario 4 and 5 for the NS line and scenario 4 for the WE line.

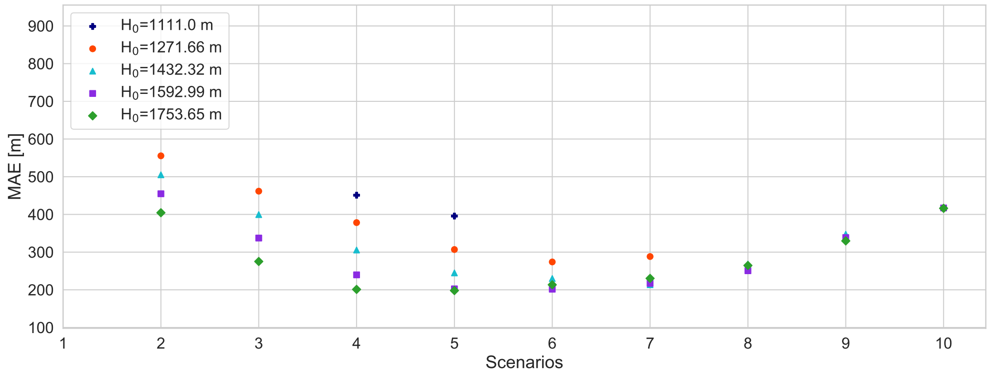

Figure 2.12: Mean absolute error of possible ice sheet heights over mountains on the NS line The scenario number describe the location of the ice sheet over the mountains.

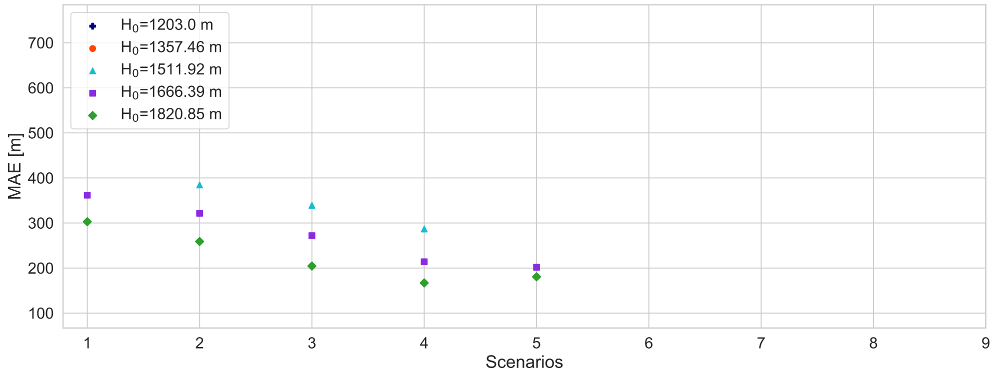

Figure 2.13: Mean absolute error of possible ice sheet heights over mountains on the WE line. The scenario number describe the location of the ice sheet over the mountains. Scenarios 6 to 9 were suboptimum and thus excluded.

From this first analysis, two optimum scenarios for the ice height have been selected for further optimisation: H_0 = 1754 m from the NS line and H_0 = 1821 m from the WE analysis. In a second optimisation run, these two ice heights are fitted over the NS and WE tuyas to determine an optimum location of the ice sheet and select a final divide height and location. To recall, the goal of the optimisation is to find the optimum ice divide height (H_0) above the base elevation and optimum location (Δx) of the ice sheet with respect to the tuyas, such that for all tuyas the distance between the maximum possible passage zone elevation and the ice height is minimised. Base on the mean absolute error between ice height and passage zone elevation, the new scenario 4 from the second optimisation run achieves the best fit for both ice divide heights (Figure 2.14 below). Overall, we achieve a slightly better fit for the ice sheet profile over the tuyas on the WE line. As the difference between the MAE of EW and NS fit for H_0 = 1754 m is smaller than for H_0 = 1821 m, the optimum ice divide height that gives the thickest possible ice sheet is taken to be 1754 m and the ice midpoint is located just above tuya 8 at 7°E, 63.8°S on the WE line (Figure 2.15).

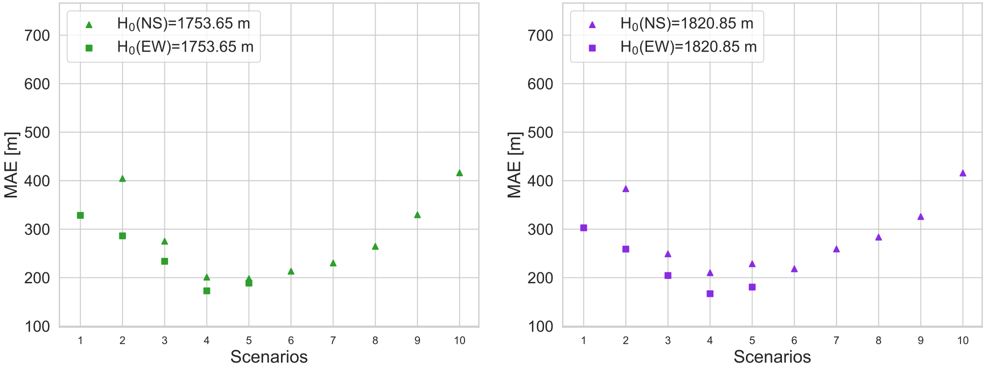

Figure 2.14: Mean absolute error for two ice divide heights (left) H_0 = 1754m and (right) H_0 = 1821 m over the tuyas on the NS and WE line.

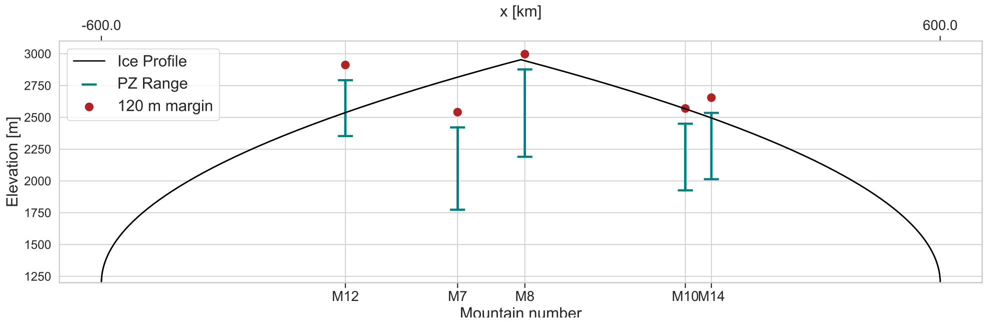

Figure 2.15: Optimum ice sheet profile over passage zone elevation ranges of mountains 7, 8, 10, 12 and 14 including a 120 m margin for fractured ice and snow layers.

The radius of the circular ice sheet is 600 km, which is sufficient to also cover other edifices in the region that might be of glaciovolcanic origin, but were not included in this study. The total area of the ice sheet is 1.13x10^6 km^2. The optimum circular ice sheet over the Sisyphi Montes is shown in Figure 2.16 and Figure 2.17 in an Albers Equal Area projection, which slightly elongates the circular shape in east-west direction towards an elliptical shape.

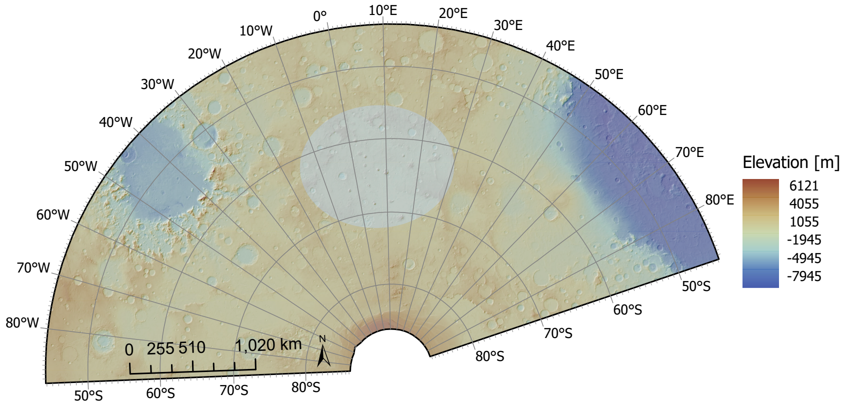

Figure 2.16: MOLA topography overlain hillshade with reconstructed ice sheet over Sisyphi Montes in the South Polar Region in an Albers Equal Area projection between 80°W to 90°E and 50°S to 80°S. Symbology of elevation uses a minimum maximum stretch type and a gamma value of 0.8.

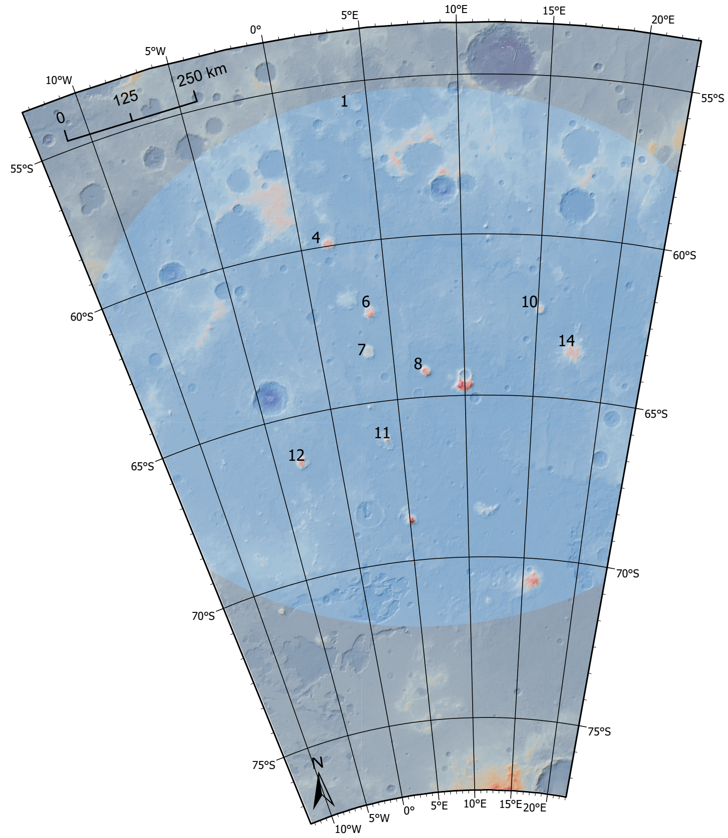

Figure 2.17: MOLA topography overlain hillshade with reconstructed ice sheet over Sisyphi Montes in the South Polar Region in an Albers Equal Area projection between 10°W to 20°E and 55°S to 75°S. Tuyas used in the ice sheet reconstruction are numbered. The ice midpoint location is above tuya 8 at 7°E, 63.8°S.

2.2.4. Mars Finite Element Model

We use a flat, symmetric finite element (FE) model to study decompression rates in the Martian mantle. We focus on the maximum decompression rates observed and compare the order of magnitude with results from a study in Iceland as outlined in Section 2.1.1.

Mars is modelled as an incompressible elastic lithosphere that overlies an incompressible Maxwell viscoelastic mantle. Self-gravity is neglected, which implies that the deformation due to changes in the gravity field are not taken into account, and so is self-gravity of the ice sheet. On Earth, the latter has an effect on sea level change, however, for modelling Mars, sea-level is not relevant and a non-self-gravitating FE model is appropriate. The ice sheet is modelled as perfectly plastic circular cap as explained in Section 2.2.3. The modelling software Abaqus is used (Simulia Abaqus, 2014a).

We test two cases of Martian internal structure in the finite element model displayed in Figure 2.18. We define lithosphere as follows: The lithosphere is a fully elastic layer in the Martian internal structure, denoted at T_e. Case I has a thin lithosphere of 35 km and large mantle of 1524.5 km. The use of a thin elastic layer in this study is based on results from Grott and Breuer (2008) who estimated T_e for the Hesperian epoch on Mars and found an average of 30±7 km. For Case II a thick lithosphere of 500 km is chosen, in line with the new discoveries from the InSight mission (Khan et al., 2021). Both model cases have a mantle viscosity of 10^{21} Pa · s (Plesa et al. (2018) and Khan et al. (2021)) and the core radius is kept at 1830 km as proposed by Stähler et al. (2021). As GIA is less sensitive to deeper viscosities due to the short wavelength of the ice load on the surface, pressure changes are expected to be predominantly noticeable in the first mantle layer (M1).

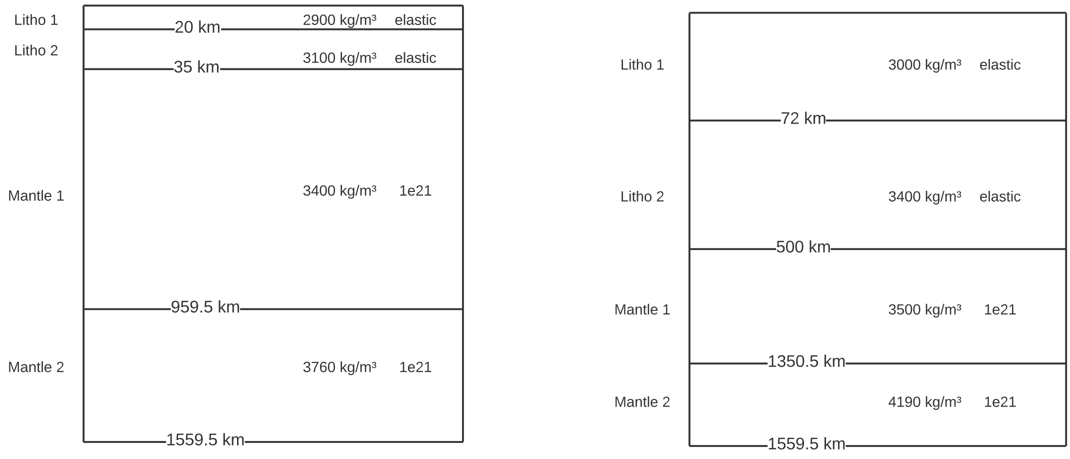

(a) (b)

Figure 2.18: Martian internal structure cases with an elastic lithosphere layer of (a) 35 km and (b) 500 km and a mantle viscosity of 10^{21} Pa·s. Density in kg/m^3 per layer is shown in the figures.

Although, lateral variations in the elastic lithosphere thickness have been mapped globally by Audet (2014) and Thor (2016), the region analysed in this study is small compared to the whole of the planet and the resolution from previous studies is not high enough to provide accurate variations for the Sisyphi Montes area. Therefore, a homogeneous lithosphere is a valid assumption for this research.

Shear moduli for lithosphere and mantle layers are set to the following values for Litho 1, Litho 2, Mantle 1 and Mantle 2, respectively: 5x10^{12} Pa, 8x10^{12} Pa, 1.05x10^{11} Pa, 2.17x10^{11} Pa. As Abaqus requires the Young's modulus as input it is first computed with Equation (2.3), where ν is the Poisson's ratio, equal to 0.5 for the case of incompressibility and S that shear modulus per layer.

$$E = 2S(1+\nu) \tag{2.3}$$

We determine the densities per layer based on computation of gravity at the surface of each layer with Equation (2.7) derived from Newton's law. For a homogeneous sphere it holds:

$$g = \frac{GM}{R^2} \tag{2.4}$$

$$M = \frac{4}{3}\pi R^3 \rho \tag{2.5}$$

G is the gravitational constant, equal to 6.67408e^{-11} m^3/kgs^2, M is the mass of the sphere, R the radius of the sphere, ρ the density of the sphere and g the gravitational acceleration. To obtain the gravity at a certain layer inside the sphere we need to take the difference in cubed radii between the layer of interest and the core which leads to the total mass of the core and the added layer.

$$M_{total} = M_{core} + \frac{4}{3}\pi(R^3_{layer} - R^3_{core}) \tag{2.6}$$

Combining Equation (2.4), Equation (2.5) and Equation (2.6) the gravity at the surface of each layer is computed with:

$$g_i = \frac{\frac{4}{3}G\pi(R_0^3\rho_0 + \sum_{j=0}^{i-1}(R^3_{j+1} - R^3_j)\rho_{j+1})}{R_i^2} \tag{2.7}$$

By varying the density of the lithosphere and mantle layers (Litho 1, Litho 2, Mantle 1 and Mantle 2) a surface gravity of 3.7119 m/s^2 for Case I and 3.7116 m/s^2 for Case II is achieved, resulting in the densities for the separate layers shown in Figure 2.18.

To analyse the rebound effect from the palaeo ice sheet in the region of interest we model Mars using a linear Maxwell rheology. The rheology of the planet behaves like a spring-damper system (spring = elasticity, damper = viscosity). Each layer in our two cases of the Martian structure is modelled as a spring-damper system, resulting in a series of smaller systems for the whole planet (Whitehouse et al., 2021).

The Finite Element model geometry is set based on the size of the ice load applied on top. The total model width is set to 3000 km. We apply a set of boundary conditions that limit the sides of the model to vertical motion only and fix the bottom, restraining any horizontal or vertical motion. Fixed boundaries may impact the magnitude, as well as the direction of the stresses in the elements at the model edges. This, in turn, may cause faulty estimations of the pressure changes as they are stress dependent (Section 2.2.6). Analysis by Qin (2021) showed that with a FE model size of 1.25 times the region of interest (ROI) boundary effects due to a finite model can be avoided.

With a circular load size of 1200 km in diameter a model width of 1500 km would be sufficient according to Qin (2021). Since we apply a fine and a coarse region in our model, we need to be sure that the fine region is not affected by boundary effects. Hence, we set the width of the fine region to 1500 km and increase the model width to twice this value. For the fine region a resolution of 30 km is set. The vertical resolution of each layer is set to 16, proving sufficient to investigate the pressure stress in the mantle. Figure 2.19 shows the model geometry and resolutions on the surface.

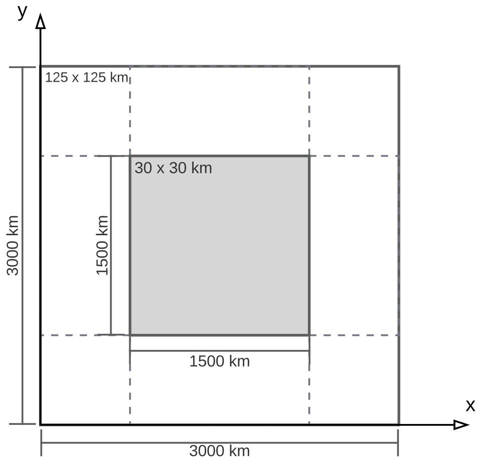

Figure 2.19: FE model geometry and resolution.

Besides the boundary conditions mentioned above, we also need constraints at layer boundaries. Density gradients in the planet's stratigraphy cause buoyancy forces to act which drive the process of isostasy. We model these restoring forces as Winkler foundations (Wu, 2004) that are applied at all internal boundaries where a density change occurs.

The element type selected is C3D8H which is a continuum, 3D, 8 node hybrid hexahedron element. As incompressibility is applied, the hybrid mesh element is a must. Advantage of using hexahedron elements in the incompressible model is that volumetric locking is avoided. If locking occurs the element would act stiffer than it actually is, leading to an underestimation of the stresses (Simulia Abaqus, 2014a). We tested the option of reduced integration to decrease simulation time. However, no major improvements could be achieved. Therefore, reduced integration was omitted.

2.2.5. Ice Load Application

For the loading scenario, the ice load is applied instantaneous as a step function (Figure 2.20a) and stays constant over the course of 2 Myr. Unloading is done with a ramp function, where the load decreases linearly over time (Figure 2.20b). We test three different unloading periods: 60 kyr, 30 kyr and 1 kyr (Section 2.2.2). It is expected that an ice melt of 1 kyr shows the largest decompression rate inside the mantle.

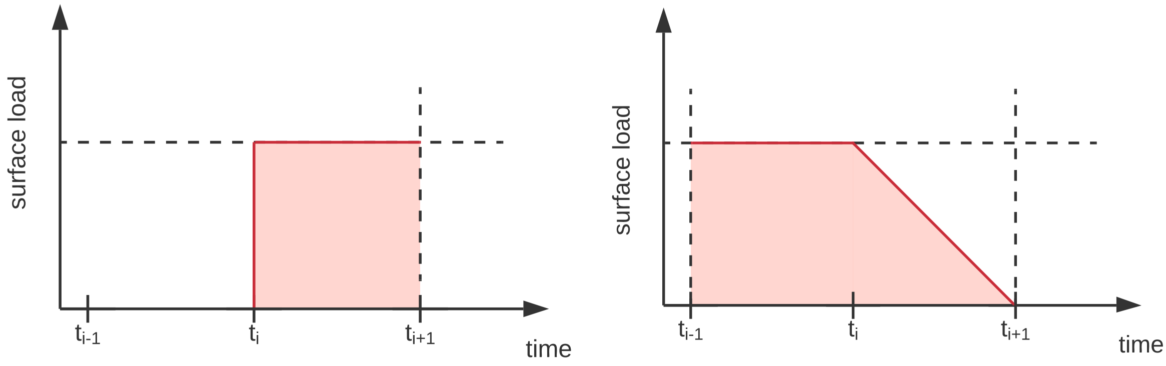

(a) (b)

Figure 2.20: Schematic drawings of (a) the instant load application at time step t_i that stays constant over time and (b) a linearly decreasing load starting at time step t_i by means of a ramp function.

We apply the ice load as a pressure load to the FE model surface. A *MappedField* object (Simulia Abaqus, 2014b) is created which uses the ice heights and maps them onto an xy-grid of the model surface as a cloud of points. This rectangular grid is then applied to the FE model surface as a pressure load where the ice height per grid cell is converted to pressure with Equation (2.8) and Equation (2.9), where ρ_i is the density of ice equal to 931 kg/m^4, h_g is the ice thickness at each cell, A is the area of a grid cell and g the gravity at the surface.

$$m_g = \rho_i A h_g \tag{2.8}$$

$$P = \frac{m_g g}{A} \tag{2.9}$$

2.2.6. Estimation of Pressure Changes

To say anything about the induced mantle melting by deglaciation, the decompression rate in the Martian mantle needs to be known. We use the previously described flat finite element model (Section 2.2.4) loaded by the reconstructed ice sheet (Section 2.2.3) to receive the pressure stresses in the mantle layer during unloading.

For engineering applications commercial FE-packages are designed to solve the stiffness equation, equivalent to the equation of motion, and given in Equation (2.10)

$$\vec{\nabla}\bar{\tau} = 0 \tag{2.10}$$

However, this relation only holds for geophysical problems where the elastic deformations have short wavelength , since self-gravitation and restoring force of isostasy are neglected (Wu, 2004). Therefore, analysis of long wavelength deformations requires modifications.

For an incompressible, non-self-gravitating flat Earth model the equations of motion are defined by Wu (2004) as:

$$\vec{\nabla}\bar{\tau} - \rho_0 g_0 \vec{\nabla}\omega = 0 \tag{2.11}$$

where $\omega = \vec{u}\hat{z}$ is the vertical component of the displacement vector (defined positive upwards), ρ_0 is the density of the layer and g_0 the gravitational acceleration in the layer.

By defining a new stress tensor (Wu and Peltier, 1982):

$$\bar{t} = \bar{\tau} - \rho_0 g_0 \omega \bar{I}, \tag{2.12}$$

Equation (2.11) can be recast into the same form as Equation (2.10).

For the analysis of results from Abaqus, the stress tensor needs to be transformed back to the elastic stress with Equation (2.13)

$$\bar{\tau} = \bar{t} + \rho_0 g_0 u_z, \tag{2.13}$$

with

$$\bar{t} = \begin{bmatrix} \sigma_x & \tau_{xy} & \tau_{xz} \\ \tau_{yx} & \sigma_y & \tau_{yz} \\ \tau_{zx} & \tau_{zy} & \sigma_z \end{bmatrix} \tag{2.14}$$

The equivalent pressure relates to stress as in Equation (2.15) (Simulia Abaqus, 2014a), where σ_{ii} is the sum of the normal stresses, the elements on the main diagonal of the stress tensor $\bar{t}$ (Irgens, 2008). Applying the stress transformation explained by Wu (2004) the final pressure in the mantle is computed with Equation (2.16).

$$p = -\frac{1}{3}\sigma_{ii} \tag{2.15}$$

$$P = -\frac{1}{3}(\sigma_{ii} + \rho_0 g_0 u_z) \tag{2.16}$$

By definition, compressional stresses are negative and tensional stresses are positive. In the case σ_{ii} is in compression the resulting pressure is positive. This is what we expect in the upper lithosphere during the loading scenario right below the loading centre. In the lower lithosphere, we expect tensional stresses to occur right below the loading centre and negative pressure to be present. Figure 2.21a and Figure 2.21b show an example of pressure in the upper and lower lithosphere for the loading of the Martian surface with an elastic lithosphere of 35 km and 500 km, respectively. These results confirm the expectations of compressional stress state in the upper lithosphere and expansion state in the lower lithosphere right below the loading centre.

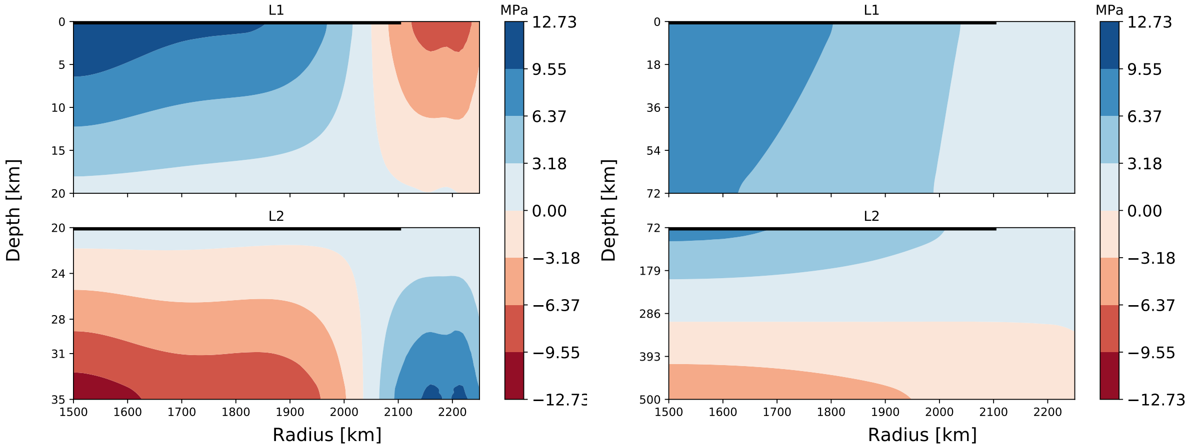

(a) (b)

Figure 2.21: Pressure (MPa) over depth and radius in the upper (L1) and lower lithosphere (L2) at t = 2 Myr of loading. Pressure is shown for the two FE model cases with an elastic lithosphere thickness of (a) 35 km and (b) 500 km. Cross-section taken at Y = 1500 km. The black horizontal line shows the region of the ice sheet on the surface with the ice divide at (1500, 1500) km in the coordinate system of the FE model.

We expect the Martian mantle to show positive pressure values at the end of the loading period, as material is flowing away from the loading centre and the region is in a compressional state. This expectation is confirmed by the pressure values in the two mantle layers as seen inFigure 2.22a and Figure 2.22b.

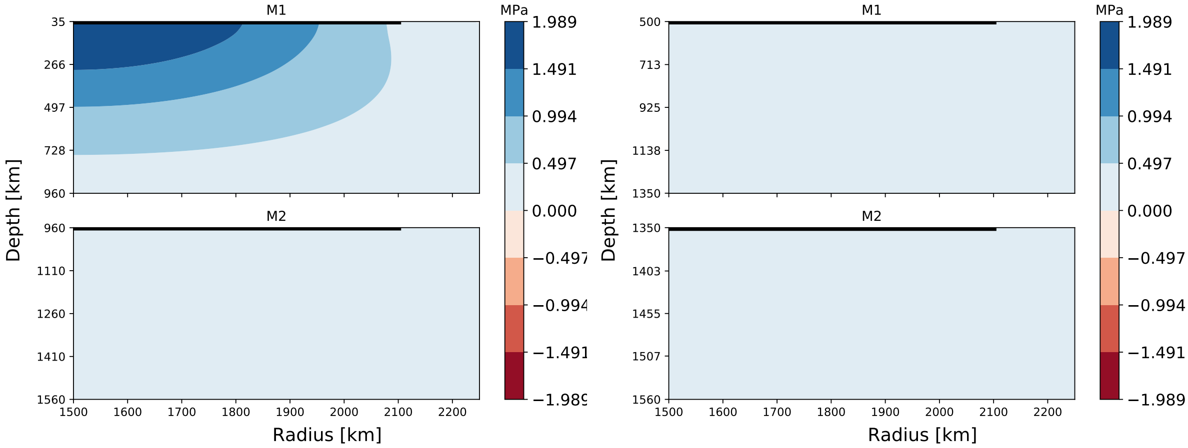

(a) (b)

Figure 2.22: Pressure (MPa) over depth and radius in the first (M1) and second mantle layer (M2) at t = 2 Myr of loading. Pressure is shown for the two FE model cases with an elastic lithosphere thickness of (a) 35 km and (b) 500 km.Cross-section taken at Y = 1500 km. The black horizontal line shows the region of the ice sheet on the surface with the ice divide at (1500, 1500) km in the coordinate system of the FE model.

In the unloading period, the ice sheet gradually decays with a linear melt. It is expected that pressure in the upper lithosphere is decreasing and becomes less positive (less compression), whereas in the lower lithosphere it is also decreasing, but becomes less negative (less tensional). Our predictions are confirmed by the model results for the lithosphere layers (Figure 2.23a and Figure 2.23b for T_e = 35 km). We find the same behaviour for the model with a thick lithosphere of 500 km (Figure 3.9 in Section 3.4.2 of the supplementary material). However, the temporal variation in P in the lower lithosphere (L2) is slightly larger than for the thin model. This implies that the tensional state in the lower lithosphere reduces quicker for a thick lithosphere.

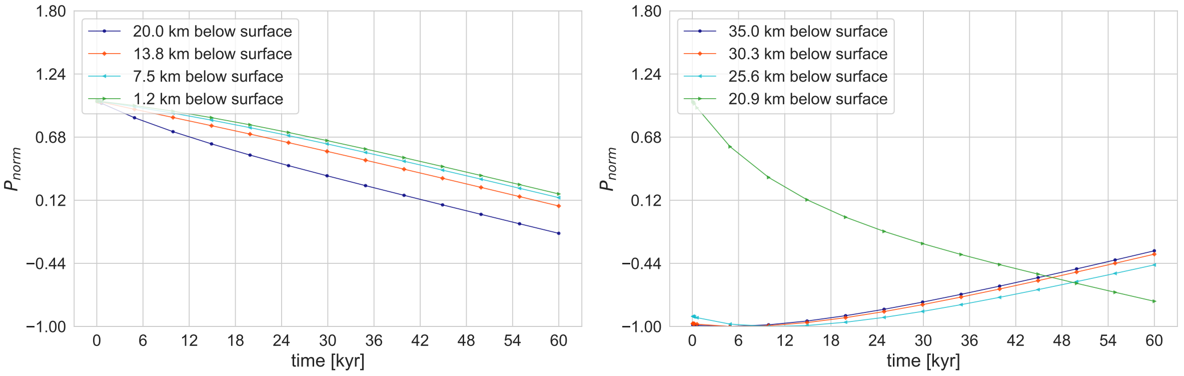

(a) (b)

Figure 2.23: Normalised pressure over time at different depths below the surface in the (a) first lithosphere layer (L1) and (b) second lithosphere layer (L2) over an unloading period of 60 kyr. Lithosphere thickness is set to T_e = 35 km. Pressure is normalised against the absolute maximum pressure at each depth. Results are obtained at X = Y = 1500 km in the coordinate system of the FE model.

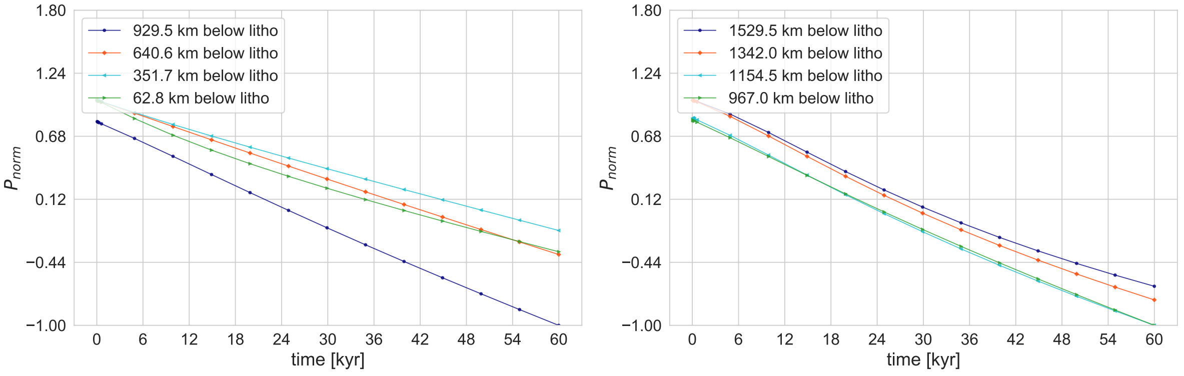

(a) (b)

Figure 2.24: Normalised pressure over time in (a) the first mantle layer (M1) and (b) the second mantle layer (M2) at different depths below the lithosphere over an unloading period of 60 kyr. Lithosphere thickness is set to T_e = 35 km. Pressure is normalised against the absolute maximum pressure at each depth. Results are obtained at X = Y = 1500 km in the coordinate system of the FE model..

In the mantle, gradual decrease of pressure is expected, letting the mantle go towards a state of expansion. Over an unloading period of 60 kyr normalised pressure over time is presented in Figure 2.24 above for a thin lithosphere. We observe almost linear decreasing pressure at all depths in the first and second mantle layer and can conclude that the FE models behave appropriately during the unloading period. For the thick lithosphere the same behaviour is observed and is shown in the supplementary material (Figure 3.10 in Section 3.4.3). We find that the change in pressure over time in both lithosphere layers varies less between the individual depths values for a thick lithosphere.

We convert these pressure values into decompression rates ($\frac{dP}{dt}$) using the (explicit) forward Euler method (Equation (2.17)). Δt is non constant, as results were extracted at selected integration time steps from Abaqus. This simplifications introduces some uncertainty in the decompression rates, but is a good approximation to estimate the order of magnitude, as we aim to find the maximum induced decompression rate (Section 2.2.6).

$$\frac{dP}{dt}(t) = \frac{P(t+\Delta t) - P(t)}{\Delta t} \tag{2.17}$$

We use these obtained decompression rates to identify magnitude and location of the maximum decompression rate possible for two different lithosphere thicknesses (35 km and 500 km) and three different unloading periods (60 kyr, 30 kyr and 1 kyr) as explained before (Section 2.2.6). The three time vectors which have been used to compute $\frac{dP}{dt}$ in the mantle over the three different unloading periods are listed in Table 2.3.

Table 2.3: Time steps at which pressure results have been extracted from Abaqus for three periods of linear unloading of the surface.

time step	60 kyr	30 kyr	1 kyr
t_0	55.5 yr	55.52 yr	50 yr
t_i	111.04 yr	111.04 yr	100 yr
t_{i+1}	166.57 yr	166.57 yr	150 yr
t_{i+2}	277.61 yr	277.61 yr	250 yr
t_{i+3}	610.75 yr	610.75 yr	500 yr
t_{i+4}	4.9 kyr	4.9 kyr	750 yr
t_{i+5}	9.9 kyr	9.9 kyr	1 kyr
t_{i+6}	14.9 kyr	14.9 kyr	-
t_{i+7}	19.9 kyr	19.9 kyr	-
t_{i+8}	24.9 kyr	24.9 kyr	-
t_{i+9}	29.9 kyr	29.99 kyr	-
t_{i+10}	34.9 kyr	-	-
t_{i+11}	39.9 kyr	-	-
t_{i+12}	44.9 kyr	-	-
t_{i+13}	49.9 kyr	-	-
t_{i+15}	54.9 kyr	-	-
t_{i+17}	59.99 kyr	-	-

2.3. Results

We are looking to find the maximum decompression rate in the shallow Martian mantle induced by unloading of a former ice sheet. From elevation of tuyas and their spatial distribution in the Dorsa Argentea Formation we have reconstructed a circular ice sheet with maximum thickness at the ice divide of 1754 m. We have use this as surface load in our incompressible, flat Mars finite element model to investigate the deglaciation effects. We have tested two different cases of internal Martian structure, one with a thin lithosphere of 35 km and one with a thick lithosphere of 500 km. Deglaciation periods have been set to 60 kyr, 30 kyr or 1 kyr and the ice linearly decays over time. We observe effects on decompression rate due to deglaciation period, as well as lithosphere thickness and compare findings to the study in Iceland.

2.3.1. Decompression Rates in the Martian Mantle

We have tested two different cases for the Martian internal structure, one with a thin lithosphere of 35 km (Figure 2.18a) and one with a thick lithosphere of 500 km (Figure 2.18b) and we have used three different deglaciation periods: 60 kyr, 30 kyr and 1 kyr. We note that largest decompression rates occur in the first layer of the mantle, therefore we do not further analyse the results in the lower mantle in detail.

We find a maximum decompression rate of 4474 Pa/yr for an unloading period of 1 kyr and a lithosphere thickness of 35 km. This maximum is present after 500 yr of ice decay and occurs directly below the lithosphere (Figure 2.25). Our results are comparable to pressure changes found in the Icelandic mantle underneath the Vatnajökull ice cap during current deglaciation (120 yr). For this region a maximum decompression rate of 1450 Pa/yr was found right below the lithosphere at 35 km (Schmidt et al., 2013).

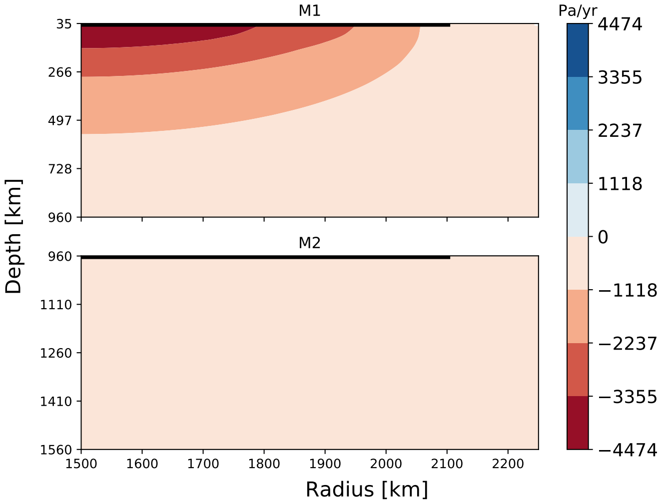

Figure 2.25: Decompression rate (Pa/yr) in the mantle layers for an unloading period of 1 kyr at t = 500 yr with T_e = 35 km Similar cross-section as in Figure 2.21.

We further find that our maximum $\frac{dP}{dt}$ is about three times larger than the one under Vatnajökull. Due to the larger surface load applied decompression rates at certain depths in the mantle are generally slightly larger on Mars than in Iceland, but as mentioned earlier comparable in magnitude. We find that the maximum decompression rate under Vatnajökull (1450 km) can be found at lower depth inside the Martian mantle as compared to right below the lithosphere in Iceland. The depth at which $\frac{dP}{dt}$ = 1450Pa/yr is about 500 km. This is an effect of viscosity being higher on Mars and more ice loss per year on Mars for the same lithosphere thickness.

Our results show that the decompression rate decreases with increasing depth underneath the decaying ice sheet (Figure 2.26). This general decrease in $\frac{dP}{dt}$ with depth is in good agreement with what is found for Iceland (Schmidt et al. (2013); Sigmundsson et al. (2010); Pagli and Sigmundsson (2008) and Jull and McKenzie (1996)). For a thin lithosphere (35 km) the maximum $\frac{dP}{dt}$ decreases by a factor of two over a depth of 295 km. While on Mars the decompression rate halves over 295 km, under Vatnajökull it reduces to $\frac{1}{8}$ of the maximum. Relatively speaking, we see a larger reduction in decompression rate for Iceland over the same depth range compared to Mars. This means, that if the maximum $\frac{dP}{dt}$ right below the lithosphere would be equal to 1450 Pa/yr, at a depth of 295 km we would find a $\frac{dP}{dt}$ of 175 Pa/yr in Iceland and a $\frac{dP}{dt}$ of 725 Pa/yr on Mars. The observation is consistent with the higher viscosity in the Martian mantle, which leads to pressure from the surface load to reach lower depth. In addition, the larger ice loss per year on Mars, results in higher values of $\frac{dP}{dt}$ at the same depth inside the mantle and the pull from the elastic lithosphere on the shallow mantle is stronger, causing decompression values right below the lithosphere to higher than at lower depths.

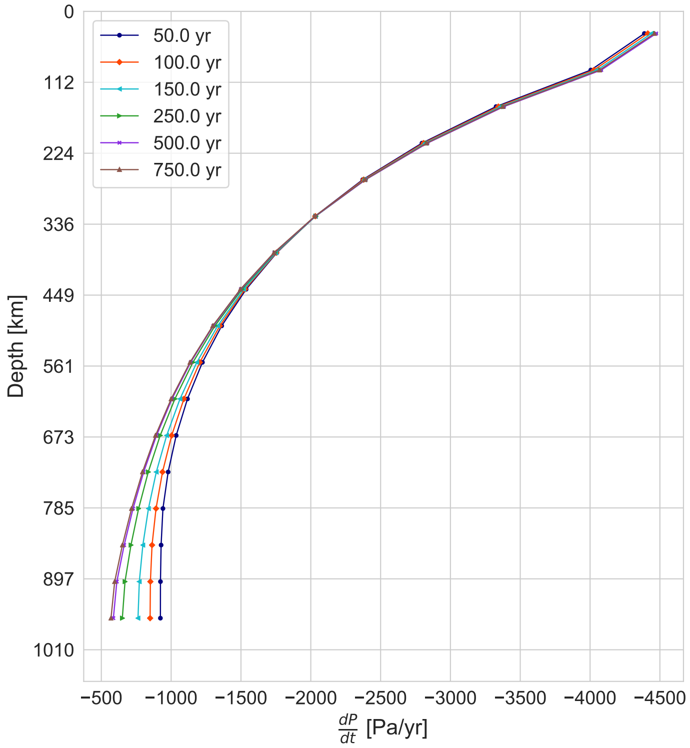

Figure 2.26: Predicted pressure changes ($\frac{dP}{dt}$) induced by deglaciation in the Martian mantle as a function of depth and time for T_e = 35 km. Pressure changes are shown right below the loading centre (X = Y = 1500 m).

Comparing the different deglaciation periods we see that maximum decompression rates for the deglaciation periods of 30 kyr and 60 kyr are 149 Pa/yr and 74.5 Pa/yr, respectively (Figure 3.7a and Figure 3.7b in Section 3.4). These maxima occur right below the lithosphere. We find a hyperbolic relationship between deglaciation period and decompression rate, where for shortest deglaciation, largest decompression rates take place.

We further observe that longer deglaciation of the same ice sheet results in a smaller reduction in $\frac{dP}{dt}$ w.r.t. the maximum decompression rate over the same depths interval. An almost linear relationship between deglaciation time and relative decrease in decompression rate w.r.t. the maximum can be inferred, if ice size and mantle viscosity are kept the same (Figure 3.4b and Figure 3.4c in the supplementary material in Section 3.3). With slower ice decay, less surface load is removed per year and the GIA process is overall slower. In the shallow mantle layers, the elastic lithosphere exerts a pulling force during the unloading period, which is also reason for the decompression rates to be larger right below the lithosphere. With a slower unloading this pull from the lithosphere is less strong. Since deeper layers of the mantle are not really affected by the lithosphere pull, the difference in $\frac{dP}{dt}$ between shallow mantle and deeper mantle is smaller for longer deglaciation.

In general we find $\frac{dP}{dt}$ to be sensitive to the lithosphere thickness. Increasing the lithosphere thickness from 35 to 500 km leads to a decrease in maximum decompression rate of 78% right below the lithosphere. However, sensitivity decreases with increasing depth (Figure 3.2 in the supplementary material in Section 3.2). The overall smaller $\frac{dP}{dt}$ with a thick lithosphere are due to the fact that the thick layer acts as a low-pass filter, only transmitting longest wavelengths of the load. And increase in lithosphere thickness for the same load size eventually results in he state of no isostasy, where only bending of the upper lithosphere takes place.

Furthermore, for 1 kyr and 30 kyr of deglaciation and a thick lithosphere the decrease in $\frac{dP}{dt}$ w.r.t. the maximum decompression rate over depth is smaller compared to the thin lithosphere case (Figure 3.5 in Section 3.3 in the supplementary material). We do find, that this decrease in $\frac{dP}{dt}$ w.r.t. the maximum decompression rate over depth is however the same for all three deglaciation periods for a thick lithosphere model. The pull on the upper mantle from the lithosphere during unloading does have a much smaller effect on the decompression rates. Therefore, the difference between the decompression rates in shallow and deeper mantle do not vary between the different deglaciation periods.

In the research by Schmidt et al. (2013) they found temporal variations in $\frac{dP}{dt}$ to be most apparent right below the lithosphere and decrease with increasing depth. We make the same observations in our results for deglaciation periods of 30 kyr and 60 kyr ((Figure 2.27b and Figure 2.27c). Decompression rate varies by up to 48% over 60 kyr and by up to 40% over 30 kyr in the model with a thin lithosphere. We have normalised decompression rates against the absolute maximum $\frac{dP}{dt}$ at each depth shown in Figure 2.27. However, over a deglaciation period of 1 kyr we see that the variation in $\frac{dP}{dt}$ over time is larger in the deeper parts of the first mantle layer (up to 35% over 1 kyr at 929.5 km below the lithosphere). This observation is not directly in line with findings by Schmidt et al. (2013) under Vatnajökull, but could possibly be an effect of the higher viscosity in the Martian mantle, since we find the same observations in the model with a thick lithosphere (Figure 3.3b in Section 3.2).

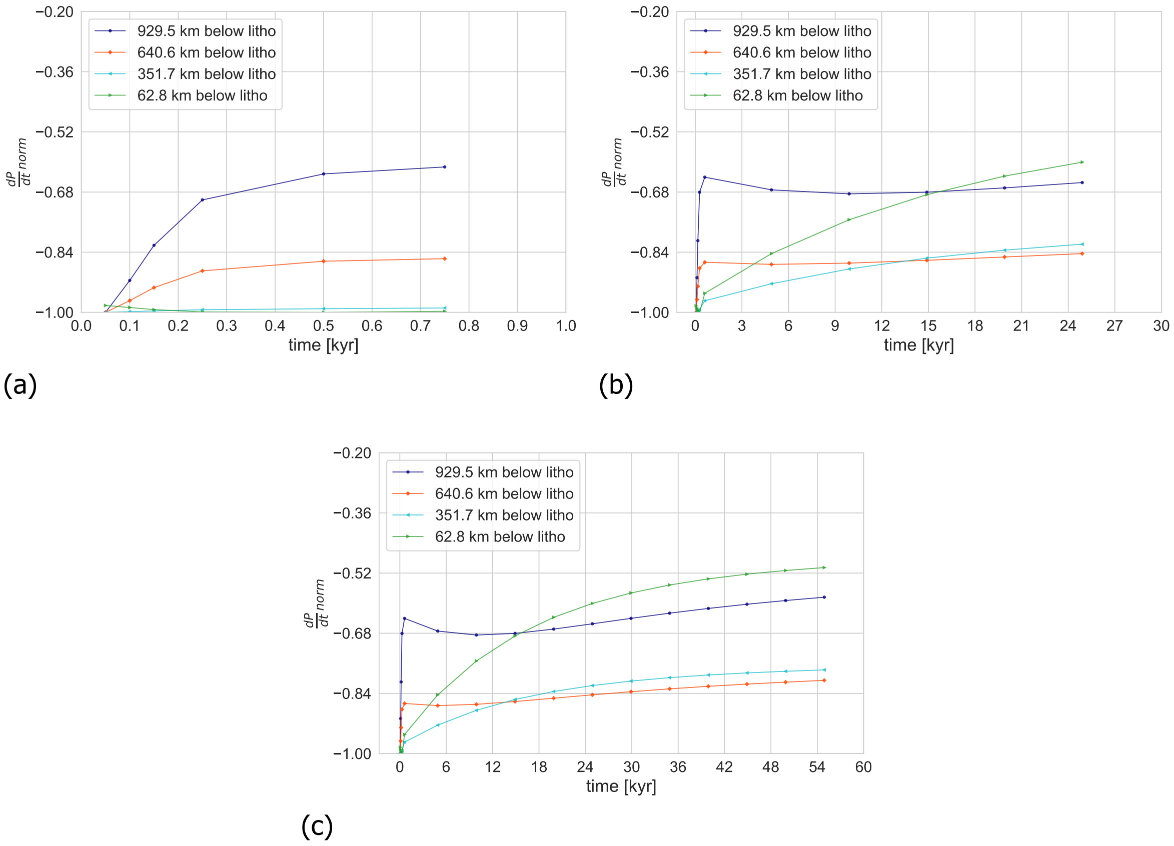

(a)

(b)

(c)

Figure 2.27: Predicted pressure changes ($\frac{dP}{dt}$) induced by deglaciation in the Martian mantle as a function of time for T_e = 35 km. Values are normalised against the absolute maximum at each depth. Results are shown for deglaciation periods of (a) 1 kyr and (b) 30 kyr and (c) 60 kyr. Pressure changes are shown right below the loading centre (X = Y = 1500 m).

We point out that for a thin lithosphere a very small increase in decompression rate at 62.8 km below the lithosphere over the first 500 yr takes place (Figure 3.8 in Section 3.4). However, this increase is small compared to the magnitude of the decompression rate itself. It means, that the decrease in pressure over time becomes slightly faster in the first 500 yr. Since we only observe this pattern for a lithosphere of 35 km, it is probably related to the thin lithosphere on top of the mantle and could possibly be an effect of hysteresis where the pressure in the mantle lags behind changes in ice loading on the surface and the upper mantle does not react immediately.

We see that in general the evolution of the decompression rates reflect the transition from an immediate elastic response at the beginning of deglaciation to a viscous response during ice melt. The immediate jump from a large decompression rate to a smaller decompression rate at the onset of deglaciation reflects the elastic response of the mantle, clearly observable for the deglaciation periods of 30 kyr and 60 kyr (Figure 2.27b and Figure 2.27c) for the model with a thin lithosphere. In GIA the elastic response of the mantle is almost immediate and we would expect this pattern to be visible for all three deglaciation periods. However, for a short deglaciation period of 1 kyr, the elastic behaviour is less apparent and could be related back to the hysteresis effect, that the mantle does not have enough time to react to the fast ice removal above a thin lithosphere.

We make similar observations for the model with a lithosphere of 500 km for all three deglaciation periods (Figure 3.6 in the supplementary material in Section 3.3). We see again that the elastic and viscous response is clearly reflected for 30 kyr and 60 kyr of ice decay (Figure 3.6b and Figure 3.6c in the supplementary material in Section 3.3). For these two deglaciation periods, the largest temporal variations in $\frac{dP}{dt}$ occur right below the lithosphere. We also find over a deglaciation of 1 kyr that the larger temporal variation in $\frac{dP}{dt}$ occurs at lower depth (Figure 3.6a in the supplementary material in Section 3.3), which could again be related to the higher viscosity on Mars. Compared to the model with a thin lithosphere this temporal variation of $\frac{dP}{dt}$ at lower depth is very similar (35% for the thin model vs. 32% for the thick model).

However, we note that the variations in decompression rate over longer deglaciation times are stronger with a thick lithosphere. Largest temporal variation of 65% is found right below the lithosphere over a deglaciation period of 30 kyr. This is about 25% more variation than for the model with a thin lithosphere. Our results give the impression that for deglaciation of 30 kyr and 60 kyr, a new equilibrium state has been reached again in the the entire mantle, whereas underneath the thin lithosphere the upper parts of the mantle still show a decrease in decompression rate over time and have not reached equilibrium yet. From this, the effect of the lithosphere thickness can be seen again which results in less unloading effects in the mantle and equilibrium can be reached faster.

2.4. Discussion and Model Limitations

Using the geological and geomorphological evidence, high resolution images and a global topography map it was possible to complete the first ever regional reconstruction of a palaeo ice sheet thickness in the South Polar Region on Mars. We have used elevation and distribution of tuyas in the Dorsa Argentea Formation to reconstruct the ice sheet with an optimised fitting approach, assuming a perfectly plastic ice sheet. We make a simplification by superimposing the tuyas onto two straight lines, one from North to South and one from East to West. This makes our ice sheet reconstruction a 2D approach, leading to some uncertainty in the surface pressure load applied to the FE model. However, since in this study we aimed to find the maximum decompression rate induced by the decaying ice sheet a 3D reconstruction would not change the decompression results, but only have a possible influence on the location of maximum decompression rate laterally.

Research by Head and Pratt (2001) and Head et al. (2007) suggested that the region could have been covered by a much larger ice sheet which was an extension of the current South Polar ice cap. This would however only alter the size of the modelled ice load and not its thickness. An increase in ice extent would cause a larger area to be affected by the pressure decrease in the mantle and possibly more wide spread mantle melting. There are two possible scenarios: (1) As there are no clear remnants of tuyas closer to the South Pole, it is less likely that the ancient ice sheet was an extension from the South Pole and that volcanic activity took place more southwards and (2) the palaeo ice sheet used to be an extension of the current South Polar cap, but volcanic activity was more localized to the area where we find tuyas today.

In our ice sheet reconstruction we assume that the knick point zone, where steep side transitions into flat top, is representative for the elevation range in which the passage zone could lie. The identified knick point zone per tuya includes the lava cap rock of the tuya. However, from the four stage tuya formation the passage zone always lies below the lava cap. Our passage zone elevations are therefore slightly overestimated and derived ice sheet thickness would have probably been lower. However, since passage zones provide an indication of the minimum ice sheet thickness, the palaeo ice sheet over the region could have been thicker in any way. This makes our results still highly likely.

Another uncertainty that is involved in the ice sheet reconstruction is the assumption made that all the nine tuyas formed during the same eruption period and are therefore of similar age. In the case they did form in different periods the ice sheet thickness would be slightly different. We would then derive the thickness only based on the passage zone elevation estimates of tuyas of similar age. In general crater counting is used to determine the age of planetary surfaces (Hartmann, 2005). However, at the current stage of available data on Mars, this approach is not possible for edifices such as the tuyas in the Dorsa Argentea Formation, as surface areas are insufficient (Martínez-Alonso et al., 2011). One could request a set of high resolution images from the High Resolution Imaging Science Experiment (HiRISE) on the Mars Reconnaissance Orbiter (MRO) of each tuya. These could be used in a potential study involving crater counting to determine the age of the tuyas.

Furthermore, the assumption of a perfectly plastic ice profile with horizontally flat bedrock does not take into account the topography. As the region surrounding the tuyas in the region of interest is relatively even, without topographic heights, only the tuyas themselves would cause a decrease in ice mass on the surface during formation. Taking this into account would result into a reduction in ice volume of 4947 km^3, which is <0.5% of the total ice volume. Volume estimates of the tuyas are taken from Ghatan and Head (2002). This would not cause any drastic changes in surface pressure load and is therefore negligible.

We used the reconstructed ice sheet to constrain the surface load over the mountain region to predict decompression rates in the Martian mantle using a finite element model. We compared our findings to Icelandic decompression rates and found that maximum decompression rates are in the same order as induced by deglaciation of Vatnajökull between 1890 and 2010. A maximum of 4474 Pa/yr was found for a GIA model with an elastic lithosphere thickness of 35 km which could be representative for ancient Mars during the Hesperian epoch (Grott and Breuer, 2008). We also tested a model using a thick elastic lithosphere which is a better approximation for Mars today (Khan et al., 2021). We observe smaller decompression rates in the Martian mantle underneath a thick lithosphere, with a maximum of 1210 Pa/yr right below the lithosphere and decreasing with depth (details can be found in the supplementary material in Section 3.2). Hence, deglaciation on Mars today would cause small effects inside the mantle regarding decompression rates.

Largest uncertainty in the FE model is the ice load history, since climate models for Mars are not as advanced yet. We have used modelled Martian obliquity cycles to make a prediction of deglaciation periods on Mars. Periods of 30 and 60 kyr are derived from the obliquity cycles, whereas a period of 1 kyr is tested as an extreme case. The shortest deglaciation period is however the same as found for a similar sized ice sheet on Earth and therefore an interesting one to be tested. When climate models for Mars have advanced further, more accurate prediction of the ice melt over time and with this better estimates of the decompression rate inside the mantle could be made. First estimates of the effect of solar brightening and radiative active clouds on ice stability in higher latitudes have already been made (Madeleine et al. (2014) and Mansfield et al. (2018)), but are not yet good enough for accurate ice models.

However, decompression rates alone do not generate mantle melt. As explained in Section 2.1.1 the melting temperature of the mantle material drops due to the change in pressure and only if it drops below the actual mantle temperature, melting takes place. Decompression rates during deglaciation in Iceland and resulting temperature changes are very small (<10th of a degree). We do not expect them to be larger on Mars. Therefore, the mantle temperature must already be very close to the melting one before the change in in situ pressure occurs. Only then any melting in the Martian mantle can take place (P. Schmidt, personal communication, October 5, 2021).

We find that the same decompression rate as in Iceland is present at lower depth on Mars. As mentioned in Section 2.3.1 the maximum decompression rate of 1450 Pa/yr under

Vatnajökull right below the lithosphere occurs at about 500 km depth on Mars.

Ding et al. (2020) provided estimates of solidus and melt productivity of an anhydrous Martian mantle. They found a depth of initial melt around 490 km for a mantle potential temperature equal to 1450°C and a mantle composition derived by Lodders and Fegley (1997). We can assume, that at a depth of 500 km the mantle potential temperature is around 1500°C, as temperature increases with depth.

We note that the depth of melt generation found by Ding et al. (2020) holds for an anhydrous Martian mantle. Water content however affects the depth of initial melt as shown in Iceland (Schmidt et al., 2013). A decrease in mantle potential temperature from 1500 to 1450°C shifted the melt depth 20 km and 40 km upwards for a dry and a wet model, respectively.

Given the estimates by Ding et al. (2020) and the fact that for a decrease in mantle potential temperature the melting depth moves upwards two scenarios could take place, that favour the melting of mantle material on Mars. (1) At a mantle potential temperature of 1500°C at a depth of 500 km, the decompression rate found in our results causes a drop in solidus temperature large enough to initiate melt. (2) An increase in water content for a mantle potential temperature of 1450°C would result in a downward shift of the melt depth that was found by Ding et al. (2020) to possibly 500 km. For scenario (1), the drop in solidus temperature by less than 10^{th} of a degree, as it occurs in Iceland, is likely large enough at the depth of 500 km. Since melt initiation at 490 km was found for a mantle temperature of 1450°C, probability is high that solidus and mantle temperature 10 km deeper are very close, and the shift in melting temperature sufficient.

With mantle melting possibly taking place deeper inside the Martian mantle as compared to Iceland, the question arises how long the magma needs to rise to the surface. Fast magma ascent could result in eruptions under the ice, forming observed tuyas in the South Polar Region. In the study by Jull and McKenzie (1996) they proposed that melt would reach the surface within 1 kyr. In another study by Maclennan et al. (2002) a maximum average melt extraction velocity of 100 m/yr matched observations for enhanced volcanism in Iceland. From our discussion above, melt could possibly generate at a depth of 500 km in the Martian mantle. With an extraction velocity similar to that in Iceland, melt would reach the surface in 5 kyr. Larger extraction velocities are possible, but unlikely for Iceland. Nevertheless, due to lower gravity on Mars, the extraction velocity is probably larger Wilson and Head (1994). Taking a velocity of 1000 m/yr, which was also tested for Iceland, results in a time lag of 500 years until melt reaches the surface. This is a likely scenario that could have taken place on Mars in the past and would ensure that volcanic eruptions still take place under the ice, for a deglaciation period of 1 kyr.

Our modelled ice sheet on Mars is comparable in size and volume to the glaciation of Iceland during the last glacial maximum (10 kyr ago). In addition, a deglaciation period of 1 kyr is equal to the deglaciation of the 2 km thick ice sheet Jull and McKenzie (1996) modelled in their study. However, for a similar surface load and unloading period we find smaller decompression rates inside the Martian mantle (4.5 kPa/yr vs. 19 kPa/yr). A reason for this could be higher mantle viscosity in Iceland and the fact that it is located over a spreading ridge. Material in the mantle is already relatively hot and mantle upwelling takes place even without a change in pressure due to unloading. An increase in Marian mantle viscosity would potentially result in larger decompression rates at more shallow depths than what we have found in this study.

In order to calculate the exact melt generation, melt parametrisation is needed. We do not model actual melting rates in this study, due to lack of knowledge about mantle composition. However, initial estimates on mantle compositions are already present from modelling (Khan and Connolly (2008); Lodders and Fegley (1997)) With a thorough study of Martian meteorites the mantle composition can most probably be further constraint. Parameters such as specific heat constant, thermal expansivity and bulk water content could possibly be derived. Furthermore, a thorough study of the SNC meteorites could provide information on the concentration of incompatible elements (uranium, thorium). This would help to determine the amount of melt generated due to deglaciation only. However, uncertainties lie within the age of the meteorite, as well as their origin location on Mars. Meteorites from the northern plain would not be representative for this study.

As mentioned in Section 2.1.1 also dyke formation and magma chamber failure in the crust are a likely process during the unloading period of an ice sheet (Mora and Tassara (2019); Sigmundsson et al. (2010); Wilson and Russell (2020)). A magma filled dyke propagates inside the Earth's lithosphere when the driving pressure exceeds the in situ tensile strength of the host rock plus the horizontal stresses induced by unloading. During unloading, the upper lithosphere is in tension and dyke propagation is favourable. The maximum crustal rock strength on Earth is about 10 MPa (Gudmundsson, 2012) and magma driving pressures lie between 3 to 30 MPa on Earth Wilson and Russell (2020). For magmas with high driving pressure, the horizontal stresses in the crust must therefore be large, between 15 to 20 MPa.

From our finite element model analysis we can see horizontal tensile stresses of up to 17 MPa in the Martian upper lithosphere. We find these stresses for the model with a thin lithosphere (35 km) and a deglaciation period of 1 kyr. Assuming similar rock and magma composition on Mars, these horizontal stresses would result in a driving pressure of 27 MPa, which is within the range of magma driving pressures found on Earth. Therefore, the process of magma chamber failure and initiation of dykes inside the Martian upper lithosphere due to deglaciation is a very likely process.

Although location of magma chambers is suggested to be deeper on Mars than on Earth Wilson and Head (1994), the lower surface gravity causes magma to rise quicker. In addition, heavily cratered surface in the South could make it more likely for fractures in the surface to occur and magma to rise upwards. We can conclude that both, mantle melting and dyke propagation, are viable processes to have occurred on Mars.

Modelling Mars using a flat, finite element model brings some uncertainties, as well. The current model size is limited to a region of interest of less than 1500 km in diameter. If the ice sheet would have been an extension of the South Polar cap, a larger FE model would be required to not run into boundary problems as discussed in Section 2.2.4. We expect decompression rates to be spread over a larger region spatially. If the thickness of the larger ice sheet would be kept the same, variations in maximum decompression rate inside the mantle will probably not occur, as thickness and unloading period influence the process in the mantle, the most. However, faster melting of the ice edges could have an influence on the decompression rates in the region of interest, in case the edge of the large ice sheet is right above the region of tuyas.

In addition, a flat model is less representative for the actual planet. In this study, the flat assumption is still applicable since the surface load size is small enough. For a surface load wavelength of more than 1200 km a spherical model is suggested based on findings from Qin (2021).

Furthermore, we only modelled linear rheology for Mars and assumed no lateral variations in viscosity. Including non-linear rheology would mean that elastic and viscous parameters in the Mars model vary with depth. However, much more precise knowledge on the Martian interior composition and structure is needed to propose such non-linear rheology models. Advances in knowledge gained from the InSight mission are promising to constrain the interior further. In addition, in the future laboratory deformation experiments could be carried out on rock samples extracted from the Martian mantle. Lateral variations of viscosity and also lower values of viscosity would favour the melt production, as the mantle would potentially be hotter and wetter.

2.5. Conclusion

In this study we have examined how deglaciation of a palaeo ice sheet over the Sisyphi Montes affects Martian mantle decompression rates and aimed to find support for the following hypothesis: *The unloading of the Martian mantle, due to melting of a former ice sheet, has contributed to forming tuyas, glaciovolcanic edifices, in the South Polar region on Mars.*

We reconstruct the minimum ice sheet thickness from tuya heights in the region of interest using slope and curvature analysis. From this, we find that an ice sheet with thickness at the ice divide of 1754 m matches the tuya heights best. The optimum location of the ice midpoint was found to be at 7°E and 63.8°S and a circular shape with radius of 600 km covered all edifices under the ice.

We apply the derived ice sheet as a pressure load to our flat finite element model to analyse glacially induces decompression rates in the Martian mantle. We model Mars as an incompressible elastic lithosphere that overlays an incompressible viscoelastic mantle. Mantle viscosity is set to 10^{21} Pa · s. An ice history based on estimated Martian obliquity cycles of the past 20 Myr has lead to testing of three different deglaciation periods: 60 kyr, 30 kyr and 1 kyr. Deglaciation of 1 kyr is investigated as we expect shorter ice melt to cause larger decompression rates inside the mantle. In addition, this deglaciation period is similar to the ice melting of a comparable ice sheet in Iceland during the last glacial maximum and results can be compared. Two different lithosphere models are tested, one with a thin layer, resembling ancient Mars and one with a thick layer, more representative of Mars today.

We find that decompression rates ($\frac{dP}{dt}$) induces by deglaciation vary in space and time with a general decrease with increasing depth. Peak decompression rates of 4474 Pa/yr are found for the shortest unloading period of 1 kyr right below the elastic lithosphere of 35 km.

This maximum decompression rate is slightly larger, but comparable to values found during the present-day deglaciation of Vatnajökull in Iceland, which resulted in decompression rates of up to 1450 Pa/yr. We find the same $\frac{dP}{dt}$ value at a depth of 500 km inside the Martian mantle. The solidus and mantle temperature at this specific depth would need to be very close to each other in order for decompressions rates of this magnitude to cause any material melting. There is however evidence from modelling results that this could indeed be the case, favouring the initiation of melt and with it increase in eruptions. Uncertainty remains about the timing of volcanism due to the increased melt generation. However, with estimated delays in the order of 500 to 1000 yr, increase in volcanism would still occur during the presence of ice on the surface. This would favour the formation of tuyas.

If on ancient Mars similar climate conditions would have been present as in Iceland today, specifically a warm mantle and more water content, mantle melting would have been very likely. In addition, provided that magma ascent velocities are high and increase in eruption rate would have also possibly occurred. Our study proposes that the deglaciation of Vatnajökull today and induced mantle melting underneath are a good analogue study for processes related to deglaciation on Mars. Furthermore, the trapping of magma during glacial loading and magma release and propagation of dykes during unloading times is a viable process inside the Martian lithosphere. This could be an alternative hypothesis for the origin of the tuyas found in the South Polar Region.

3

Supplementary Material

The following sections serve as supporting material for the main article. Firstly, an explanation in the identification of a knick point in ArcGIS Pro is given in Section 3.3. Secondly, the effects of the lithosphere thickness are discussed in Section 3.2. After this, Section 3.3 provides explanation on how deglaciation period affects the decompression rates in the mantle. Section 3.4 shows a number of supplementary figures with short explanation.

3.1. Mountain Knick Point Analysis

Identification of knick points in river beds has been done using slope-area relations and visual inspection (Zahra et al., 2017). It is a time intensive process, but using observations and expert knowledge on the morphologies make it a robust approach. The identification of knick point regions for the tuyas on Mars has been done by combining slope and profile curvature of the Martian surface and by visually inspection. Figure 3.1 shows a flow diagram of the individual steps taken to receive slope and curvature layers in ArcGIS Pro from the MOLA raster data set and identifying possible knick points of the mountains. The steps are further explained below:

1. After importing the MOLA raster data sets, it is necessary to create a hillshade with the Hillshade raster function. This layer is a grayscale 3D representation of the surface where the relative position of the Sun is taken into account. Altitude and azimuth properties are kept at default.
2. Activating the new hillshade layer, one can zoom to mountain of interest and turn on the CTX image layer.
3. Apply *Raster Calculator* with criteria: Elevation >= 1300 m slightly over the average base elevation for all mountains to exclude the change between mountain slope to plain on the base. As an input raster dataset we selected the clipped elevation dataset of the mountains, generated previously.
4. Apply *Reclassify Spatial Analyst Tool* to reclassify the cells that match minimum elevation from step 3 to a value of 1 and a selected colour. Set cells that do not match the criteria from step 3 to 'no colour'.
5. Add *Surface Parameters 3D Analyst* to calculate the **slope** and **profile curvature** for each mountain. Ground elevation must be selected as surface input. We calculate slope in degree and select profile curvature to be able to identify convex regions. Results of the tool application are shown in Figure 2.4b, Figure 2.4a and Figure 2.5a in Section 2.2.3.
6. Based on slope and profile curvature knick point regions are identified visually, where cells of largest slope and highest profile curvature meet. A feature class is created to

create ring shaped polygons that include all identified cells. Results are presented in Figure 2.5b in Section 2.2.3.

7. To extract elevation data from the polygon feature the *Interpolate Shape* tool is used first. This tool created a 3D feature by interpolating the z values from the ground surface. The ground surface is the MOLA raster data set used as elevation surface.
8. Apply *Stack Profile* to each drawn polygon feature to extract elevation values in a table and save as .txt file.
9. Analyse elevation of knick points regions of mountain in Python.

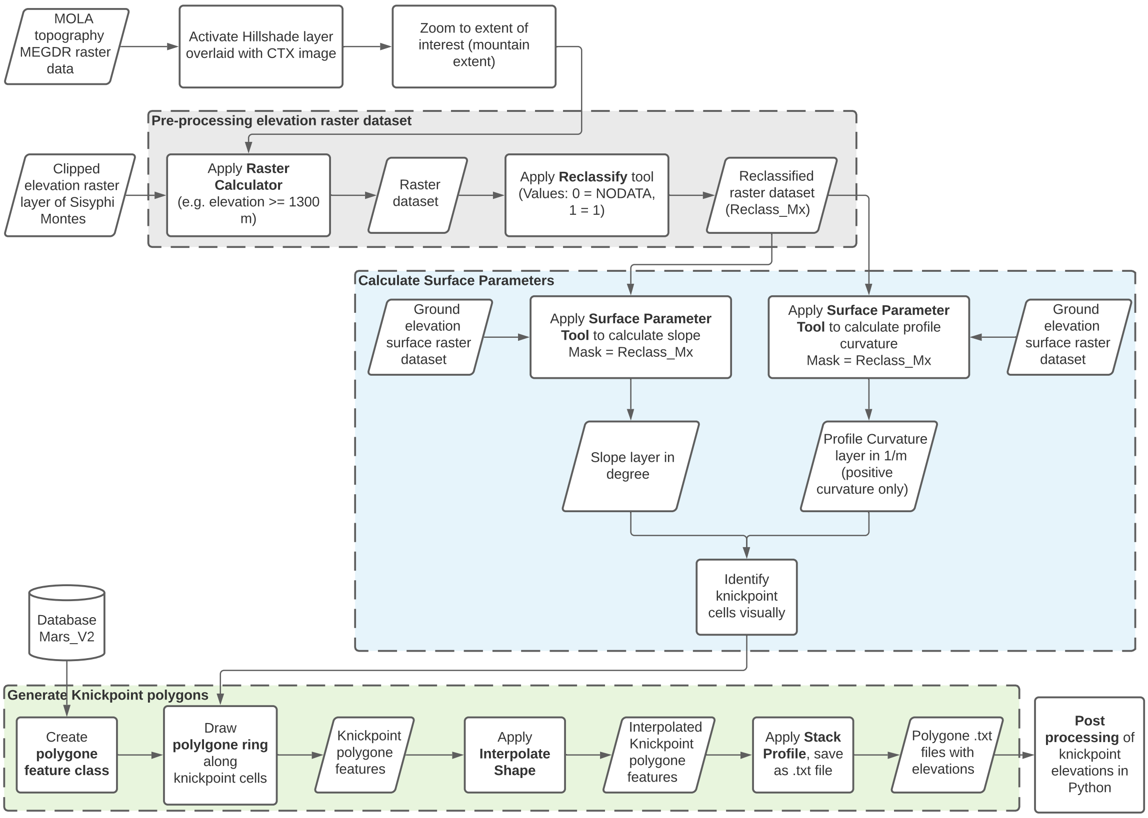

Figure 3.1: Flow diagram of the knick point analysis using slope and profile curvature in ArcGIS Pro.

3.2. Effects of Lithosphere Thickness

In this section the effect of the lithosphere thickness on decompression rates in the Martian mantle is explained.

In general, a sensitivity of decompression rate to lithosphere thickness can be observed (Figure 3.2 below). This is in line with findings in Iceland (Schmidt et al., 2013). For an increase in T_e from 35 to 500 km a decrease in decompression rate of up to 77% takes place. Sensitivity decreases with increasing depth below the lithosphere. At a depth of about 800 km below the lithosphere the decompression rates are very similar.

The large change in magnitude in decompression rate right below the lithosphere is due to the fact that the thicker the lithosphere, the less wavelengths are transmitted to the mantle regions and the load is more heavily supported by the strong elastic layer. The relation between lithosphere thickness and size of the load determines the state of isostasy. This means that with a thicker lithosphere for the same load size, isostasy may eventually not be present any more and only bending of the upper lithosphere layer takes place. Figure 3.2 shows the decompression rate in the mantle below each case of lithosphere thickness. Values are shown at 500 yr after onset of deglaciation as this is where the maximum decompression for the thin lithosphere model is observed.

Looking at the maximum decompression rates, we find a maximum of 1210 Pa/yr for the model with a thick elastic layer right at the start of unloading and over a deglaciation period of 1 kyr. For the thin model a maximum $\frac{dP}{dt}$ of 4474 Pa/yr occurs after 500 yr. The difference in temporal occurrence of the maxima can also be seen when comparing the two sub-figures in Figure 3.3. Why the maximum for the thin model is present only after 500 yr of unloading is not clear.

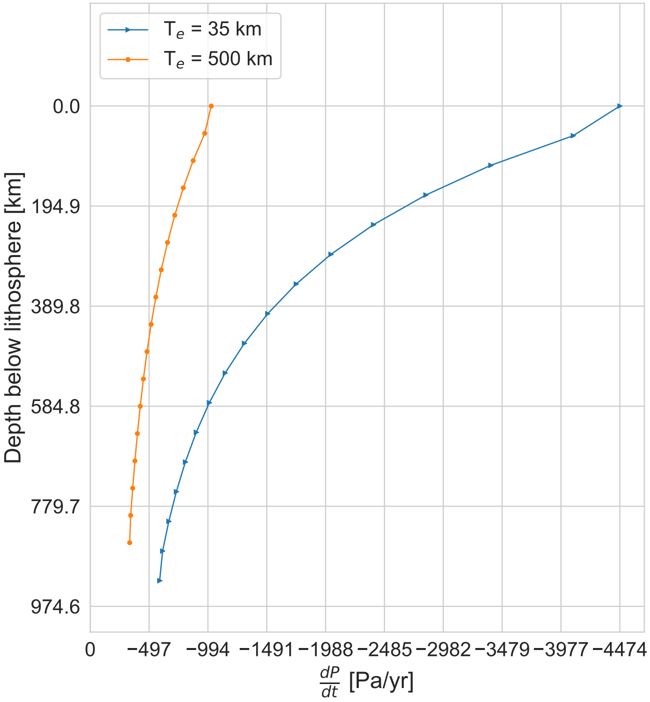

Figure 3.2: Predicted pressure changes ($\frac{dP}{dt}$) induced by deglaciation in the Martian mantle as a function of depth below the lithosphere for two different elastic lithosphere thicknesses at t = 500 yr over a deglaciation period of 1 kyr. Pressure changes are shown right below the loading centre (X = Y = 1500 m).

Comparing the decompression rates over time for the two lithosphere thicknesses we find that the general behaviour is the same: A decrease in $\frac{dP}{dt}$ over time (Figure 3.3). However, we find that for the thin lithosphere case the decompression rate first increases until 500 yr and then starts to decrease (Figure 3.3a). As mentioned above, the reason for this is not entirely clear, but could be a possible hysteresis effect, where the response of the mantle lags behind the unloading. This cannot be observed for the thick lithosphere, where $\frac{dP}{dt}$ decreases directly from the onset of deglaciation onwards Figure 3.3b. Since this pattern is only present in the thin lithosphere model, it must be related to the thickness of the lithosphere.

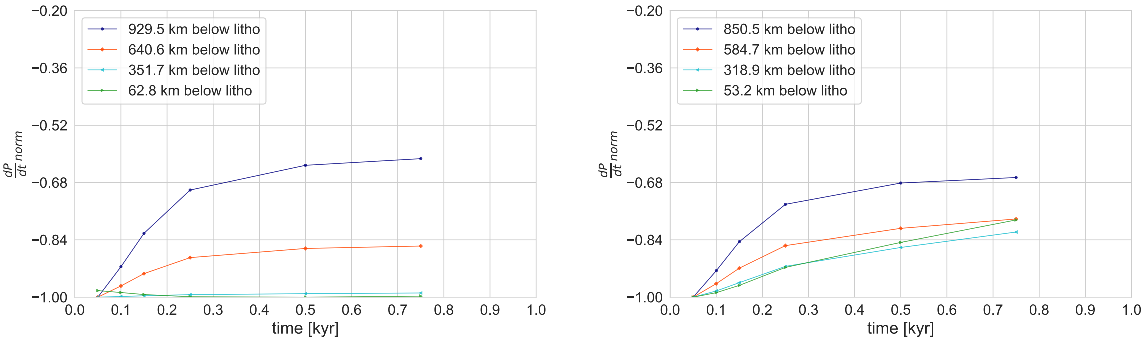

(a)

(b)

Figure 3.3: Predicted pressure changes ($\frac{dP}{dt}$) induced by deglaciation in the Martian mantle as a function of time for an elastic lithosphere thickness of (a) 35 km and (b) 500 km. Values are normalised against the absolute maximum at each depth. Pressure changes are shown right below the loading centre (X = Y = 1500 m).

From our modelling we also detect that the temporal variation in $\frac{dP}{dt}$ are more similar between different depths when we have a thick lithosphere overlaying the mantle (Figure 3.3). The thick lithosphere acts as a low-pass filter and only transmits the longest wavelengths of the load. Therefore, the decompression rate right below the lithosphere is lower for the thick model and less variation over the same depth as in the thin model can be found, as $\frac{dP}{dt}$ decreases to a similar value over a similar depth interval below the lithosphere.

3.3. Effects of Deglaciation History

Here we discuss the effects of deglaciation periods on decompression rates more in depth.

We find that the overall behaviour of $\frac{dP}{dt}$ as a function of depth and time is similar for all deglaciation periods, with a decreasing decompression rate with increasing depth and time (Figure 3.4a, Figure 3.4b and Figure 3.4c). For the longer deglaciation periods, doubling the period leads to a decrease in $\frac{dP}{dt}$ to half the maximum value (Figure 3.4b and Figure 3.4c). Taking the short deglaciation period into account, we find a hyperbolic relationship between deglaciation period and decompression rate. The same behaviour is found for a lithosphere thickness of 500 km (Figure 3.5).

We further take a look at the decrease in decompression rate with respect to the maximum value over depth. It can be observed that when the ice is decaying slower, the difference between $\frac{dP}{dt}$ in the shallow mantle and deeper mantle decreases. Over a depth range of 925 km and 1 kyr of deglaciation $\frac{dP}{dt}$ reduces to about 12% of the maximum. For 30 kyr of deglaciation decompression rate reduces to about 20% of the maximum value, whereas for the 60 kyr case it reduces to 40% of the maximum. Therefore, changes with respect to the maximum value over the same depth range are smaller for longer ice melt.

Furthermore, analysis shows that for all deglaciation periods decompression rate decreases over time, as also pointed out earlier (Figure 3.4). The largest variation can be observed for the longest deglaciation period, which is logical. $\frac{dP}{dt}$ varies of up to 50% over 60 kyr of unloading and we find this variation occurs right below the lithosphere (Figure 3.4c). For 30 kyr of deglaciation largest temporal variation in $\frac{dP}{dt}$ also occur right below the lithosphere. It is interesting to note that for the case of the thin lithosphere, the variations in $\frac{dP}{dt}$ over a short deglaciation periods are very small in the shallow mantle region and are larger for deeper regions (Figure 3.4a). This observation is in contradiction to to the observations in Iceland by Schmidt et al. (2013) where they found that the temporal variations in $\frac{dP}{dt}$ decrease with increasing depth. Since the larger temporal variation in decompression rate at lower depth is also found for a thick lithosphere and deglaciation of 1 kyr, it could possibly be an effect of higher viscosity used in the Mars model compared to Iceland. With the mantle being more viscous, the pressure from the surface load can travel to deeper depths.

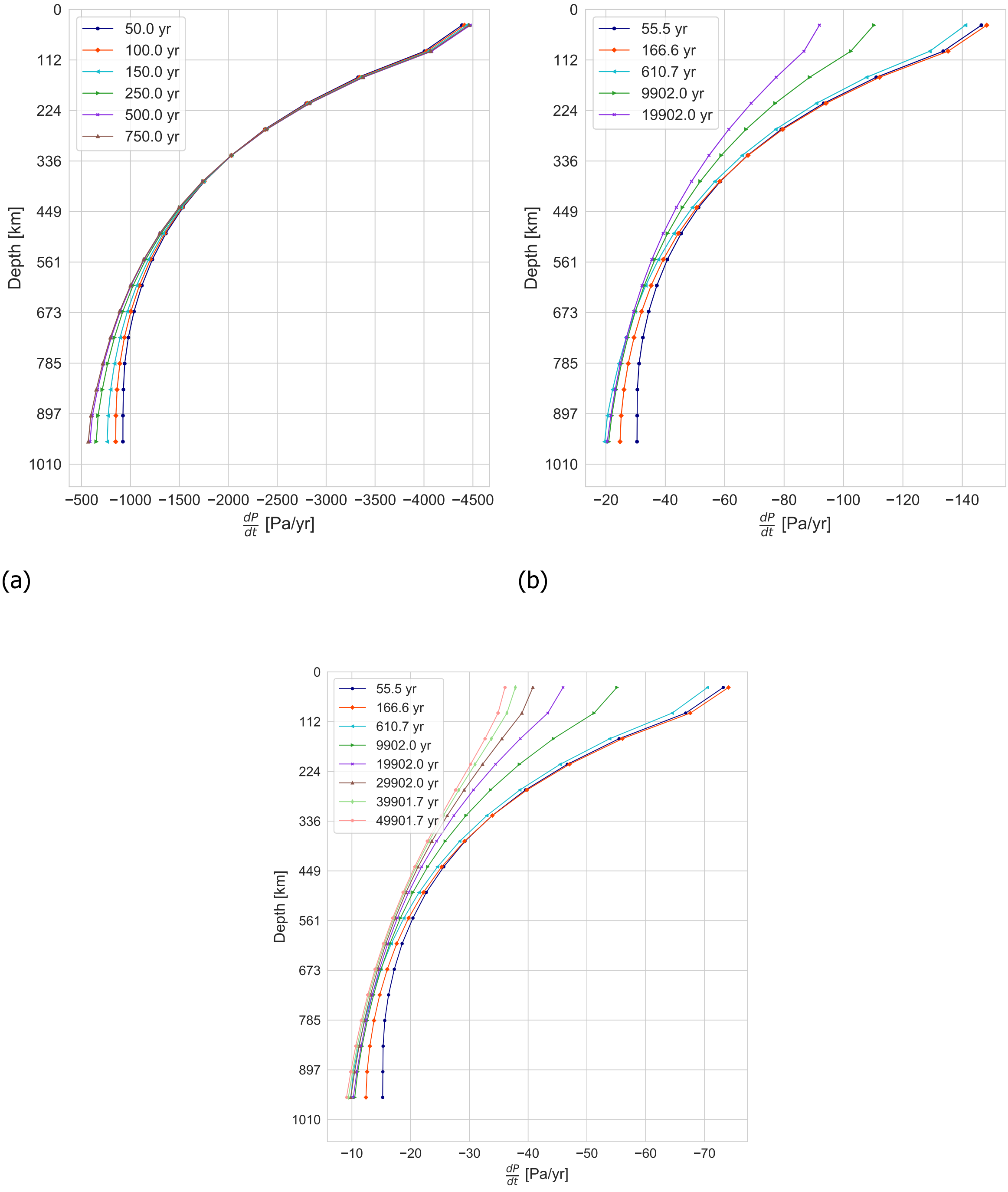

(a)

(b)

(c)

Figure 3.4: Predicted pressure changes ($\frac{dP}{dt}$) induced by deglaciation in the Martian mantle as a function of depth and time for an elastic lithosphere thickness of 35 km. Deglaciation period is set to (a) 1 kyr, (b) 30 kyr and (c) 60 kyr. Pressure changes are shown right below the loading centre (X = Y = 1500 m).

The effects of deglaciation history already mentioned are also visible for the model with a thick lithosphere (Figure 3.5). A general decrease in decompression rate for longer deglaciation and temporal variations that are largest right below the lithosphere for the deglaciation periods of 30 kyr and 60 kyr. However, there is no difference of the decrease in maximum $\frac{dP}{dt}$ over depth between the three deglaciation periods. The decompression rates decrease to 40% of the maximum value over the same depth interval (Figure 3.5).

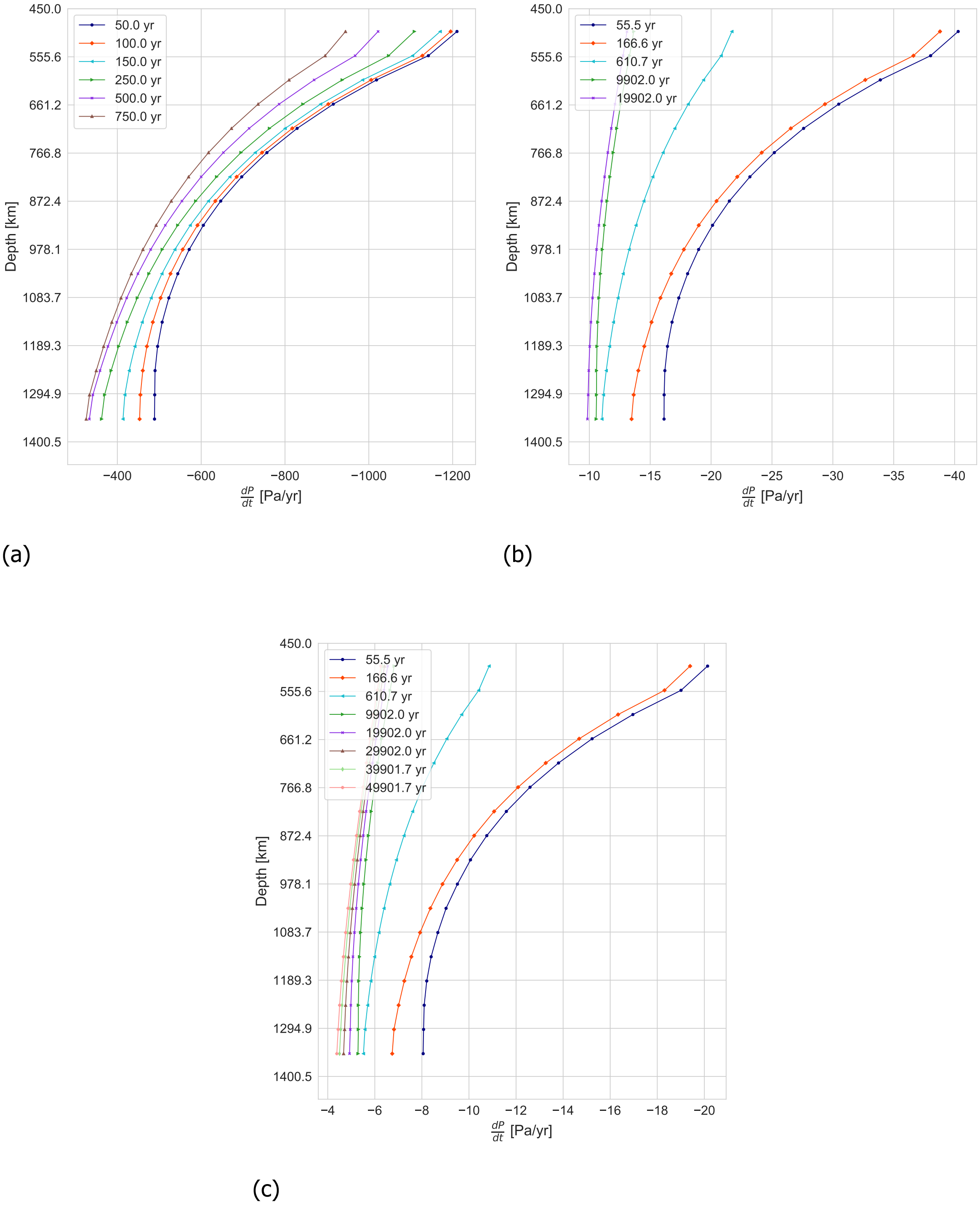

(a)

(b)

(c)

Figure 3.5: Predicted pressure changes ($\frac{dP}{dt}$) induced by deglaciation in the Martian mantle as a function of depth and time for an elastic lithosphere thickness of 500 km. Deglaciation period is set to (a) 1 kyr, (b) 30 kyr and (c) 60 kyr. Pressure changes are shown right below the loading centre (X = Y = 1500 m).

Taking a look at decompression over time for the model with a thicker lithosphere, we observe similar behaviours than for the thin lithosphere (Figure 3.6). A decrease in $\frac{dP}{dt}$ over time takes place and largest variations of decompression over time are observed for the longest deglaciation period (60 kyr). Longer periods of ice decay show the largest temporal variation in decompression rate in the shallow mantle, right below the lithosphere (Figure 3.5c and Figure 3.6c), whereas a short deglaciation period shows largest variations in the lower mantle regions. This particular behaviour is consistent with our results for a thin lithosphere, however in general contradiction to the Icelandic decompression rate variations that decrease with depth. That temporal variations in decompression rate over short deglaciation are more pronounced at deeper depth could be again an effect of the higher viscosity on Mars.

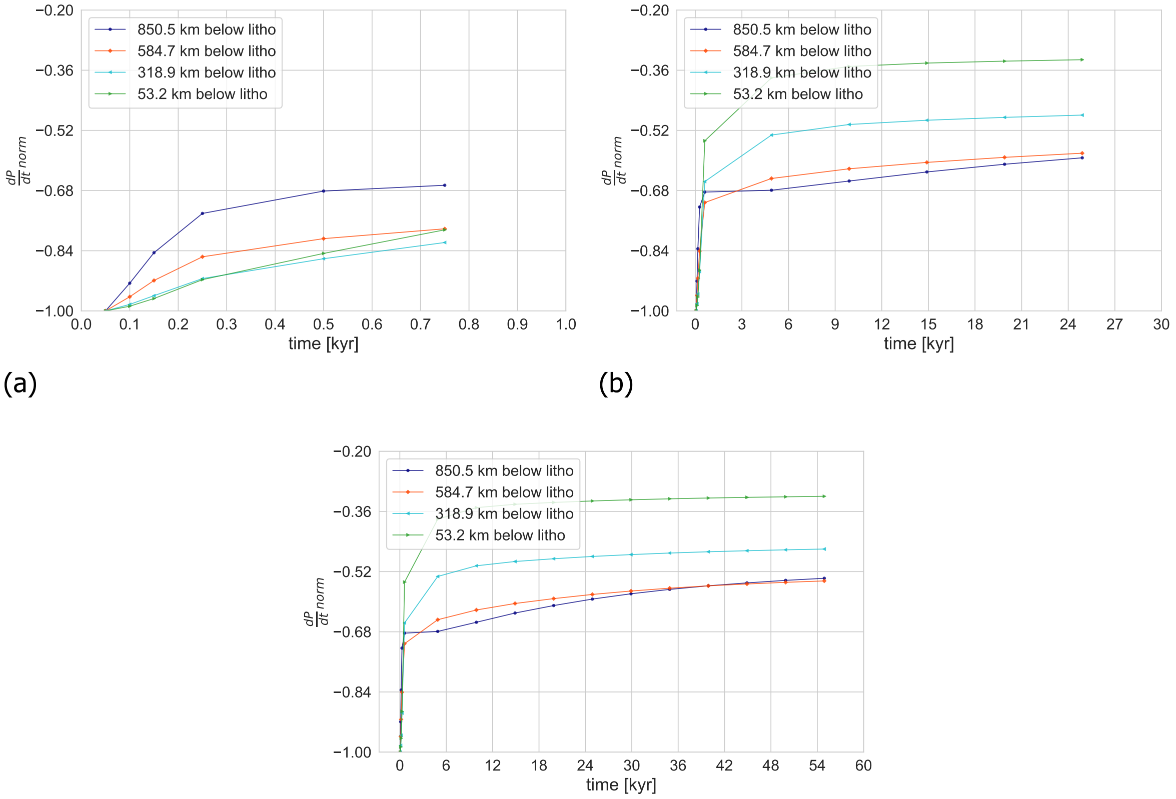

(a)

(b)

(c)

Figure 3.6: Predicted pressure changes ($\frac{dP}{dt}$) induced by deglaciation in the Martian mantle as a function of time for an elastic lithosphere thickness of 500 km. Values are normalised against the absolute maximum at each depth. Results are shown for deglaciation period of (a) 1 kyr, (b) 30 kyr and (c) 60 kyr. Pressure changes are shown right below the loading centre (X = Y = 1500 m).

3.4. Supplementary Figure

The supplementary figures serve as supporting material for the main article. In Section 3.4.1 the contour plots of maximum decompression rates for deglaciation of 30 kyr and 60 kyr for the model with a thin lithosphere are shown. And a enlarged plot of decompression rate over time for a deglaciation of 1 kyr is provided. Furthermore, Section 3.4.2 and Section 3.4.3 provide plots of normalised pressure over time in the lithosphere and mantle for a thick lithosphere model, respectively.

3.4.1. Decompression Rates in the Mantle

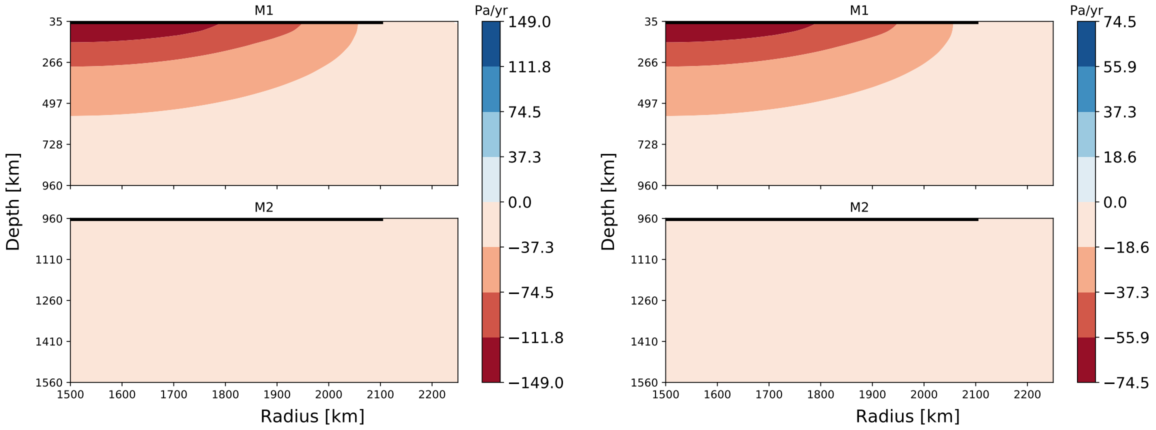

(a)

(b)

Figure 3.7: Contours of maximum predicted decompression rates ($\frac{dP}{dt}$) induced by deglaciation in the Martian mantle. $\frac{dP}{dt}$ is shown at t = 277 yr with T_e=35 km for (a) a deglaciation period of 30 kyr and (b) a deglaciation period of 60 kyr. Black horizontal lines indicate the ice sheet on the surface. Cross-section taken at X=Y=1500 km.

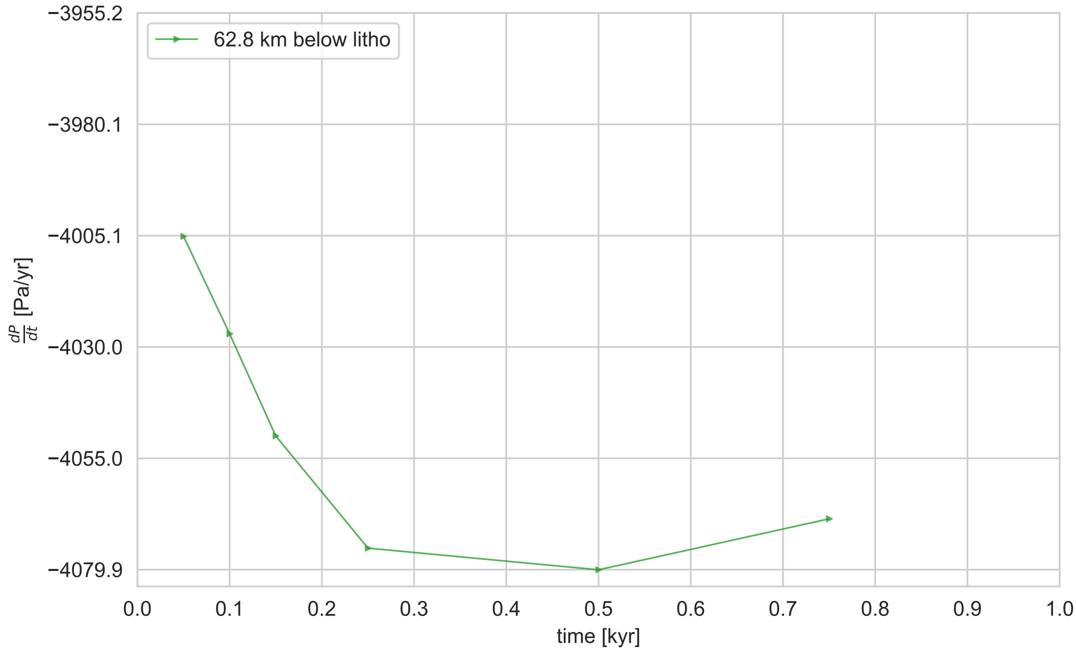

Figure 3.8: Decompression rate at 62.8 km below the Martian lithosphere with T_e=35 km over a deglaciation period of 1 kyr. $\frac{dP}{dt}$ is shown right below the loading centre (X=Y=1500 km) in the coordinate system of the FE model.

3.4.2. Pressure Changes in the Lithosphere

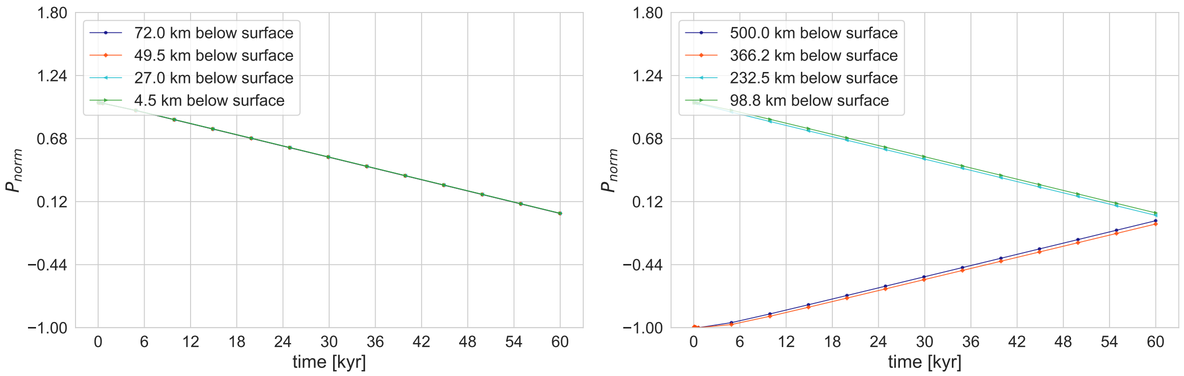

(a) (b)

Figure 3.9: Normalised pressure over time at different depths below the surface in the (a) first lithosphere layer (L1) and (b) second lithosphere layer (L2) over an unloading period of 60 kyr. Lithosphere thickness is set to T_e = 500 km. Pressure is normalised against the absolute maximum pressure at each depth. Results obtained at X = Y = 1500 km in the coordinate system of the FE model.

3.4.3. Pressure Changes in Mantle

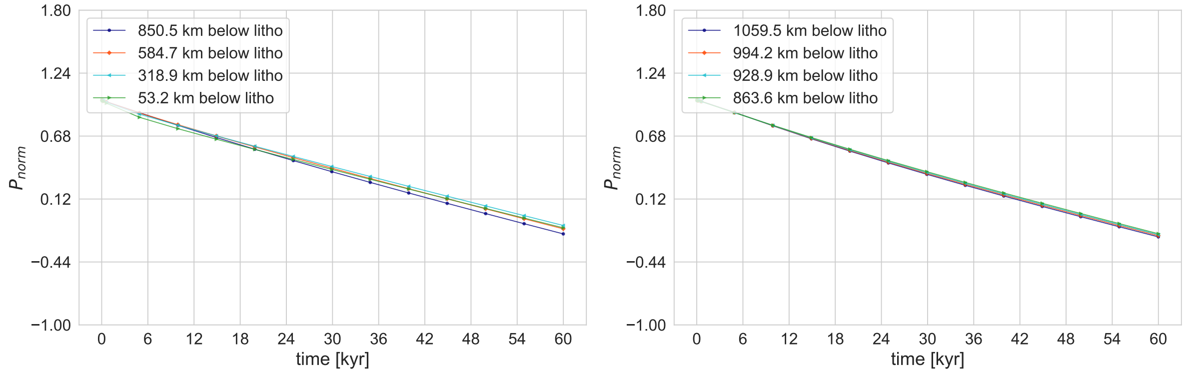

(a) (b)

Figure 3.10: Normalised pressure over time in (a) the first mantle layer (M1) and (b) the second mantle layer (M2) at different depths below the lithosphere with T_e = 500 km.Pressure is normalised against the absolute maximum pressure at each depth. Results are obtained at X = Y = 1500 km in the coordinate system of the FE model.

4

Conclusion and Recommendations

In the two sections below the overall conclusions from the results are presented and the research questions are answered. After this a statement on the research hypothesis is given. Lastly, a number of recommendations are mentioned for future work inSection 4.2.

4.1. Conclusion

Firstly, the sub-questions are answered, after which the main hypothesis is discussed.

a) *How can the elevation and spatial distribution of tuyas in the Dorsa Argentea Formation be used to constrain the minimum palaeo ice sheet thickness and minimum ice extent?*

In this study the first ever regional reconstruction of a palaeo ice sheet was done using tuya heights in the South Polar Region on Mars. Ice sheet reconstruction from tuya height done on Earth helps to gain knowledge about past climate and processes inside the Earth. An optimised fitting approach was applied with the goal to find the optimum ice divide height (H_0) above the base elevation and optimum location (Δx) of the ice sheet with respect to the tuyas, such that for all tuyas the distance between the maximum possible passage zone elevation and the ice height is minimised.

On selected mountains in the region of interest, slope and curvature analysis have been applied to determine a knick point region, where the steep slope of the mountain transitions into a flat top. From the identified region, elevation values were extracted that served as indication for the elevation range in which the passage zone possible lies. Passage zones of tuyas on Earth are indicators for the minimum palaeo ice sheet thickness under which the volcano erupted (Smellie and Edwards, 2016) and the same relationship has been applied on Mars in this study.

Although previously identified as tuyas by Ghatan and Head (2002), a clear knick point region could not be recognised for six of the initially eighteen mountains. These were therefore excluded from the study. The other eleven were termed tuyas, since a clear knick point could be found. A total of eleven tuyas was used to infer a maximum possible passage zone elevation per edifice. A 120 m margin was added to the maximum elevation to account for fractured ice and surface sagging during eruption (Smellie et al., 2011).

An uncertainty that comes with using the knick point region as possible passage zone elevation is that the lava cap is included, as well. During tuya formation the passage zone always forms below the lava cap. This results in an overestimation of the passage zone elevation using the knick point analysis.

Identified tuyas have been superimposed either onto a straight line from North to South and a straight line from West to East. This was done to pragmatically constraint the axes of the ice sheet. A 2D analysis is a simplification and does only take into account the tuyas that are already located close to the straight lines. A 3D ice sheet fitting would decrease the difference between model and reality. However, a more realistic ice sheet profile would probably not affect decompression rates in the mantle largely. Therefore, a perfectly plastic glacier profile with a smooth horizontal bedrock was assumed. The latter assumption was based on the fact that surrounding area are fairly even without any topographic extremes and the loss in ice volume due the formation of tuyas is negligible.

To constrain the ice extent a circular ice sheet with a radius of 600 km was set. The fixed radius was based on the spatial distribution of the tuyas in the region of interest. In addition, it is sufficiently large to also cover other edifices in the region that might be of glaciovolcanic origin (Ghatan and Head (2002) Fagan et al. (2010)), but were not included in this study.

With the extracted maximum passage zone elevations and the fixed ice extend the fitting process was done. By varying the ice divide height (H_0) and the location of the ice sheet with respect to the tuyas in either WE or NS direction, an optimum ice thickness and location could be achieved. A perfectly plastic, circular ice sheet with a ice divide height of 1753.5 m and a radius of 600 km was the result of the analysis. The optimum location of the ice sheet midpoint was found to be at 7°E and 63.8°S.

b) *In what way can the ice sheet retreat period be derived from the spatial distribution of tuyas in the Dorsa Argentea Formation?*

Up until today, climate models for Mars are not very advanced yet and are still inaccurate for estimations of past climate back in the Hesperian epoch. However, same as on Earth, the planet's obliquity has a strong influence on the climatic processes on Mars. Research agrees that during high obliquity (>35°) the CO_2 is on the South Pole could extent to higher latitudes, also covering the region of the Sisyphi Montes.

Since the tuyas are clustered in a small region close to the South Pole on Mars it was assumed that ice from the South Polar cap only needed to extend slightly towards the equator to cover the entire region of interest. Studies suggest that in the Hesperian epoch the South Polar ice cap was much larger than today (Head and Pratt (2001); Head et al. (2007)). These suggestions were based on geological evidence and support that the Sisyphi Montes were once covered under ice.

Since estimates of obliquity evolution on Mars are available, the assumption was made to derive melting periods for the reconstructed ice sheet from the variations in obliquity. Models of obliquity variations are however only accurate for the past 20 Myr on Mars (Mischna, 2018), due to the chaotic nature of the solar system. It was therefore assumed, that obliquity variations in the Hesperian epoch were similar to estimates 20 Myr ago with a period of high obliquity for more than 5 Myr. This is in agreement to statistical estimates by Laskar et al. (2004a). According to previous research a peak to peak obliquity cycle takes about 120 kyr during which ice can grow and melt (Bramson et al. (2017); Laskar et al. (2004a); Madeleine et al. (2009); Schorghofer (2007)). Based on this, for the reconstructed ice sheet three different melting period have been assumed and simulated: 60 kyr, 30 kyr and 1 kyr. A short deglaciation of 1 kyr is comparable to the deglaciation of Iceland during the last maximum, where a similar sized ice sheet resulted in decompression melting as found by Jull and McKenzie (1996). From the finite element model maximum decompression rates were found for the shortest melting period (1 kyr). Although, shorter deglaciation periods result in larger decompression rates inside the mantle, anything below 1 kyr is an unlikely scenario. Besides, for short time scales ($\leq$ 1 yr) the mantle only behaves elastically (Whitehouse et al., 2021) and effects of viscosity on the depth of the decompression rates would not be present.

c) *How does induced change in mantle decompression affect the mantle melt rate underneath the degrading ice sheet?*

To answer this question the reconstructed ice sheet was used in a flat, symmetric, incompressible finite element model to model the pressure changes in the Martian mantle during deglaciation. A linear ice history was assumed, and two different FE models where created, one with a thin lithosphere (35 km) and one with a thick lithosphere (500 km). The former is more representative for a warm and wet Mars in the past (Grott and Breuer, 2008), whereas the latter is based on findings about the Martian interior structure today (Khan et al., 2021). The derived deglaciation periods mentioned above were tested with both FE models and results interpreted.

In this study a maximum decompression rate of 4474 Pa/yr was found for the model with a thin elastic lithosphere and a deglaciation period of 1 kyr. Decompression rates generally decrease with increasing depth, which is in agreement with results found in Iceland (Jull and McKenzie (1996); Pagli and Sigmundsson (2008); Schmidt et al. (2013)). Furthermore, longer deglaciation periods resulted in overall lower decompression rates inside the mantle, which are less likely to result in melting of material. A melting period of 1 kyr could be a likely scenario on ancient Mars during a wet and warm climate. In a study by Jull and McKenzie (1996) an ice sheet of similar size was simulated to melt over 1 kyr. If conditions were similar to the ones in Iceland during the last glacial maximum, such deglaciation period is very likely to be true for Mars in the past.

In addition, a sensitivity of decompression rate to lithosphere thickness was found. An increase in lithosphere from 35 km to 500 km caused a decrease in decompression rate at similar depth inside the mantle of up to 78%. From this, it can be concluded that mantle melting due to change in decompression rate is less likely on Mars today.

Decompression rates for the thin lithosphere model over a deglaciation of 1 kyr were found to be comparable to decompression rates underneath Vatnajökull during a deglaciation of 120 yr. Under Vatnajökull a maximum decompression rate of 1450 Pa/yr was found right below the lithosphere (Schmidt et al., 2013). Such decompression rate resulted in an increase in melt generation by 0.21-0.23 km^3/yr. On Mars, the same decompression rate was discovered at a depth of 500 km. The difference in depth compared to Iceland could be a result of lower viscosity, as well as the presence of a spreading ridge in Iceland.

It is important to note that for mantle melting to take place, the decompression rate must cause a drop in solidus temperature large enough for it to shift close to, or below, the actual mantle temperature. It was previously estimates that initial melt can occur at a depth of 490 km on Mars for a mantle potential temperature equal to 1450°C Ding et al. (2020). This depth is very close to the determined depth of maximum decompression rate found in this study. Based on these estimates it is likely that at 500 km solidus temperature and mantle temperature are close enough such that the decompression rate found caused a drop in melting temperature and initiation of melt.

Since melt generation potentially occurs at a lower depth on Mars than in Iceland, the ascent velocity of the magma becomes very important. Due to lower gravity on Mars, rise velocity of magma from the mantle to the surface would be larger on Mars. This is in favour for still causing eruptions under the ice, although melting takes place at deeper depth compared to Earth. For a rise magma extraction velocity of 1000 m/yr a delay in volcanism of 500 yr was calculated. Even for the shortest deglaciation period tested in this research, such a delay would still result in eruptions under the ice.

To be able to make conclusions about the actual melt rate and increase in volcanic activity, melt parametrisation as well as more detailed knowledge about the mantle composition are necessary.

By answering these research question, it is possible to draw a conclusion on the main research hypothesis that states:

> *The unloading of the Martian mantle, due to melting of a former ice sheet, has contributed to forming tuyas, glaciovolcanic edifices, in the South Polar region on Mars.*

In this study it was shown that by using the height and spatial distribution of tuyas in the South Polar Region on Mars, the thickness and extent of a palaeo ice sheet could be reconstructed. Furthermore, the ice sheet was applied used to constrain the surface load for a flat, symmetric, incompressible finite element model to simulate decompression rates in the Martian mantle during deglaciation. Two different FE models were used, one having a thick lithosphere and one with a thin one. Over three different deglaciation periods the decompression rates were evaluated.

A maximum decompression rate of 4474 Pa/yr was found right below the lithosphere. Furthermore, a decompression rate comparable to values found under Vatnajökull during recent deglaciation were observed at lower depth on Mars (500 km). Mantle decompression causes a drop in solidus temperature, which can initiate melting if the melting temperature drops below the actual mantle temperature. Based on estimates of the solidus depth inside the Martian mantle by Ding et al. (2020), it is likely that at a depth of 500 km, where the same decompression rate as under Iceland was found, the mantle temperature was very close to the solidus one. Therefore, a decompression rate the same as in Iceland could have likely initiates melting at 500 km inside Mars. However, these decompression rates have only been achieved with a thin lithosphere of 35 km. This would make the process of mantle melting not likely on Mars today.

Although possible melt is generated deeper in the Martian mantle, faster magma ascent due to Mars' lower gravity (Wilson and Head, 1994) would ensure that enhanced volcanism could occur about 500 yr after onset of deglaciation. Even for a deglaciation period of 1 kyr this would favour the formation of tuyas. Furthermore, the initiation of dykes would support faster magma ascent. A small investigation into driving pressures due to the horizontal stresses inside the Martian lithosphere has shown that dyke propagation could possibly have occurred, as well.

The research has shown that mantle melting due to deglaciation of a former ice sheet in the South Polar Region on Mars is indeed a likely scenario. This is especially true in the case that conditions on Mars in the past were similar or even the same as in Iceland today, meaning a wet and warm rheology.

4.2. Recommendations

Following recommendations for future work can be made, listed from highest to lowest priority. The first point is recommended for an extension of the study by a few weeks. Recommendations 2, 3 and 4 could result in a new Master thesis study.

1. *Investigating the effect of viscosity*
   With a few weeks extra in the project an investigation into the effects of viscosity on decompression rate is proposed. Decreasing the mantle viscosity to a value of $10^{19}\,\mathrm{Pa \cdot s}$ could provide interesting insights. Especially since Iceland has a low viscosity the comparison between the studies would bring even more understanding to the differences and similarities of the two planets.

2. *Age determination of tuyas*
   A more accurate age determination of the tuyas could leading to a more accurate ice sheet reconstruction. It is proposed to apply buffer crater counting on the summit surfaces of the mountains to determine their exact age. In order to do this, one could request a set of high resolution images from the HiRISE on the Mars Reconnaissance Orbiter of each of the tuyas in the South Polar Region. This would make crater counting more accurate than using MOLA data, since surface areas of the tuyas are small compared to surrounding areas and MOLA topography resolution not high enough. Furthermore, previous work from Hartmann (2005) on Martian isochrones can be used to determine the age. Based on number of craters per km^2 over the crater diameter they derived a set of curves that determine the surface age.

3. *Melt parametrisation and melt generation*
   The calculation of the melt fraction and actual amount of melt would provide details about how much melt would have been generated by the decompression rate found in this research. Due to large uncertainties in Martian mantle composition, thermal states and melt parametrisation and limited amount of time for the study, this has not been done yet. From the new seismic observations by the InSight mission, more information on Martian mantle composition can be obtained in the future. This could be used in a new Master thesis to propose a melt parametrisation, involving specific heat, thermal expansion coefficient and bulk water content. Furthermore a thorough study of the Martian meteorites could provide further insights into these parameters. In addition, analysis of the so called SNC meteorites can be used to derive information on the concentration of uranium and or thorium. This could serve as observations on the amount of melt generated by deglaciation, as is done in Iceland.

4. *Spherical FE model*
   Another Master thesis project could improving the finite element modelling by applying a spherical model. This ensures that the curvature of the planet is taken into account and makes the analysis more realistic. Especially for a case where the ice sheet was a large extension of the South Polar ice cap, a spherical model is highly recommended to achieve accurate and realistic.

5. *Automated knick point detection*
   To improving the ice sheet reconstruction, the knick point identification and detection of the passage zones can be automated in ArcGIS. This would reduce the working time, but also potential errors made by manual extraction. An advantage of the manual extraction is that by visual inspections outliers can be identified easier. Furthermore, object-based image analysis using the Digital Elevation Model data of Mars could be an alternative for detecting the knick point automatically.

6. *A drone mission to the tuyas*
   As a more abstract and more broad recommendation, a drone mission to the tuyas on Mars is suggested. Based on the recent success of flying a helicopter on Mars, a drone mission could be used to capture more high resolution imagery of the tuyas and topography of the surfaces. It could potentially be even used for sample return.

A

Using ArcGIS Pro on Mars

A.1. Importing MOLA Data into ArcGIS

When using Mission Experiment Gridded Data Records (MEGDR) from the Mars Orbiter Laser Altimeter (MOLA) go to the PDS Geoscience Node Mars Global Surveyor: MOLA MEGDRs data directory directory and download the set of data you need. These data consists of a set of three or four maps:

1. The planetary radius as recorded by the MOLA instrument
2. The areoid, a model for an equipotential surface of Mars, analogous to ”sea level” on Earth (this map is omitted for the 32, 64 and 128 pixel/degree and polar MEGDRs)
3. The topography computed as the difference between the radial coordinate and the areoid
4. Counts (number of observations) per cell in the map

To import the raster datasets into ArcGIS one needs the header files to help ArcGIS understand the data properly. Header files can be found in the EXTRAS directory

Things to keep in mind when working with ArcGIS and MOLA Data:

- Surface Parameters Tool (Spatial Analyst) first transforms data into an ECEF reference frame and computes all calculations in this frame. According to the ESRI community the tool is still applicable to Mars, as it transforms the results back into the reference frame of the input raster data.

- Vertical units not recognised by tools: even though the raster dataset source states vertical units = ’meter’ the tool does not recognise it. Reasons for this might be string vs. float or empty rows in metadata, etc. Check your metadata!

A.2. Creating a new Projected Coordinate System

Based on the Mars2000 Geographical Coordinate System one can create new projected coordinate systems applicable for Mars. ArcGIS supports different kinds of projections, from Albers Equal Area to Polar Stereographic ones over Lambert Conformal Conic and Transverse Mercator. Details can be found under Map Projections in ArcGIS When creating a new projection, keep in mind what your goal is: preservation of area, shapes, distances? Choosing the right projection can benefit you in future analyses.

Bibliography

Ackiss, S., B. Horgan, F. Seelos, W. Farrand, and J. Wray. Mineralogic evidence for subglacial volcanism in the Sisyphi Montes region of Mars. *Icarus*, 311:357–370, 2018. doi: 10.1016/j.icarus.2018.03.026.

Ackiss, S., B. Horgan, M. Suda, D. Minton, and A. Campbell. GEOMORPHOLOGIC MAPPING OF A POSSIBLE HESPERIAN SUBGLACIAL VOLCANIC ENVIRONMENT IN THE SISYPHI MONTES, MARS. In *50th Lunar and Planetary Science Conference 2019*, volume 2132, 2019.

Ackiss, S. E. *Investing the Mineralogy and Morphology of Subglacial Volcanoes on Earth and Mars*. PhD thesis, PURDUE UNIVERSITY, 2019.

Allen, C. C. Volcano-ice interactions on Mars. *Journal of Geophysical Research*, 84(B14):8048, 1979. ISSN 0148-0227. doi: 10.1029/jb084ib14p08048. URL http://dx.doi.org/10.1029/JB084iB14p08048.

Audet, P. Toward mapping the effective elastic thickness of planetary lithospheres from a spherical wavelet analysis of gravity and topography. *Physics of the Earth and Planetary Interiors*, 226:48–82, 2014. doi: 10.1016/j.pepi.2013.09.011. URL http://dx.doi.org/10.1016/j.pepi.2013.09.011.

Barr, I. D., C. M. Lynch, D. Mullan, L. De Siena, and M. Spagnolo. Volcanic impacts on modern glaciers: A global synthesis. *Earth-Science Reviews*, 182(November 2017):186–203, 2018. ISSN 00128252. doi: 10.1016/j.earscirev.2018.04.008.

Bouley, S., J. T. Keane, D. Baratoux, B. Langlais, I. Matsuyama, F. Costard, R. Hewins, V. Payré, V. Sautter, A. Séjourné, O. Vanderhaeghe, and B. Zanda. A thick crustal block revealed by reconstructions of early Mars highlands. *Nature Geoscience*, 13(2):105–109, 2020. doi: 10.1038/s41561-019-0512-6.

Bramson, A. M., S. Byrne, and J. Bapst. Preservation of Midlatitude Ice Sheets on Mars. *Journal of Geophysical Research: Planets*, 122(11):2250–2266, 2017. ISSN 21699100. doi: 10.1002/2017JE005357.

Broquet, A., M. A. Wieczorek, and W. Fa. Flexure of the Lithosphere Beneath the North Polar Cap of Mars: Implications for Ice Composition and Heat Flow. *Geophysical Research Letters*, 47(5):1–8, 2020. doi: 10.1029/2019GL086746.

Campbell, A., S. E. Ackiss, and B. Horgan. MORPHOLOGY OF POSSIBLE SUBGLACIAL VOLCANOES IN THE SISYPHI MONTES REGION OF MARS. *Lunar and Planetary Science Conference XLVII*, 47:1554, 2016.

Cottaar, S. and P. Koelemeijer. The interior of mars revealed. *Science*, 373(6553):388–389, 2021. doi: 10.1126/science.1110531.

Cousins, C. R. and I. A. Crawford. Volcano-ice interaction as a microbial habitat on earth and mars. *Astrobiology*, 11(7):695–710, 2011. doi: 10.1089/ast.2010.0550.

de Vet, S. *When the glacier left the volcano: Behaviour and fate of glaciovolcanic glass in different planetary environments*. PhD thesis, University of Amsterdam, 2013.

De Vries, M. V. W., R. G. Bingham, and A. S. Hein. A new volcanic province: An inventory of subglacial volcanoes in West Antarctica. *Geological Society Special Publication*, 461(1): 231–248, 2018. ISSN 03058719. doi: 10.1144/SP461.7.

Ding, S., R. Dasgupta, and K. Tsuno. The Solidus and Melt Productivity of Nominally Anhydrous Martian Mantle Constrained by New High Pressure-Temperature Experiments—Implications for Crustal Production and Mantle Source Evolution. *Journal of Geophysical Research: Planets*, 125(4):1–23, 2020. doi: 10.1029/2019JE006078.

Earle, S. *Physical Geology*. British Columbia Centre for Open Education, first edition, 2015.

Edwards, B. R., M. T. Gudmundsson, and J. K. Russell. Glaciovolcanism. In *The Encyclopedia of Volcanoes*, pages 377–393. Academic Press, 2 edition, 2015. ISBN 9780081022955.

Edwards, B. R., W. Kochtitzky, and S. Battersby. Global mapping of future glaciovolcanism. *Global and Planetary Change*, 195(March):103356, 2020. ISSN 09218181. doi: 10.1016/j.gloplacha.2020.103356.

Fagan, A. L., S. E. Sakimoto, and S. S. Hughes. Formation constraints on Martian north polar volcanic edifices. *Journal of Geophysical Research E: Planets*, 115(7), 2010. ISSN 01480227. doi: 10.1029/2009JE003476.

Fraser, C. I., A. Terauds, J. Smellie, P. Convey, and S. Chown. Geothermal activity helps life survive glacial cycles. *Proceedings of the National Academy of Sciences of the United States of America*, 111(15):5634–5639, 2014. ISSN 10916490. doi: 10.1073/pnas.1321437111.

Ghatan, G. J. and J. W. Head. Candidate subglacial volcanoes in the South polar region of Mars: Morphology, morphometry, and eruption conditions. *Journal of Geophysical Research: Planets*, 107(7), 2002. ISSN 01480227. doi: 10.1029/2001je001519. URL https://doi.org/10.1029/2001JE001519.

Grott, M. and D. Breuer. The evolution of the martian elastic lithosphere and implications for crustal and mantle rheology. *Icarus*, 193:503–515, 2008. doi: 10.1016/j.icarus.2007.08.015.

Grott, M. and D. Breuer. On the spatial variability of the martian elastic lithosphere thickness: Evidence for mantle plumes? *Journal of Geophysical Research*, 115(E3):1–16, 2010. ISSN 21562202. doi: 10.1029/2009JE003456.

Gudmundsson, A. Magma chambers: Formation, local stresses, excess pressures, and compartments. *Journal of Volcanology and Geothermal Research*, 237-238:19–41, 2012. doi: 10.1016/j.jvolgeores.2012.05.015. URL http://dx.doi.org/10.1016/j.jvolgeores.2012.05.015.

Gudmundsson, M. T., G. Larsen, A. Hoskuldsson, and A. G. Gylfason. Volcanic hazards in Iceland. *Jokull*, 58(58):251–268, 2008.

Hartmann, W. K. Martian cratering 8: Isochron refinement and the chronology of Mars. *Icarus*, 174(2 SPEC. ISS.):294–320, 2005. doi: 10.1016/j.icarus.2004.11.023.

Head, J. W. and S. Pratt. Extensive hesperian-aged south polar ice sheet on Mars: Evidence for massive melting and retreat, and lateral flow and ponding of meltwater. *Journal of Geophysical Research E: Planets*, 106(6):12229–12275, 2001. ISSN 01480227. doi: 10.1029/2000je001359.

Head, J. W., D. Marchant, and F. Forget. Regional polar glaciation in the hesperian period of the history of mars: The south circumpolar dorsa argentea formation as an ancient ice sheet remnant. In *Abstract 3115 presented at Seventh International Conference on Mars, Lunar Planet. Inst., Pasadena, Calif*, 2007.

Huggel, C., J. L. Ceballos, B. Pulgarín, J. Ramírez, and J. C. Thouret. Review and reassessment of hazards owing to volcano-glacier interactions in Colombia. *Annals of Glaciology*, 45(1985): 128–136, 2007. doi: 10.3189/172756407782282408.

Irgens, F. Springer, 1 edition, 2008. ISBN 978-3-540-74297-5.

Iverson, N. A., R. Lieb-Lappen, N. W. Dunbar, R. Obbard, E. Kim, and E. Golden. The first physical evidence of subglacial volcanism under the West Antarctic Ice Sheet. *Scientific Reports*, 7(1):1–8, 2017. ISSN 20452322. doi: 10.1038/s41598-017-11515-3.

Jakobsson, S. and M. Gudmundsson. Subglacial and intraglacial volcanic formations in Iceland. *JÖKULL*, 58, 2008.

Jakobsson, S. P. and G. L. Johnson. Intraglacial volcanism in the Western Volcanic Zone, Iceland. *Bulletin of Volcanology*, 74(5):1141–1160, 2012. doi: 10.1007/s00445-012-0589-x.

Jellinek, A. M., M. Manga, and M. O. Saar. Did melting glaciers cause volcanic eruptions in eastern California? Probing the mechanics of dike formation. *Journal of Geophysical Research: Solid Earth*, 109(9):1–10, 2004. doi: 10.1029/2004JB002978.

Jiménez-Díaz, A., I. Egea-Gonzalez, L. M. Parro, M. Tasaka, and J. Ruiz. The thermal structure and mechanical behavior of the martian lithosphere. *Icarus*, 353(December 2019), 2021. doi: 10.1016/j.icarus.2020.113635.

Johnson, C. L., S. C. Solomon, J. W. Head, R. J. Phillips, D. E. Smith, and M. T. Zuber. Lithospheric Loading by the Northern Polar Cap on Mars. *Icarus*, 144(2):313–328, 2000. doi: 10.1006/icar.1999.6310.

Jones, J. Intraglacial volcanoes of the Laugarvatn region, south-west Iceland-I. *Quarterly Journal of the Geological Society of London*, 124(1-4):197–211, 1968. doi: 10.1144/gsjgs.124.1.0197.

Jull, M. and D. McKenzie. The effect of deglaciation on mantle melting beneath Iceland. *Journal of Geophysical Research*, 101:21,815–21,828, 1996. ISSN 2156-2202. doi: 10.1029/96jb01308.

Kelman, M. C., J. K. Russell, and C. J. Hickson. Effusive intermediate glaciovolcanism in the Garibaldi Volcanic Belt, southwestern British Columbia, Canada M. *Geological Society Special Publication*, 202:195–211, 2002. doi: 10.1144/GSL.SP.2002.202.01.10.

Khan, A. and J. A. Connolly. Constraining the composition and thermal state of Mars from inversion of geophysical data. *Journal of Geophysical Research E: Planets*, 113(7):1–19, 2008. doi: 10.1029/2007JE002996.

Khan, A., S. Ceylan, M. van Driel, and E. Al. Upper mantle structure of Mars from InSight seismic data. *Science*, 373(July):434–438, 2021.

Knapmeyer-Endrun, B., M. P. Panning, F. Bissig, R. Joshi, A. Khan, D. Kim, V. Lekić, B. Tauzin, S. Tharimena, M. Plasman, N. Compaire, F. Garcia, L. Margerin, M. Schimmel, N. Schmerr, E. Bozdağ, A.-c. Plesa, M. A. Wieczorek, A. Broquet, D. Antonangeli, S. M. Mclennan, H. Samuel, L. Pan, S. E. Smrekar, C. L. Johnson, N. Brinkman, A. Rivoldini, P. M. Davis, P. Lognonné, B. Pinot, R. Scholz, S. Stähler, M. Knapmeyer, M. V. Driel, D. Giardini, and W. B. Banerdt. Thickness and structure of the Martian crust from InSight seismic data. *Science*, 373(July):438–443, 2021.

Laskar, J., A. C. Correia, M. Gastineau, F. Joutel, B. Levrard, and P. Robutel. Long term evolution and chaotic diffusion of the insolation quantities of Mars. *Icarus*, 170(2):343–364, 2004a. doi: 10.1016/j.icarus.2004.04.005.

Laskar, J., P. Robutel, F. Joutel, M. Gastineau, B. Levrard, J. Laskar, P. Robutel, F. Joutel, M. Gastineau, A. C. M. Correia, J. Laskar, P. Robutel, F. Joutel, M. Gastineau, A. C. M. Correia, and B. Levrard. A long term numerical solution for the insolation quantities of the Earth. *Astronomy and Astrophysics*, 2004b.

Licciardi, J. M., M. D. Kurz, and J. M. Curtice. Glacial and volcanic history of Icelandic table mountains from cosmogenic 3He exposure ages. *Quaternary Science Reviews*, 26(11-12): 1529–1546, 2007. ISSN 02773791. doi: 10.1016/j.quascirev.2007.02.016.

Lodders, K. and B. Fegley. An oxygen isotope model for the composition of Mars. *Icarus*, 126 (2):373–394, 1997. doi: 10.1006/icar.1996.5653.

Maclennan, J., M. Jull, D. McKenzie, L. Slater, and K. Grönvold. The link between volcanism and deglaciation in iceland. *Geochemistry, Geophysics, Geosystems*, 3(11):1–25, 2002. doi: 10.1029/2001GC000282.

Madeleine, J., F. Forget, J. W. Head, B. Levrard, F. Montmessin, and E. Millour. Amazonian northern mid-latitude glaciation on Mars : A proposed climate scenario. *Icarus*, 203(2): 390–405, 2009. ISSN 0019-1035. doi: 10.1016/j.icarus.2009.04.037. URL http://dx.doi.org/10.1016/j.icarus.2009.04.037.

Madeleine, J. B., J. W. Head, F. Forget, T. Navarro, E. Millour, A. Spiga, A. Colaïtis, A. Määttänen, F. Montmessin, and J. L. Dickson. Recent Ice Ages on Mars: The role of radiatively active clouds and cloud microphysics. *Geophysical Research Letters*, 41(14):4873–4879, 2014. doi: 10.1002/2014GL059861.

Mansfield, M., E. S. Kite, and M. A. Mischna. Effect of Mars Atmospheric Loss on Snow Melt Potential in a 3.5 Gyr Mars Climate Evolution Model. *Journal of Geophysical Research: Planets*, 123(4):794–806, 2018. doi: 10.1002/2017JE005422.

Martínez-Alonso, S., M. T. Mellon, M. E. Banks, L. P. Keszthelyi, and A. S. McEwen. Evidence of volcanic and glacial activity in Chryse and Acidalia Planitiae, Mars. *Icarus*, 212(2):597–621, 2011. ISSN 00191035. doi: 10.1016/j.icarus.2011.01.004.

Mathews, W. H. ”Tuyas,” flat-topped volcanoes in northern British Columbia. *American Journal of Science*, 245:560–570, 1947.

Maxwell, J. On the Dynamical Theory of Gases. In *Proceedings of the Royal Society of London*, volume 15, pages 167–171, 1867.

Mischna, M. A. *Orbital (Climatic) forcing and its imprint on the global landscape*. Elsevier Inc., 2018. doi: 10.1016/B978-0-12-813018-6.00001-7.

Mischna, M. A. and S. Piqueux. The role of atmospheric pressure on Mars surface properties and early Mars climate modeling. *Icarus*, 342(September 2019):113496, 2020. doi: 10.1016/j.icarus.2019.113496. URL https://doi.org/10.1016/j.icarus.2019.113496.

Mischna, M. A., M. I. Richardson, R. J. Wilson, and D. J. McCleese. On the orbital forcing of Martian water and CO2 cycles: A general circulation model study with simplified volatile schemes. *Journal of Geophysical Research E: Planets*, 108(6):1–25, 2003. doi: 10.1029/2003je002051.

Mora, D. and A. Tassara. Upper crustal decompression due to deglaciation-induced flexural unbending and its role on post-glacial volcanism at the Southern Andes. *Geophysical Journal International*, 216(3):1549–1559, mar 2019. doi: 10.1093/gji/ggy473.

Neukum, G., A. T. Basilevsky, T. Kneissl, M. G. Chapman, S. van Gasselt, G. Michael, R. Jaumann, H. Hoffmann, and J. K. Lanz. The geologic evolution of Mars: Episodicity of resurfacing events and ages from cratering analysis of image data and correlation with radiometric ages of Martian meteorites. *Earth and Planetary Science Letters*, 294(3-4):204–222, 2010. doi: 10.1016/j.epsl.2009.09.006.

Neumann, G. A., M. T. Zuber, M. A. Wieczorek, P. J. McGovern, F. G. Lemoine, and D. E. Smith. Crustal structure of Mars from gravity and topography. *Journal of Geophysical Research E: Planets*, 109(8):1–18, 2004. ISSN 01480227. doi: 10.1029/2004JE002262.

Pagli, C. and F. Sigmundsson. Will present day glacier retreat increase volcanic activity? Stress induced by recent glacier retreat and its effect on magmatism at the Vatnajökull ice cap, Iceland. *Geophysical Research Letters*, 35(9):3–7, 2008. doi: 10.1029/2008GL033510.

Phillips, R. J., M. T. Zuber, S. E. Smrekar, M. T. Mellon, J. W. Head, K. L. Tanaka, N. E. Putzig, S. M. Milkovich, B. A. Campbell, J. J. Plaut, A. Safaeinili, R. Seu, D. Biccari, L. M. Carter, G. Picardi, R. Orosei, P. Surdas Mohit, E. Heggy, R. W. Zurek, A. F. Egan, E. Giacomoni, F. Russo, M. Cutigni, E. Pettinelli, J. W. Holt, C. J. Leuschen, and L. Marinangeli. Mars north polar deposits: stratigraphy, age, and geodynamical response. *Science*, 320(5880):1182–1185, 2008. ISSN 00368075. doi: 10.1126/science.1157546.

Plesa, A., S. Padovan, N. Tosi, D. Breuer, M. Grott, M. Wieczorek, T. Spohn, S. Smrekar, and W. Banerdt. The Thermal State and Interior Structure of Mars. *Geophysical Research Letters*, 3:198–209, 2018. doi: 10.1029/2018GL080728.

Qin, W. Mars surface stress modeling investigation on the crustal structure of mars with finite element method. Master's thesis, Delft University of Technology, 2021. URL http://resolver.tudelft.nl/uuid:74eb3038-2de4-44b9-bac7-07d94becd48e.

Robinson, C. A. The crustal dichotomy of Mars. *Earth, Moon, and Planets*, 69(3):249–269, 1995. doi: 10.1007/BF00643787.

Russell, J., B. R. Edwards, L. Porritt, and C. Ryane. Tuyas: A descriptive genetic classification. *Quaternary Science Reviews*, 87:70–81, 2014. ISSN 02773791. doi: 10.1016/j.quascirev.2014.01.001.

Schmidt, P., B. Lund, C. Hieronymus, J. Maclennan, T. Árnadõttir, and C. Pagli. Effects of present-day deglaciation in Iceland on mantle melt production rates. *Journal of Geophysical Research: Solid Earth*, 118(7):3366–3379, 2013. doi: 10.1002/jgrb.50273.

Schorghofer, N. Dynamics of ice ages on Mars. *Nature*, 449(7159):192–194, 2007. doi: 10.1038/nature06082.

Seroussi, H., E. R. Ivins, D. A. Wiens, and J. Bondzio. Influence of a West Antarctic mantle plume on ice sheet basal conditions. *Journal of Geophysical Research: Solid Earth*, 122(9): 7127–7155, 2017. ISSN 21699356. doi: 10.1002/2017JB014423.

Sigmundsson, F., V. Pinel, B. Lund, F. Albino, C. Pagli, H. Geirsson, and E. Sturkell. Climate effects on volcanism: Influence on magmatic systems of loading and unloading from ice mass variations, with examples from Iceland. *Philosophical Transactions of the Royal Society A: Mathematical, Physical and Engineering Sciences*, 368(1919):2519–2534, 2010. doi: 10.1098/rsta.2010.0042.

Simulia Abaqus. Abaqus analysis user's guide, 2014a. URL http://130.149.89.49:2080/v6.14/books/usb/default.htm?startat=pt02ch04s02.htm.

Simulia Abaqus. Abaqus 6.14 scripting reference guide, 2014b. URL http://130.149.89.49:2080/v6.14/books/ker/default.htm.

Smellie, J. L. The relative importance of supraglacial versus subglacial meltwater escape in basaltic subglacial tuya eruptions: An important unresolved conundrum. *Earth-Science Reviews*, 74(3-4):241–268, 2006. ISSN 00128252. doi: 10.1016/j.earscirev.2005.09.004.

Smellie, J. L. Quaternary Vulcanism: Subglacial Landforms. In *Encyclopedia of Quaternary Science: Second Edition*, pages 780–802. Elsevier B.V., 2 edition, 2013. ISBN 9780444536433. doi: 10.1016/B978-0-444-53643-3.00074-1.

Smellie, J. L. Glaciovolcanism: A 21st Century Proxy for Palaeo-Ice. In *Past Glacial Environments*, pages 335–375. Elsevier Ltd, second edition, 2018.

Smellie, J. L. and B. R. Edwards. *Glaciovolcanism on Earth and Mars*. Cambridge University Press, first edition, 2016.

Smellie, J. L., S. Rocchi, and P. Armienti. Late Miocene volcanic sequences in northern Victoria Land, Antarctica: Products of glaciovolcanic eruptions under different thermal regimes. *Bulletin of Volcanology*, 73(1):1–25, 2011. ISSN 02588900. doi: 10.1007/s00445-010-0399-y.

Smellie, J. L. Lava-Fed Deltas. In *Encyclopedia of Planetary Landforms*. 2014. ISBN 9781461492139. doi: 10.1007/978-1-4614-9213-9.

Smith, D., M. Zuber, G. Neumann, E. Guinness, and S. Slavney. Mars Global Surveyor Laser Altimeter Mission Experiment Gridded Data Record, MGS-M-MOLA-5-MEGDR-L3-V1.0, NASA Planetary Data System, 2003. Accessed: April 2021.

Stähler, A. S. C., A. Khan, W. B. Banerdt, P. Lognonné, S. Ceylan, M. Drilleau, A. C. Duran, R. Garcia, H. Quancheng, D. Kim, V. Lekic, H. Samuel, M. Schimmel, N. Schmerr, D. Sollberger, É. Stutzmann, Z. Xu, D. Antonangeli, C. Constantinos, P. Davis, J. C. Irving, T. Kawamura, M. Knapmeyer, R. Maguire, A. G. Marusiak, M. P. Panning, C. Perrin, A.-C. Plesa, A. Rivoldini, C. Schmelzbach, G. Zenhäusern, É. Beucler, J. Clinton, N. Dahmen, M. van Driel, T. Gudkova, A. Horleston, T. Pike, M. Plasman, and S. Smrekar. Seismic detection of the Martian core. *Science*, 373:443–448, 2021.

Steinberger, B., S. C. Werner, and T. H. Torsvik. Deep versus shallow origin of gravity anomalies, topography and volcanism on Earth, Venus and Mars. *Icarus*, 207(2):564–577, 2010. doi: 10.1016/j.icarus.2009.12.025.

Stroncik, N. A. and H. U. Schmincke. Palagonite - A review. *International Journal of Earth Sciences*, 91(4):680–697, 2002. doi: 10.1007/s00531-001-0238-7.

Tanaka, K. L. and E. J. Kolb. Geologic history of the polar regions of Mars based on Mars Global survey data. I. Noachian and Hesperian Periods. *Icarus*, 154(1):3–21, 2001. doi: 10.1006/icar.2001.6675.

Tanaka, K. L. and D. H. Scott. Geologic Map of the polar regions of Mars. *U.S. Geological Survey Miscellaneous Investigations Series Map*, 1987. I–1802–C.

Thor, R. *Mapping the Thickness of the Martian Elastic Lithosphere using Maximum Likelihood Estimation*. PhD thesis, Delft University of Technology, 2016.

Tuffen, H., J. Owen, and J. Denton. Magma degassing during subglacial eruptions and its use to reconstruct palaeo-ice thicknesses. *Earth-Science Reviews*, 99(1-2):1–18, 2010. doi: 10.1016/j.earscirev.2010.01.001.

van der Veen, C. *Fundamentals of Glacier Dynamics*. A.A. Balkema Publishers, 1999.

Walker, G. P. Aspects of Quaterny Volcanism, Iceland. In *Transact. Leicester Lit. Philosoph. Soc*, volume 59, pages 29–40. 1965.

Ward, W. R. Climatic variations on Mars: 1. Astronomical theory of insolation. *Journal of Geophysical Research*, 79(24):3375–3386, 1974. ISSN 0148-0227. doi: 10.1029/jc079i024p03375.

Whitehouse, P., G. Milne, and K. Lambeck. Glacial isostatic adjustment. In A., F. and N. F., editors, *Glaciers and Ice Sheets in the Climate System*. Springer Textbooks in Earth Sciences, Geography and Environment. Springer, Cham, 2021. doi: 10.1007/978-3-030-42584-5_15.

Whitehouse, P. L. Glacial isostatic adjustment modelling: Historical perspectives, recent advances, and future directions. *Earth Surface Dynamics*, 6(2):401–429, 2018. ISSN 2196632X.

Wieczorek, M. A. and M. T. Zuber. Thickness of the Martian crust: Improved constraints from geoid-to-topography ratios. *Journal of Geophysical Research E: Planets*, 109(1):1–16, 2004. ISSN 01480227. doi: 10.1029/2003je002153.

Wilson, A., J. Russell, and B. Ward. Paleo-glacier reconstruction in southwestern British Columbia, Canada: A glaciovolcanic model. *Quaternary Science Reviews*, 218(2019):178–188, 2019. ISSN 02773791. doi: 10.1016/j.quascirev.2019.06.024.

Wilson, A. M. and J. K. Russell. Glacial pumping of a magma-charged lithosphere: A model for glaciovolcanic causality in magmatic arcs. *Earth and Planetary Science Letters*, 548:116500, 2020. doi: 10.1016/j.epsl.2020.116500.

Wilson, L. and J. W. Head. Mars: Review and Analysis and of Volcanic Eruption Theory and Relationships to Observed Landforms. *Reviews of Geophysics*, 32(3):221–263, 1994. ISSN 8755-1209.

Wu, P. Using commercial finite element packages for the study of earth deformations, sea levels and the state of stress. *Geophysical Journal International*, 158(2):401–408, 2004. doi: 10.1111/j.1365-246X.2004.02338.x.

Wu, P. and W. R. Peltier. Viscous gravitational relaxation. *Geophysical Journal of the Royal Astronomical Society*, 70(2):435–485, 1982. doi: 10.1111/j.1365-246X.1982.tb04976.x.

Zahra, T., U. Paudel, Y. S. Hayakawa, and T. Oguchi. Knickzone Extraction Tool (KET) - A new ArcGIS toolset for automatic extraction of knickzones from a DEM based on multi-scale stream gradients. *Open Geosciences*, 9(1):73–88, 2017. doi: 10.1515/geo-2017-0006.